University of North Carolina at Chapel Hill
Solar Energy Research Center
UNC SERC

Solar Energy Research Center Instrumentation Facility

Award DE-EE0003188
August 15, 2010 – August 14, 2011

Final Scientific and Technical Report

DOE Award Number:	DE-EE0003188
Project Title:	Solar Energy Research Center Instrumentation Facility
Reporting period Start Date:	August 15, 2010
Reporting period End Date:	August 14, 2011
Report Issued:	November 2011
Lead Institution:	University of North Carolina at Chapel Hill
Principal Investigator:	Thomas J. Meyer, Arey Distinguished Professor of Chemistry Director, UNC Solar Energy Research Center SERC Department of Chemistry, Campus Box 3290 Caudill & Kenan Laboratories The University of North Carolina at Chapel Hill Chapel Hill, NC 27599-3290 (919) 843-8313 tjmeyer@unc.edu
Administrative Contact:	Catherine M. Heyer, Ph.D. Assistant Director, UNC Energy Frontier Research Center EFRC, Department of Chemistry, Campus Box 3290 Caudill & Kenan Laboratories The University of North Carolina at Chapel Hill Chapel Hill, NC 27599-3290 (919) 962-2304 cmheyer@unc.edu
Cost-Share Partners:	Balfour Beatty Construction Company, Raleigh, NC Wilson Architects, Chapel Hill, NC
DOE Project Team:	DOE Field Contracting Officer: Michael Buck DOE Field Project Officer: Holly Thomas Project Engineer: Andrew Kobusch

Solar Energy Research Center Instrumentation Facility

Award DE-EE0003188

August 15, 2010 – August 14, 2011

2. Table of Contents

3. EXECUTIVE SUMMARY

The mission of the Solar Energy Research Center (UNC SERC) at the University of North Carolina at Chapel Hill (UNC-CH) is to establish a world leading effort in solar fuels research and to develop the materials and methods needed to fabricate the next generation of solar energy devices. We are addressing the fundamental issues that will drive new strategies for solar energy conversion and the engineering challenges that must be met in order to convert discoveries made in the laboratory into commercially available devices.

The development of a photoelectrosynthesis cell (PEC) for solar fuels production faces daunting requirements: (1) Absorb a large fraction of sunlight; (2) Carry out artificial photosynthesis which involves multiple complex reaction steps; (3) Avoid competitive and deleterious side and reverse reactions; (4) Perform 13 million catalytic cycles per year with minimal degradation; (5) Use non-toxic materials; (6) Cost-effectiveness. PEC efficiency is directly determined by the kinetics of each reaction step. The UNC SERC is addressing this challenge by taking a broad interdisciplinary approach in a highly collaborative setting, drawing on expertise across a broad range of disciplines in chemistry, physics and materials science. By taking a systematic approach toward a fundamental understanding of the mechanism of each step, we will be able to gain unique insight and optimize PEC design. Access to cutting-edge spectroscopic tools is critical to this research effort. We have built professionally-staffed facilities equipped with the state-of the-art instrumentation funded by this award. The combination of staff, facilities, and instrumentation specifically tailored for solar fuels research establishes the ***UNC Solar Energy Research Center Instrumentation Facility*** as a unique, world-class capability.

This congressionally directed project funded the development of two user facilities:

Task 1: Solar Device Fabrication Laboratory Development:

The space allocated for this laboratory was "shell space" that required an upfit in order to accommodate nano-fabrication equipment in a *quasi*-clean room environment. This construction project (cost $279,736) met the non-federal cost share requirement of $250,000 for this award. The central element of the fabrication laboratory is a new $400,000+ stand-alone system, funded by other sources, for fabricating and characterizing photovoltaic devices, in a state-of-the-art nanofabrication environment.

This congressionally directed project also included the purchase of an energy dispersive x-ray analysis (EDX) detector for a pre-existing transmission electron microscope (TEM). This detector allows elemental analysis and elemental mapping of materials used to fabricate solar energy devices which is a key priority for our research center.

Task 2: Solar Energy Spectroscopy Laboratory Development (Instrumentation):

This laboratory provides access to modern spectroscopy and photolysis instrumentation for characterizing devices, materials and components on time scales ranging from femtoseconds to seconds and for elucidating mechanisms. The goals of this congressionally directed project included the purchase and installation of spectroscopy and photolysis instrumentation that would substantially and meaningfully enhance the capabilities of this laboratory. Some changes were made to the list of equipment proposed in the original budget. These changes did not represent a change in scope, approach or aims of this project. All of the capabilities and experiments represented in the original budget were maintained.

The outcome of this Congressionally Directed Project has been the development of world-class fabrication and spectroscopy user facilities for solar fuels research at UNC-CH. This award

has provided a significant augmentation of our pre-existing instrumentation capabilities which were funded by earlier UNC SERC projects, including the Energy Frontier Research Center UNC EFRC, funded by the US Department of Energy Office of Basic Energy Sciences. Equipment funded by this congressional award has provided important new capabilities for UNC SERC and has greatly facilitated collaborative research by many multi-institutional teams in the six partner institutions of the UNC EFRC, including Duke University, North Carolina Central University, and North Carolina State University. This state-of-the-art instrumentation has allowed us to design cutting-edge experiments that provide insight into the molecular structure and dynamics of materials and components for solar energy conversion under real working conditions. This research has resulted in ten publications already published or in preparation that acknowledge support from DOE EERE for this congressionally directed project.

4. COMPARISON OF ACTUAL ACHIEVEMENTS WITH GOALS AND OBJECTIVES OF PROJECT

Goals and objectives for this congressionally directed project were identified as follows:

> The UNC Solar Energy Research Center will develop the Solar Energy Research Center Instrumentation Facility to provide access to state-of-the-art instrumentation for scientists pursuing solar energy research. The instrumentation facility will consist of two primary laboratories: The Solar Device Fabrication Laboratory (Task 1) and the Solar Energy Spectroscopy Laboratory (Task 2).

Table 1: Project Goals and Achievements

TASK 1:	**SOLAR DEVICE FABRICATION LABORATORY**
GOAL - Subtask 1.1	Upfit of shell space to construct Solar Device Fabrication Laboratory ($280K – institutional cost share)
GOAL - Subtask 1.2	Purchase and install EDX (Energy Dispersive X-ray Analysis) detector for existing Transmission Electron Microscope (TEM) ($69K)
KEY MILESTONES (Proposed):	• Laboratory space upfit to accommodate planned equipment • EDX detector ordered, • Equipment delivered. • Equipment installed, fully operational and available for use by researchers under guidance of trained personnel.
ACHIEVEMENTS:	All milestones were met as planned and on schedule
TASK 2:	**SOLAR ENERGY SPECTROSCOPY LABORATORY**
GOAL - Task 2	Purchase and installation of spectroscopy and photolysis instrumentation in Solar Energy Spectroscopy Laboratory ($931K)
KEY MILESTONES (Proposed):	• Listed Equipment ordered. • Listed Equipment delivered. • Listed Equipment installed, fully operational and available for use by researchers under the guidance of trained personnel.
ACHIEVEMENTS:	All milestones were completed on schedule. Some changes were made to the list of equipment proposed in the original budget. These changes did not represent a change in scope, approach or aims of this project. All of the capabilities and experiments represented in the original budget were maintained.

The upfit construction and development of the Solar Device Fabrication Laboratory was completed as planned and on schedule, with details provided in Section 5. The development of the Solar Energy Spectroscopy Laboratory, Task 2, was also completed on schedule. Some changes were made to the list of equipment proposed in the original budget. These changes did not represent a change in scope, approach or aims of this project. All of the capabilities and experiments represented in the original budget were maintained. By the end of the award period on 8/14/2011 all equipment was fully operational and being used by trained researchers. Details are provided in Section 5.

5. SUMMARY OF PROJECT ACTIVITIES

As described above, this award funded two tasks which correlated with the development of two instrumentation facility laboratories, the Solar Device Fabrication Laboratory (Task 1) and the Solar Energy Spectroscopy Laboratory (Task 2). Both tasks were independent of each other and were pursued in parallel. Table 2 provides a timeline of progress during each reporting quarter of the award period. All subtasks and all elements of this project were successfully completed on schedule before the end of the award period on 8/14/2011, thus meeting all goals and objectives for this congressionally directed project.

Table 2: Time Line of Accomplishments During Award Period
See list of equipment and detailed status in Table 5

Task		Subtask		Goals/Objectives for One Year Award Period 8/15/2010 – 8/14/2011	Accomplishments After 1st Reporting Quarter 8/15 - 9/30/2010	Accomplishments After 2nd Reporting Quarter 10/1 - 12/31/10	Accomplishments After 3rd Reporting Quarter 1/1 - 3/31/11	Accomplishments After 4th Reporting Quarter 4/1-6/30/11	Accomplishments After 5th Reporting Quarter 7/1-9/30/11
1.	Solar Device Fabrication Lab Development	1.1	Upfit of Lab Space	• Laboratory space upfitted to accommodate planned equipment	• 95% complete on 9/30/2010	• 100% complete as of 10/31/2010	• 100% complete as of 10/31/2010	• 100% complete as of 10/31/2010	• 100% complete as of 10/31/2010
		1.2	Purchase & Install Equipment	• EDX detector ordered	• Competitive bid process is underway	• Equipment selection finalized.	• 100% complete	• 100% complete	• 100% complete
				• Equipment delivered	• Not yet begun	• Not yet begun	• Delivered 4/8/2011	• 100% complete	• 100% complete
				• Equipment installed, fully operational & available for use by researchers under guidance of trained personnel	• Not yet begun	• Not yet begun	• Not yet begun	• 100% complete	• 100% complete
2.	Solar Energy Spectroscopy Lab Development			• Listed Equipment* ordered	• 76% complete	• 85% complete	• 95% complete	• 100% complete	• 100% complete
				• Listed Equipment* delivered	• 50% complete	• 83% complete	• 88% complete	• 95% complete	• 100% complete as of 8/14/2011
				• Listed Equipment* installed, fully operational & available for use by researchers under guidance of trained personnel	• 17% complete	• 70% complete	• 88% complete	• 92% complete	• 100% complete as of 8/14/2011

TASK 1: SOLAR DEVICE FABRICATION LABORATORY DEVELOPMENT

Subtask 1.1: Upfit of Laboratory Space in Chapman Hall

The space allocated for this laboratory was 655 square feet of "shell space" in the recently constructed Chapman Hall that required an upfit in order to create the Solar Device Fabrication Laboratory. This laboratory was required to accommodate nanofabrication equipment for fabrication and characterization of photovoltaic devices for solar energy conversion. A quasi-clean room environment is essential to eliminate dust particles that severely harm the electrical performance, reproducibility and reliability of sample fabrication. This construction project (cost $279,736) met the non-federal cost share requirement of $250,000 for this award. Construction began on 4/6/2010 and was completed by 10/31/2010. Progress and timelines for this upfit project are summarized in Table 3. Full details were provided in earlier quarterly reports.

The central element of the fabrication laboratory is a new $400,000+ stand-alone system for fabricating and characterizing photovoltaic devices, in a state-of-the-art nanofabrication environment. This equipment was partially funded with UNC EFRC funds. The system has an appropriate array of optical tools under an inert atmosphere that provide device characterization without sample degradation. These tools include a vacuum deposition module in a train of inert atmosphere glove-boxes with the associated spin-coater, high resolution microscope, optical goniometer interfaced with an optical monochromator and a 1.5 AM solar simulator. The equipment is computer controlled, built from individual components and enclosed in a controlled low humidity glove box. In addition, a Keithley 4200-SCS semiconductor characterization system capable of IV, Pulse IV, and CV measurements of electronic devices with sub-femtoAmp resolution is available with four channels. A two sun solar simulator is also available.

Table 3. Subtask 1.1 – Upfit Construction Project
Cost Status and Schedule - Recipient Cost Share

ITEM	SCHEDULE*	COST*	CUMULATIVE % WORK COMPLETED
Design Cost		**$32,950**	
Construction Cost 4/6/2010 – 12/31/2010	Apr 2010	$13,597	6%
	May 2010	$46,193	24%
	Jun 2010	$96,698	63%
	Jul 2010	$57,410	87%
	Aug 2010	$19,324	95%
	Sept 2010	$2,408	95%
	Oct 2010	$11,156	100%
	Nov 2010	$0	100%
	Dec 2010	$0	100%
Construction Sub-Total		**$246,786**	
GRAND TOTAL RECIPIENT COST SHARE Design ($32,950) + Construction ($246,786)		**$279,736**	**Successfully completed**

Completion of the construction upfit project to create the Solar Device Fabrication Laboratory represented the successful completion of Subtask 1.1.

Task 1 Subtask 1.2: Purchase and Installation of Instrumentation (TEM EDX Detector) for Solar Device Fabrication Laboratory (Experiment 8 in Table 5)

The energy dispersive x-ray analysis (EDX) detector for a pre-existing transmission electron microscope (TEM) was installed in June 2011 and many trained users are making use of this new capability. Elemental analysis and elemental mapping of materials used to fabricate solar energy devices is a key priority. The 250 TEM EDX detector uses a large area 80 mm^2 crystal which offers users more than 10x the solid collection angle, and therefore 10x the count rate, of conventional energy dispersive spectrometer detectors, without compromising on performance. This is especially important for research which involves nanoparticles with diameters on the order of tens of nanometers. Examples of research carried out, or planned, using the system include:

- Doping different elements into TiO_2 has been shown to improve the efficiency of solar energy conversion, and changing the physical and chemical properties of TiO_2 nanowires could effectively improve the open circuit voltage of dye-sensitized solar cells. The EDX on the TEM system is being used to carry out elemental mapping of single nanowires to address the composition and distribution of the dopant across the nanowire and to study the growth mechanisms of nanowires fabricated under different conditions.
- The EDX has been used to examine the composition of indium tin oxide nanoparticles and to study electrochemically tagged surface-bound silane molecules. These functionalized nanoparticles will be used in solar cell applications.
- The conversion of greenhouse gases into usable fuels such as methane, methanol, or higher order alkanes by using platinum nanoparticles in the reduction of CO_2 is being studied. Platinum is electrodeposited onto electrode surfaces that contain an iron complex, and the EDX is being used to determine the composition of the platinum and the iron complex after platinum deposition.
- The EDX detector is being used in the study of metal-organic frameworks for energy applications, such as hydrogen storage and solar fuel production. We are also working on the syntheses of a hematite/titania/platinum nanocomposite material capable of catalyzing hydrogen production from water. The EDX detector is used to quantitate iron, titanium, and platinum in the material.

TASK 2: SOLAR ENERGY SPECTROSCOPY LABORATORY DEVELOPMENT

The goal of Task 2 was the purchase and installation of selected research equipment for the Solar Energy Spectroscopy Laboratory. This 1200 sq-ft spectroscopy laboratory is located in the recently constructed Caudill Laboratory building on the UNC-CH campus**.** All instrumentation funded with this award is installed and fully operational. With these acquisitions this laboratory now provides access to modern spectroscopy instrumentation for performing measurements and for characterizing devices, materials and components on time scales ranging from femtoseconds to seconds, and for elucidating mechanisms. The laboratory is staffed by two full-time Ph.D. positions, both supported by the UNC Energy Frontier Research Center: a facility director who is a senior research scientist in spectroscopy and a staff research associate in spectroscopy whose duties include supporting the facility director and who is responsible for maintaining the equipment and training users.

All of the instrumentation funded by this award is fully tested and operational and is available for use by all researchers who complete training and sign our facility user agreement.

Users must first complete a general laboratory safety orientation and a laser safety course, both run by the UNC office of Environmental Health and Safety. Users must then receive hands-on training on each instrument they plan to use. Users, their faculty advisor and the laser facility director must sign off that training has been satisfactorily completed. Users agree to sign and update the instrument log book and are financially responsible for any damage to the instrument due to negligence. Users further agree to acknowledge support from this DOE EERE award in all publications based on research performed using the facility. The instrumentation has seen heavy use and is being used in a wide variety of experiments related to the characterization of materials and components that will be used to fabricate photoelectrosynthesis cells for solar fuels production. This work has resulted in ten publications already published or in preparation. Many more papers are in gestation. This instrumentation represents new capabilities for the UNC SERC and the UNC EFRC and is providing insight into the molecular dynamics of photoelectrosynthesis cells under real working conditions.

The following instrumentation was listed in the award proposal:

1. Steady-state and time-resolved emission spectrometer
2. Nanosecond time-resolved infrared (TRIR) absorption instrument
3. Resonance Raman spectrometer and microscope
4. Nanosecond time-resolved absorption spectrometer upgrades
5. Transient absorption system for picosecond/nanosecond transient absorption
6. Optical parametric amplifier (OPA) for infrared probe, spectrograph, infrared charge coupled device detector and opto-mechanics for time-resolved infrared spectrometer.
7. Surface infrared spectrometer
8. Transmission electron microscope EDX-detector. Note that this item is part of task 1 and represents subtask 1.2 as discussed earlier in this report.

As described below some changes were made to the list of equipment proposed in the original budget. These changes did not represent a change in scope, approach or aims of this project. All of the capabilities and experiments represented in the original budget were maintained. As described below, the most significant changes involved experiments 4, 6 and 7. Changes to experiments 6 and 7 maintain all of the capabilities of the original experiments but at a reduced cost. By combining the cost savings from these two items with incremental savings on other items relative to their budgeted cost, we were able to strengthen our transient absorption capabilities (experiments 4 and 5) as well as purchase a number of smaller items to strengthen both our laser and device fabrication facilities (Experiment 9 in Table 5 and described below).

The experiment capabilities developed are described below:

Experiment 1: Steady-State and Time Resolved Emission Spectrometer

This instrument was unchanged from the proposal but some cost savings were realized (see Table 5). This instrument is heavily used and has provided high quality characterization of both steady-state and time-resolved emission signals in many different systems, including the observation of Ruthenium(II) complex emission quenching via proton-coupled electron transfer, and the study of energy transfer kinetics between transition metal complexes in rigid media as well as in framework materials.

Experiment 2: Nanosecond Time-Resolved Infrared (TRIR) Absorption Instrument

We originally planned to purchase a laser system that could output laser pulses at a repetition rate of up to 50 kHz. For certain experiments and molecular systems, this would greatly reduce data collection time. However, for other systems, there would be insufficient time to allow for excited state relaxation between laser pulses. To combat this, we planned to purchase a pulse picker that could reduce the repetition rate sufficiently. Upon further study we determined that the pulse energy of the 50 kHz laser pulse train after passing through the pulse picker would no longer be high enough for our experiments. Furthermore, the majority of the molecular systems we are studying require a repetition rate much lower than 50 kHz. For these reasons, the EKSPLA laser system, with a repetition rate of 1 kHz or less, was purchased as the laser excitation source for the time-resolved infrared instrument. The EKSPLA system has a built-in variable repetition rate capability and consequently the pulse picker was no longer required. The purchase of the EKSPLA laser and elimination of the need for a pulse picker afforded a cost savings that was used to offset needed cost increases in other experiments in this project.

We have begun to investigate a model system for exploring the fundamentals of the proton-coupled electron transfer reaction. Specifically, we are using the instrument to monitor the electron and proton motion following photoexcitation of a tricarbonyl Rhenium complex with a hydrogen-bonded electron acceptor organic moiety. The stretching mode of the carbonyl functional groups acts as a marker for electron and proton population.

Experiment 3: Resonance Raman Spectrometer and Confocal Microscope

There were no changes in the cost of the primary components but some increases were needed in the cost of optical components. The Confocal Raman microspectrometer is regularly used for dye-sensitized photoanode experiments. Of particular interest is the binding motif of dyes onto semiconductor surfaces. These materials are at the heart of our dye-sensitized photoelectrosynthesis cell design for the production of solar fuels.

Experiment 4: Nanosecond Transient Absorption Spectrometer Upgrades

Experiment 4 involved the development of nanosecond transient absorption capabilities:

a) CCD Camera/Spectrograph:

This equipment was purchased as planned with a small increase in cost. This instrument is used heavily for a wide range of photophysical experiments including proton-coupled electron transfer and solar fuels photo-anodes. In addition, experiments will be performed on the chromophores and catalysts being developed for water splitting applications. The results of these experiments will help to form the basis for further molecular design.

b) Laser Flash Photolysis Spectrometer:

This spectrometer was purchased to replace and significantly upgrade our nanosecond transient absorption (laser flash photolysis) capabilities. This experimental capability is one of the most critical in developing a mechanistic understanding of the operation of photoelectrosynthesis cells. Our existing system had failed beyond repair and replacement was essential in order to preserve this key capability. The cost savings realized from careful budget choices in purchasing equipment for the other experiments allowed us to acquire this spectrometer.

c) Ultrasensitive Transient absorption spectrometer

It had become clear that the ability to monitor very small ($< 10^{-6}$ optical density units) changes in light absorption following pulsed excitation is absolutely critical to the

research in our center. The cost savings realized from other items funded by this award allowed us to purchase components for and build this ultrasensitive laser flash photolysis spectrometer. The components of the probe system were carefully selected to work together with an existing nitrogen/dye laser system and the detection system purchased using this award. Because this instrument allows us to perform experiments using light intensities similar to natural sunlight, the information gained from these transient absorption experiments will be of the utmost importance to our research in solar energy conversion. The experiment is being used to monitor the deleterious back electron transfer reaction following light absorption and photoinjection in ruthenium dye-sensitized titanium dioxide photoanodes.

Experiment 5: Transient Absorption System for Picosecond/Nanosecond Transient Absorption

Critical to our research is the reliable collection of pump-probe transient absorption data that spans from picoseconds out to seconds while collecting spectral information from the visible and near infrared regions. The transient absorption spectrometer was ordered as planned but the addition of a near-infrared detector with an InGaAs sensor to allow for simultaneous monitoring of photoinduced transients in the 800-1600 nm wavelength range added $30,000 to the proposed cost. This equipment provides for new transient absorption timing capabilities commonly missing from a pulsed laser spectroscopy lab. In particular, measuring the transient absorption between 1 nanosecond and 10 nanoseconds has been problematic using currently available technology. This equipment allows us to follow laser-induced kinetics from ~500 picoseconds out to milliseconds, and is being used for a multitude of research projects. Of particular value has been the ability to track the spectral changes that occur within the first several nanoseconds following light absorption. An example is the detailed photophysical study of Ruthenium(II) complexes suitable for sensitization of metal oxide electrodes.

Experiment 6: Femtosecond Stimulated Raman Spectroscopy FSRS (Ultrafast Raman)

We opted to pursue an ultrafast Raman method as opposed to the femtosecond transient IR instrument originally proposed. The Raman method provides the same information as the IR technique, and has improved sensitivity and greater flexibility. At the same time it requires less-specialized instrumentation and hence it is less expensive to implement. By switching to the Raman method we no longer required the IR Detector and Spectrograph, saving $71,625 for this one component. The change in method resulted in changes to other instrument components of this experiment as listed in Table 5. The overall cost savings from Experiment 6 was used to offset necessary increased costs in other experiments as described elsewhere in this report.

Construction of this experiment is complete. The TOPAS Ultrafast OPA is fully integrated with the pump laser system and has been used to generate a white light continuum through a sapphire window (detected using the VIS CCD). The diode array spectrometer is now fully integrated with the necessary data acquisition hardware. Software has been developed to control and synchronize instrument components such as the stage, monochromator, camera and ultrafast shutters and also to acquire, manipulate, store and analyze data.

The FSRS experiment is being used to monitor the vibrational dynamics of chromophores that are slated for use in next generation solar fuel devices. The optics on the table have also been setup to conduct transient absorption studies on ruthenium complex chromophores tethered

to a polyfluorene backbone. The pulse picker has been successfully installed in a time-resolved emission experiment and is currently being used to monitor the rate of energy transfer between ruthenium and osmium complexes tethered to metal organic frameworks and polypeptide backbones.

Experiment 7: Surface Infrared Spectrometer

We opted to purchase a $5,308 attenuated total resonance (ATR) attachment to our existing Bruker Vertex 80v FTIR spectrometer, rather than purchasing a stand-alone Surface IR instrument. While this option is considerably less-expensive ($74,667 savings), it is also a preferable technique for studying metal-oxide surfaces, allowing a broader range of capabilities and a higher signal to noise ratio. The savings realized as a consequence of this decision were used to offset the cost of equipment items required for operation of spectroscopy and photolysis experiments in the Solar Energy Instrumentation Facility (Experiment 9).

This accessory interfaces directly and seamlessly with our existing Bruker Vertex80v high resolution FTIR spectrometer. This unit makes possible infrared absorption measurements on dye-sensitized photoanodes which are typically very difficult to measure. The multiple pass operation of the attenuated total reflection crystal improves the signal to noise ratio and facilitates observation of key spectral features. We have performed experiments on monitoring dye adsorption onto titanium diode nanoparticle films by coating the nanoparticles directly onto the ATR crystal.

Experiment 8: EDX Detector for Transmission Electron Microscope

This item is part of Task 1 and represents Subtask 1.2 as described earlier in this report.

Experiment 9: **Solar Energy Spectroscopy Laboratory Equipment**

Cost savings described earlier in this section allowed the purchase of items required to develop and strengthen capabilities in the laser spectroscopy and photolysis laboratories. These items are necessary to bolster our efforts in characterizing the mechanism and reaction kinetics of catalyst components in photoelectrosynthesis cells.

a) **Electrochemical Equipment:**

Electrochemical analyzers are used to perform cyclic voltammetry and chronoamperometry experiments. In addition they are used to apply a voltage bias to photoanodes which are integral components of photoelectrosynthesis cells. Characterization hinges on being able to control the electric potential (applied bias voltage) to control the density of states within the semiconductor photoanode materials. We are currently screening various metal oxides as potential semiconductors which would not be possible without the electrochemical workstation. The electrochemical analyzers are being used in a variety of different experiments all related to dye-sensitized photoelectrosynthesis cells (DSPEC). In some cases, these instruments are used to control the applied potential between the working electrode and the counter electrode during laser flash photolysis experiments of chromophores attached to metal oxide semiconductor photoanodes. In other experiments, an electrochemical analyzer is used as an ammeter to measure the photocurrent passed between the working and counter electrodes. This transient photocurrent experiment represents a new capability for the UNC SERC, and provides insight into the molecular dynamics of a photoelectrochemical synthesis cell under real working conditions.

One of the electrochemical systems provides Electrochemical Impedance Spectroscopy (EIS) capabilities. EIS is being used to perform electrochemical evaluation of intact two electrode solar fuel devices in order to extract information about charge transport and charge transfer kinetics. The EIS capability also allows us to perform Mott Schottky analysis on semiconductor materials and to determine flat band potentials for a range of semiconductors. This information will allow us to determine whether semiconductors provide the necessary driving force for proton or carbon dioxide reduction.

b) **pH STAT Titrator**: This instrument controls solution pH during electrochemical reduction of carbon dioxide to CO and hydrocarbon products via catalysts attached to semiconductor electrode materials. The use of the pH STAT instrument is expected to improve the efficiency of catalytic CO_2 reduction and help identify the optimum pH regime for the catalysts under study. Other techniques under construction include the use of this instrument for FTIR characterization of catalyst materials attached to semiconductor coatings on a conductive ATR crystal as a function of electrolyte pH.

c) **Potentiometric Auto-titrator:** The Potentiometric Auto-titrator is being used in conjunction with a diode array spectrophotometer to determine the pKa values for the titratable protons on the ligands of certain chromophores. In addition we are using this instrument to precisely determine the pKa of the surface bound protons on the surface of various semiconductors including titanium dioxide and niobium oxide. These important experiments would not be possible without this instrument.

d) **Microwave Reaction System:** This microwave accelerated reaction system from CEM Corporation, a 1600 Watt laboratory-scale microwave instrument for rapid chemical synthesis, is now an integral part of our solar fuels research effort. We have already saved many hours of synthesis time by using the reactor in the preparation of organic ligands and inorganic metal complexes, including the archetypical $[Ru(bpy)_3]^{2+}$ complex chromophore, where bpy = 2,2'-bipyridine.

e) **Sample Preparation Equipment:** This equipment (including balances, refrigerated circulators and rotary evaporators) has enabled us to perform the necessary and critical synthesis and purification of chromophores, catalysts, and chromophore-catalyst assemblies used in the advanced spectroscopy experiments (1-7). In addition this equipment is used in the preparation and characterization of materials for photoelectrosynthesis cells designed for solar fuels production.

f) **Keithley sourcemeter system:** Critical to our experiments is the ability to simultaneously apply voltage and measure either voltage or current using a single instrument without the need for a reference electrode.

g) **Idex pumps**: These pumps are designed to flow liquid samples in high frequency time-resolved electron paramagnetic resonance spectroscopy and transient optical spectroscopy experiments. These techniques are being used to characterize mechanism and reaction kinetics of photoelectrosynthesis cells. The electrolyte solution plays a crucial role and, for certain experiments and molecular systems, it is necessary to use a micro-pump system that not only controls temperature but that continuously replenishes the photoelectrosynthesis cell with fresh electrolyte solution during the course of experiments. We routinely take advantage of the pumps by recirculating dye solution over a titanium dioxide coated ATR crystal. In this manner, we can monitor the adsorption of light-absorbing dye onto the metal oxide nanoparticles in real time.

6. PRODUCTS DEVELOPED UNDER AWARD

6.a Publications acknowledging this award:

1. Song, Wenjing; Brennaman, M. Kyle; Concepcion, Javier J.; Jurss, Jonah W.; Hoertz, Paul G; Luo, Hanlin; Chen, Chuncheng; Hanson, Kenneth G.; and Meyer, Thomas J. "*Interfacial Electron Transfer Dynamics for* $[Ru(bpy)_2((4,4'\text{-}PO_3H_2)_2bpy)]^{2+}$ *Sensitized* TiO_2 *in a Dye-Sensitized Photoelectrosynthesis Cell: Factors Influencing Efficiency and Dynamics*." J. Phys. Chem. C. **2011**, *115* (14), 7081-7091.

   This work was funded by the UNC Energy Frontier Research Center (EFRC) "Solar Fuels and Next Generation Photovoltaics", an EFRC funded by the U.S. Department of Energy, Office of Science, Office of Basic Energy Sciences, under Award DE-SC0001011, supporting MKB, JJC, JWJ, PGH, HL, KH and TJM. Partial funding for W.S. by the CCHF, an EFRC funded by the U.S. Department of Energy, Office of Science, Office of Basic Energy Sciences, under Award Number DE-SC0001298 at the University of Virginia, is also gratefully acknowledged. We acknowledge support for the purchase of instrumentation from UNC EFRC (Solar Fuels and Next Generation Photovoltaics, an Energy Frontier Research Center funded by the U.S. Department of Energy, Office of Science, Office of Basic Energy Sciences under Award Number DE-SC0001011) and UNC SERC ("Solar Energy Research Center Instrumentation Facility" funded by the US Department of Energy-Office of Energy Efficiency & Renewable Energy under Award Number DE-EE0003188).

2. Wang, Cheng; and Lin, Wenbin "Diffusion-Controlled Luminescence Quenching in Metal-Organic Frameworks" J. Am. Chem. Soc. **2011**, *133*, 4232-4235.

   We acknowledge financial support from NSF. We made use of the UNC EFRC instrumentation facility which is funded jointly by the U.S. Department of Energy Office of Science (BES, DE-SC0001011) and Office of Energy Efficiency & Renewable Energy (DE-EE0003188).

3. Lebedeva, Natalia; Schmidt, Robert; Concepcion, Javier J.; Brennaman, M. Kyle; Stanton, Ian N.; Therien, Michael J.; Meyer, Thomas J.; Forbes, Malcolm D. E. "*Structural and pH Dependence of Excited State PCET Reactions Involving Reductive Quenching of the MLCT Excited State of* $[Ru^{II}(bpy)_2(bpz)]^{2+}$ *by Hydroquinones."* J. Phys. Chem. A **2011**, *115* (15), 3346–3356.

   This material is based upon work supported as part of the UNC EFRC: Solar Fuels and Next Generation Photovoltaics, an Energy Frontier Research Center funded by the U.S. Department of Energy, Office of Science, Office of Basic Energy Sciences under Award Number DE-SC0001011, supporting the work of J. J.C. (synthesis), M.K.B. (photophysical measurements), R.D.S. and N.V.L. (electron paramagnetic resonance measurements). M.D.E.F. thanks the NSF for partial support of the TREPR instrumentation through Grant No. CHE-0809530. T.J.M. acknowledges partial support from NSF through Grant CHE-0957215 for experiment design and synthesis. M.J.T. thanks the NSF for infrastructural support through the NSEC program (DMR-04-25780). We also acknowledge support for the purchase of instrumentation from UNC EFRC (Solar Fuels and Next Generation Photovoltaics, an Energy Frontier Research Center funded by the U.S. Department of Energy, Office of Science, Office of Basic Energy Sciences under Award Number DE-SC0001011) and UNC SERC ("Solar Energy Research Center Instrumentation Facility" funded by the U.S. Department of Energy, Office of Energy Efficiency and Renewable Energy under Award Number DE-EE0003188).

4. Song, Wenjing; Glasson, Christopher R. K.; Luo, Hanlin; Hanson, Kenneth G.; Brennaman, M. Kyle; Concepcion, Javier J.; Meyer, Thomas J. *"Photoinduced Stepwise Oxidative Activation of a Chromophore-Catalyst Assembly on* TiO_2*."* J. Phys. Chem. Lett. **2011**, *2(14),* 1808-1813.

   This work was funded by the UNC Energy Frontier Research Center (EFRC) "Solar Fuels and Next Generation Photovoltaics", an EFRC funded by the U.S. Department of Energy, Office of Science, Office of Basic Energy Sciences under award DE-SC0001011, supporting M.K.B., J.J.C., and K.H. We acknowledge funding by the Army Research Office through grant W911NF-09-1-0426 for partial support for work by W.S. and C.G. on compound synthesis, separation, and characterization. Partial funding for W.S. and C.G. for work on interfacial photophysics dynamics and spectroelectrochemistry, by the CCHF,

an EFRC funded by the U.S. Department of Energy, Office of Science, Office of Basic Energy Sciences, under award number DE-SC0001298 at the University of Virginia, is gratefully acknowledged. We acknowledge support for the purchase of instrumentation from UNC EFRC (Solar Fuels and Next Generation Photovoltaics, an Energy Frontier Research Center funded by the U.S. Department of Energy, Office of Science, Office of Basic Energy Sciences under award number DE- 289SC0001011) and UNC SERC ("Solar Energy Research Center Instrumentation Facility" funded by the U.S. Department of Energy, Office of Energy Efficiency and Renewable Energy under award number DE-EE0003188)

5. Stewart, David J.; Brennaman, M. Kyle; Bettis, Stephanie E.; Wang, Li; Binstead, Robert A.; Papanikolas, John M.; Meyer, Thomas J. "*Competing Pathways in the* photo-*Proton-Coupled Electron Transfer Reduction of* fac-*[Re(bpy)(CO)$_3$(4,4'-bpy)]$^+$ by Hydroquinone,"* J. Phys. Chem. Lett., **2011**, *2(15)*, 1844-1848.

   This work has been supported by the National Science Foundation under Grant CHE-0957215 (supporting D.J.S.) and by the UNC EFRC: Solar Fuels and Next Generation Photovoltaics, an Energy Frontier Research Center funded by the U.S. Department of Energy, Office of Science, Office of Basic Energy Sciences under Award Number DE-SC0001011 (supporting M.K.B, S.E.B., L.W. and R.A.B). We acknowledge support for the purchase of instrumentation from the UNC EFRC under U.S. DOE award number DE-SC0001011 as listed above and UNC SERC ("Solar Energy Research Center Instrumentation Facility" funded by the US Department of Energy – Office of Energy Efficiency & Renewable Energy under Award Number DE-EE0003188).

6. Kenneth Hanson, M. Kyle Brennaman, Kelsey A. Parker, Rudresh Ghosh, Hanlin Luo, Wenjing Song, Michael R. Norris, Christopher R. Glasson, Javier J. Concepcion, Rene Lopez, and Thomas J. Meyer. *"Structure-Property Relationships of Phosphonate-Based Ruthenium(II) Bipyridine Dyes on Nanocrystalline TiO_2 in an Aqueous Environment,"* In preparation.
7. Akitaka Ito, David J. Stewart, Fang Zhen, M. Kyle Brennaman, and Thomas J. Meyer. *"Excited State Dynamics in Rigid Media: Evidence for Long-Range Energy Transfer."* In preparation.
8. Kenneth Hanson, M. Kyle Brennaman, Hanlin Luo, Christopher R. Glasson, Javier J. Concepcion, and Thomas J. Meyer. *"Photostability of Metal Oxide Bound Ruthenium(II) Tris(bipyridine) Derivatives."* In preparation.
9. Courtney Hadsell, Greg Mogilevsky, M. Kyle Brennaman, Kenneth Hanson, Thomas J. Meyer, and Yue Wu. *"Variation of Stability, Transient Absorbance, and Device Performance of [Ru(bpy)$_2$((4,4'-PO$_3$H$_2$)$_2$bpy)]$^{2+}$-Sensitized Multilayered, Titania Nanotube and Nanosheet Electrodes with pH and Annealing Temperature."* In preparation.
10. Aaron K. Vannucci, Jonathan F. Hull, Robert A. Binstead, Javier J. Concepcion, and Thomas J. Meyer, *"Water Oxidation Intermediates Applied to Catalysis: Benzyl Alcohol Oxidation"*, In preparation.

The five papers already in print (1-5) are attached to this report (PDF).

6.b <u>Patents</u>: No patent applications to date.

7. COST STATUS

The approved budget for this award had two components:

1. Required UNC Cost Share $279,736 – construction of new laboratory space for the Solar Energy Fabrication Laboratory (Task 1, Subtask 1.1 as shown in Table 4)
2. DOE funding of $1,000,000 for instrumentation for the fabrication laboratory (Task 1, Subtask 1.2) and the Solar Energy Spectroscopy Laboratory (Task 2), as shown in Table 5.

TABLE 4. TASK 1 SUBTASK 1.1 CONSTRUCTION COSTS (Chapman Hall upfit)

	Contractor	Description	Proposal Budget	Expended Budget
1	Wilson Architects	Design services for Instrumentation Lab	$32,950	$32,950
SUBTOTAL DESIGN			$32,950	$32,950
2	Engineering Specialties Co. Inc	Add openings for doors and windows	$9,765	$9,765
3	Ajay Glass & Mirror Company	Glass, freight, labor	$6,785	$6,785
4	Sears Contract Inc.	Construction materials, laboratory benches & furniture	$59,496	$59,496
5	Precision Walls Inc.	Materials, labor to install wall grid in lab, corridor and ceilings	$4,816	$4,816
6	Furniture Moods Inc.	Cove floor base molding materials and installation labor	$795	$795
7	Mansion Decorators of NC Inc.	Painting - materials and labor	$3,159	$3,159
8	Contract Shading Systems	Blackout laboratory shades - materials and labor	$3,576	$3,576
9	Sunland Fire Protection Inc.	Sprinkler system materials and labor	$2,729	$2,729
10	John J. Kiran LLC	Mechanical contractor - plumbing	$98,319	$98,319
11	L.L. Vann Electric	Wiring, conduit, lighting materials & labor	$8,649	$8,649
12	NC Communications	Cable, data jacks, data ports, outlets materials and labor	$5,051	$5,051
13	Subguard Insurance	Construction Insurance 1.5% - Subguard	$3,647	$3,647
SUBTOTAL CONSTRUCTION			$246,786	$246,786
GRAND TOTAL DESIGN + CONSTRUCTION			**$279,736**	**$279,736**

The goal of Task 2 was the purchase and installation of selected equipment for research. Three key milestones for Task 2 were established for the one-year award period as shown below and in Table 1.

KEY MILESTONES:

- Listed Equipment ordered — 100% complete by 6/30/2011
- Listed Equipment delivered. — 100% complete by 8/14/2011
- Listed Equipment installed, operational and available for use by researchers under the guidance of trained personnel. — 100% complete by 8/14/2011

Table 5: Task 2: Solar Energy Spectroscopy Laboratory Development
Purchase & Installation of Equipment 8/15/2010 – 8/14/2011
All items are associated with Task 2 of the proposal except item #8 (Task 1, Sub-Task 1.2)

Experiment	Equipment Item	ORIGINAL Proposal Budget ($)	Status	Order Date	Expenditure as of 8/14/2011 ($)	FINAL Budget ($)	Cost Savings ($)
1. Steady-State/Time Resolved Emission Spectrometer	Emission spectrometer	$125,191	Operational	6/14/10	$112,556	$112,556	$12,635
	Optistat-DN Cryostat	$28,500	Operational	10/18/10	$15,085	$15,085	$13,415
2. ns-Time Resolved Infrared (TRIR)	EKSPLA Nd:YAG High-repetition Laser System	$105,275	Operational	6/11/10	$38,960	$38,960	$66,315
	Electro-optic Pulse Picker	$15,000	No longer planned			$0	$15,000
	Optical components	$7,000	No longer planned			$0	$7,000
	Digital Oscilloscope	$8,000	No longer planned			$0	$8,000
3. Resonance Raman Spectrometer	RENISHAW Spectrometer + Microscope + Detector	$175,000	Operational	6/9/10	$175,000	$175,000	$0
	Optical components	$8,000	No longer planned			$0	$8,000
4. ns-Transient Absorption Upgrades	CCD camera/spectrograph	$77,595	Operational	6/14/10	$80,916	$80,916	($3,321)
	Laser Flash Photolysis Spectrometer		Operational	8/19/10	$109,370	$109,370	($109,370)
	Transient Absorption Detector		Operational	9/13/10	$16,231	$16,231	($16,231)
	Optomechanics	$7,000	Operational	9-11/2010	$11,557	$11,557	($4,557)
	Monochromator, Grating		Operational	6/17/11	$32,369	$32,369	($32,369)
	Laser Power Meter		Operational	2/8/11	$5,149	$5,149	($5,149)
	Optistat Collar and Lid		Operational	1/26/11	$2,040	$2,040	($2,040)
5. TA Spectrometer	Transient Absorption Spectrometer EOS-VIS	$90,000	Operational	6/9/10	$120,678	$120,678	($30,678)
	2-D Sample Holder		Operational	1/31/11	$5,046	$5,046	($5,046)
6. *fs* IR Spectrometer ---> Ultrafast Raman	TOPAS Ultrafast OPA	$41,980	Operational	5/17/10	$41,185	$41,185	$795
	IR Detector + Spectrograph	$71,625	No longer planned			$0	$71,625
	VIS CCD	$20,000	Operational	8/18/10	$2,905	$2,905	$17,095
	Spectrograph	$12,779	No longer planned			$0	$12,779
	Optical Delay Stage	$12,000	No longer planned			$0	$12,000
	Autocorrelator Delay Stage	$5,000	No longer planned			$0	$5,000
	Diode Array Spectrometer	$5,000	Operational	11/19/10	$13,710	$13,710	($8,710)
	Data Acquisition Hardware	$6,000	Operational	1/4/11	$501	$501	$5,499
	Digital Oscilloscope	$8,000	No longer planned			$0	$8,000
	Optomechanics + shutters	$22,000	Operational	10/10-1/11	$7,524	$7,524	$14,476
	Pulse Picker		Operational	1/31/2011	$11,215	$11,215	($11,215)
7. Surface IR Spectrometer	Attenuated Total Reflectance accessory + parts	$79,975	Operational	10/18/10	$5,328	$5,328	$74,647
8. TEM EDX Detector *TASK 1*	Transmission Electron Microscope EDX-Detector	$69,080	Operational	1/6/11	$69,080	$69,080	$0
9. Solar Energy Spectroscopy Laboratory Development	(a) Electrochemical Analyzers (4)		Operational	7/10-11/10	$28,537	$28,537	($28,537)
	(b) pH STAT Titrator		Operational	1/11/11	$6,457	$6,457	(6,457)
	(c) Potentiometric Auto-titrator		Operational	9/8/10	$23,955	$23,955	($23,955)
	(d) MW Reaction System		Operational	6/22/11	$12,703	$12,703	($12,703)
	(e) Sample Preparation Equip.		Operational	8/5/10	$35,409	$35,409	($35,409)
	(f) Keithley sourcemeter system		Operational	9/9/10	$5,332	$5,332	($5,332)
	(g) Idex Micropump System		Operational	9/17/10	$11,202	$11,202	($11,202)
	TOTALS	**$1,000,000**			**$1,000,000**	**$1,000,000**	**$0**

THE JOURNAL OF PHYSICAL CHEMISTRY C

ARTICLE

pubs.acs.org/JPCC

Interfacial Electron Transfer Dynamics for $[Ru(bpy)_2((4,4'\text{-}PO_3H_2)_2bpy)]^{2+}$ Sensitized TiO_2 in a Dye-Sensitized Photoelectrosynthesis Cell: Factors Influencing Efficiency and Dynamics

Wenjing Song, M. Kyle Brennaman, Javier J. Concepcion, Jonah W. Jurss, Paul G. Hoertz, Hanlin Luo, Chuncheng Chen, Kenneth Hanson, and Thomas J. Meyer*

Department of Chemistry, University of North Carolina at Chapel Hill, Chapel Hill, North Carolina 27599-3290, United States

Supporting Information

ABSTRACT: Nanosecond laser flash photolysis and photocurrent measurements have been used to investigate use of $[(Ru(bpy)_2(4,4'\text{-}(PO_3H_2)_2bpy)]^{2+}$ attached to TiO_2 nanoparticle films, TiO_2-Ru^{II}, in a dye-sensitized photoelectrosynthesis cell (DSPEC) configuration for H_2 production. In these experiments, laser flash excitation of TiO_2-Ru^{II} and rapid injection lead to $TiO_2(e^-)-Ru^{III}$ with subsequent $TiO_2(e^-)-Ru^{III} \rightarrow TiO_2-Ru^{II}$ back electron transfer monitored on the nsec time scale with and without added triethanolamine (TEOA) and deprotonated ethylenediaminetetraacetic tetra-anion ($EDTA^{4-}$) as irreversible electron transfer donors. With added TEOA or $EDTA^{4-}$, a competition exists between back electron transfer and scavenger oxidation with the latter leading to H_2 production in the photoelectrosynthesis cell. Reduction of $TiO_2(e^-)-Ru^{III}$ by both TEOA and $EDTA^{4-}$ occurs with $k_D \sim 10^6\ M^{-1}\ s^{-1}$. $EDTA^{4-}$ is a more efficient scavenger by a factor of ~3 because of a more favorable partition equilibrium between the film and the external solution. Its increased scavenger efficiency appears in incident photon-to-current conversion efficiency (IPCE) measurements, in electron collection efficiencies (η_{coll}), and in photocurrent measurements with H_2 production. Evaluation of electron collection efficiencies by transient current measurements gave $\eta_{coll} \sim 24\%$ for TEOA and ~ 70% for $EDTA^{4-}$. The dynamics of back electron transfer are minimized, and collection efficiencies, photocurrents, and hydrogen production are maximized by application of a positive applied bias consistent with the results of I−V measurements. A pH dependent plateau is reached at ~0 V at pH = 4.5 ($EDTA^{4-}$) and at ~ −0.4 V at pH 6.7 (TEOA). The difference is qualitatively consistent with the influence of pH on electron population in trap states below the conduction band and the role they play in back electron transfer. The excitation dependence of IPCE measurements matches the spectrum of TiO_2-Ru^{II} with IPCE values ~3 times higher for $EDTA^{4-}$ than for TEOA as noted above. Absorbed photon-to-current efficiency (APCE) values are light-intensity dependent because of the effect of multiple injection events and the influence of increasing trap site electron densities on back electron transfer. The key to efficient H_2 production is minimizing back electron transfer. Application of a sufficiently positive potential relative to E_{CB} for TiO_2 accelerates loss of electrons from the film in competition with back electron transfer allowing for H_2 production with efficiencies approaching 14.7% under steady-state irradiation.

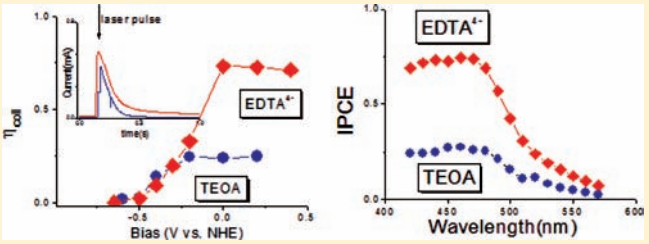

INTRODUCTION

Understanding of dye-sensitized solar cells (DSSCs) has evolved significantly by application of both transient and steady-state photocurrent measurements and theory. These devices are based on nanostructured oxide semiconductors with appropriate band energies. Photocurrents and potentials are induced by molecular excitation, injection, and intra-film diffusional electron transfer. They provide a basis for a family of photovoltaic devices which have reached solar conversion efficiencies in excess of 10%.[1−4]

The same configuration that also integrates catalytic elements for multielectron−multiproton catalysis of solar fuel half reactions in dye-sensitized photolectrosynthesis cells (DSPECs) is also a promising approach.[5−8] Examples of photoelectrochemical water splitting, $2H_2O \rightarrow O_2 + 2H_2$, based on the DSPEC approach have been reported but with relatively low efficiencies.[9−11]

A key element for continued progress in this area is exploration of the separate photodriven half reactions for water/H^+ or CO_2 reduction and water oxidation. Developing an adequate understanding of the underlying mechanism and integrating both dynamic and photocurrent measurements to maximize efficiencies are essential to the successful evolution of this strategy.

Received: January 5, 2011
Published: March 16, 2011

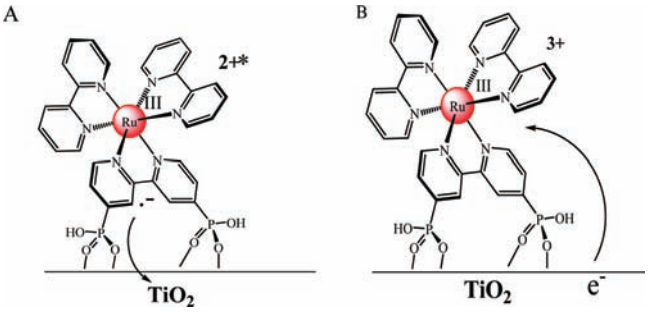

Figure 1. Schematic illustrations of surface injection, A, and back electron transfer, B, for $[Ru(bpy)_2(4,4'\text{-}(PO_3H_2)_2bpy)]^{2+}$ on TiO_2, TiO_2-Ru^{II}.

We report here results on a DSPEC for photoelectrochemical H_2 production in an aqueous environment. It is based on excitation and injection by the phosphonate derivatized complex $[Ru(bpy)_2(4,4'\text{-}(PO_3H_2)_2bpy)]^{2+}$ on TiO_2, TiO_2-Ru^{II} (Figure 1), in the presence of added reductive scavengers triethanolamine (TEOA) and ethylenediaminetetraacetic tetra-anion ($EDTA^{4-}$). In the absence of a scavenger, injection is followed by back electron transfer, eq 1. With added scavenger, there is a competition between back electron transfer and reductive capture of Ru^{III}, which creates excess electrons for H_2 production at a physically separated cathode.

$$TiO_2-Ru^{II} \xrightarrow{h\nu} TiO_2-Ru^{II}* \xrightarrow[\text{injection}]{k_{inj}}$$

$$TiO_2(e^-)-Ru^{III} \xrightarrow[\text{back electron transfer}]{k_{bet}} TiO_2-Ru^{II} \qquad (1)$$

The results of related studies have been reported. Direct band gap excitation of TiO_2 in the presence of an added reductive scavenger in a TiO_2/Nafion/Pt polymer membrane assembly led to sustained photocurrents and hydrogen generation.[12] The photochemical response of TiO_2 was extended into the visible in Ti^{3+}-doped/intercalated TiO_2 photoanodes with methanol added as the reductive scavenger.[13,14] A zinc-substituted cytochrome *c* assembly sensitized TiO_2 nanoparticle with EDTA added as a reductive scavenger achieved 10% hydrogen generation quantum yield at codeposited Pt.[15] Reisner et al. and Woolerton et al. utilized injection from the metal-to-ligand charge transfer (MLCT) excited states of $[Ru(bpy)_2(4,4'\text{-}(PO_3H_2)_2bpy)]^{2+}$ on nanoparticle TiO_2 with added reductive scavenger triethanolamine to achieve hydrogen evolution by coadsorbed hydrogenase enzymes.[16,17] Hambourger and coworkers investigated a photoelectrochemical biofuel cell on the basis of excitation and injection from a porphyrin sensitizer on TiO_2 with hydrogen evolution at *Clostridium acetobutylicum* [FeFe]-hydrogenase HydA adsorbed on pyrolytic graphite or carbon felt electrodes.[18,19] Caramori et al. have reported on photoelectrochemical hydrogen production based on phosphonic acid derivatized Ru(II) polypyridyl complexes with added sacrificial donors such as ascorbic acid and I^-.[20]

We report here a related, detailed study on H_2 evolution in a DSPEC based on $[Ru(bpy)_2(4,4'\text{-}(PO_3H_2)_2bpy)]^{2+}$ as the sensitizer on TiO_2 with added reductive scavengers TEOA and EDTA. The goal was to utilize a combination of laser flash photolysis, transient photocurrent, and steady-state photocurrent measurements to explore the underlying details of hydrogen evolution in a DSPEC configuration including factors that dictate cell efficiency.

EXPERIMENTAL SECTION

Materials. Aqueous solutions were prepared from water purified by use of a Milli Q purification system. Lithium perchlorate (99.999% trace metal basis), 70% perchloric acid (99.999%), triethanolamine (TEOA, 98%), ethylenediaminetetraacetic acid (EDTA-disodium salt) aqueous solution (0.1 M), titanium isopropoxide, isopropanol, and hydroxypropylcellulose were used as received from Sigma-Aldrich. Fluorine-doped tin oxide (FTO) coated glass (Hartford Glass Co.; sheet resistance 15 Ω/cm^2) was cut into 11 mm × 70 mm strips and was used as the substrate for TiO_2 nanoparticle films. $[Ru^{II}(bpy)_2((PO_3H_2)_2bpy](Cl)_2$ was prepared and was purified by literature procedures.[21]

Preparation of Photoanodes. TiO_2 films on FTO were prepared as previously described.[22] Films were 11 mm × 25 mm with thicknesses of 5 μm controlled by Scotch tape. The slides were immersed in slightly acidic aqueous solutions of $[Ru(bpy)_2(4,4'\text{-}(PO_3H_2)_2bpy)]Cl_2$ (0.02−0.1 mM, pH ∼ 6) for 24 h at room temperature in the dark to give TiO_2-Ru^{II} photoanodes. Surface coverages (Γ in mol/cm^2) were estimated by absorbance measurements of slides in neutral solution (baseline corrected) by using the expression $\Gamma = A(\lambda)/\varepsilon(\lambda)/1000$.[23] In these analyses, $\varepsilon(\lambda)$ = 15 100 M^{-1} cm^{-1} was the maximum molar extinction coefficient at 457 nm for the complex in aqueous solution at pH ∼ 6 determined by inductively coupled plasma mass spectrometry (ICP-MS), and $A(\lambda)$ was the maximum absorbance of TiO_2-Ru^{II} photoanodes(463 nm) (Supporting Information, Figure S1). This gave a maximum surface coverage (Γ_0) of ∼8.7 × 10^{-8} mol cm^{-2} (∼1.8 × 10^{-8} mol cm^{-2} μm^{-1}). Significant loss of complex was observed upon immersion in neutral aqueous solution apparently because of dissolution of a microcrystalline overlayer of the complex salt occluded on the surface as observed earlier.[24] Slides were soaked in water for an additional 12−36 h to remove excess complex from the surface before measurements were undertaken. Following this treatment, Γ values of <5 × 10^{-8} mol cm^{-2} were obtained.

Measurements. *Transient Absorption.* Transient absorption experiments were performed by using nanosecond laser pulses produced by a Spectra-Physics Quanta Ray Nd:YAG laser (532 nm, 5−7 ns, operated at 1 Hz, beam diameter 0.5 cm) combined with an optical parametric oscillator (OPO). White light probe pulses generated by a 150 W pulsed Xe lamp were passed through the sample at 90° relative to excitation and were collected by an Applied Photophysics laser kinetic spectrometer consisting of an f3.4 monochromator and Hamamatsu R928 photomultiplier tubes (PMT). The output from the PMT was sent to a LeCroy WavePro 7100A digital oscilloscope interfaced to a PC. Experiment synchronization and control was achieved by electronics and LabView software of local design with the assistance of a Stanford Research Systems, Inc. DG 535 pulse generator. Single wavelength kinetics at each probe wavelength was the result of 50 laser shots.

A customized three-arm (Figure S2 of the Supporting Information), one-compartment photoelectrochemical cell (PEC) was employed in the transient absorption measurements with applied bias. The arm for the photoanode was a 10 mm path length pyrex curvette. A platinum gauze was used as photocathode and Ag/AgCl as the reference electrode. The photoanode was inserted

at a 45° angle into a homemade Teflon seat located in the cuvette. The photoanode was allowed to reach equilibrium with electrolyte for ~40 min, and the background current was stabilized at the applied bias before laser excitation. All experiments were carried out under argon at 22 ± 2 °C unless otherwise specified. Current measurement and applied bias were performed on a Pine Wavenow potentialstat. All bias values are referenced versus normal hydrogen electrode (NHE).

The excitation energy of the incident laser pulses was 4 ± 0.2 mJ at 532 nm. For a photoanode with ~5×10^{-8} mol cm^{-2} with absorbance of about 0.1 at 532nm surface coverage, ~3.7×10^{-9} mol of $TiO_2(e^-)-Ru^{III}$ would be produced per laser pulse assuming that all absorbed photons lead to injection and in support of this assumption, residual emission under these conditions is negligible.[25]

Quantitative analysis of transient absorption−time profiles following laser flash excitation utilized the triexponential expression in eq 2a to calculate an average lifetime $\langle\tau\rangle$, or the decays were characterized by $t_{1/2}$, the time for half the total absorbance change to occur, eq 2b.[25]

$$A = A_1 e^{-t/\tau_1} + A_2 e^{-t/\tau_2} + A_3 e^{-t/\tau_3}$$
$$\tau_{ave} = \langle\tau\rangle = \Sigma A_i \tau_i^2 / \Sigma A_i \tau_I \qquad (2a)$$

$$t_{1/2} = t \text{ at } A_t = A_0/2 \qquad (2b)$$

Photoelectrochemistry. Single-wavelength and excitation-dependent IPCE (incident photon-to-current conversion efficiency) measurements were performed in the photoelectrochemical cell used for transient absorption measurments. Light from a 75 W xenon lamp in an Oriel Photomax housing was passed through an Oriel Cornerstone 260 monochromator to produce monochromatic light with a bandwidth of 10 nm. Photon flux was measured by a UDT S370 optometer coupled with a UDT 260 detector. Photocurrents were measured by a Wavenow potentiostat under short-circuit conditions with both auxiliary and reference electrodes connected to a platinum mesh electrode held at 0 V or with an applied bias. IPCE values were calculated using eq 3 with J_{ph} the averaged photocurrent in amps observed within 30 s of irradiation, λ the wavelength of the incident light in nm, and P_0 the incident photon flux in W.

$$\text{IPCE}(\lambda) = (1240 \text{ eVnm}) \times J_{ph}/\lambda \times P_0 \qquad (3)$$

Alternately, illumination was provided by a spectral light engine from Lumencor (λ_{max} = 445 nm, 20 nm bandwidth, output ~ 3.7−100 mW cm^{-2}). The light source was integrated with a Newport optical fiber and focusing/imaging beam probe. The irradiation beam diameter was 10 mm.

Hydrogen Evolution. Photoelectrochemically evolved hydrogen was quantified by headspace gas analysis with methane as the internal standard on a gas chromatograph (SRI 8610C-GC) equipped with a 5 Å molecular sieve column and helium ionization detector (HID) with helium as carrier gas. The instrument was calibrated with samples containing known concentrations of methane and H_2 in Ar.

RESULTS

Transient Absorption. Regeneration of Ru^{II} following laser flash excitation (532 nm) and electron injection into TiO_2 by back electron transfer, k_{bet} in eq 1, was monitored at 450 nm in the presence and absence of external electron transfer donors TEOA and $EDTA^{4-}$. The pH was adjusted by addition of $HClO_4$ with ionic strength maintained at 0.2 with added $LiClO_4$.

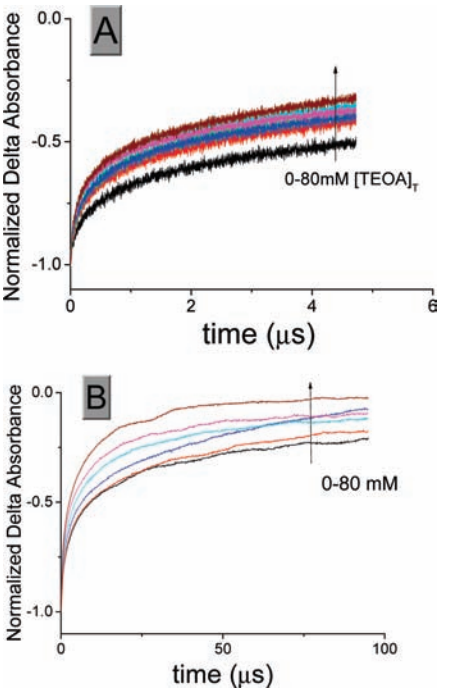

Figure 2. Normalized absorbance−time traces at 450 nm in milli-OD units (ΔmOD) following laser flash excitation of TiO_2-Ru^{II} without (black) and with added triethanolamine (TEOA) (1−80 mM) over 5 μs (A) and 100 μs (B) time windows. Excitation at 532 nm (3.9 mJ/pulse), Γ = 2×10^{-8} mol cm^{-2}, pH = 6.7, I = 0.2 M with added $LiClO_4$ 0.13−0.20 M. [TEOA] = 0.074 $[TEOA]_T$.

As described in the Experimental Section, kinetic parameters were obtained by analysis of absorbance−time traces by defining the time for half the absorbance change to occur, $t_{1/2}$ eq 2b, for the complete data set or as the average of a triexponential fit for the first 5 μs, eq 2a. The latter accounted for 50−70% of the total absorbance change. Attempted fits to multiple second order expressions[26−29] or to the Kohlrausch−Williams−Watts distribution function[30,31] were unsuccessful.

As shown in the typical transient absorbance−time traces in Figure 2, regeneration of Ru^{II} after injection is accelerated with added TEOA as a sacrificial electron transfer donor. Under the conditions of our experiments at pH = 6.7, TEOA is distributed between the acid−base forms, $^+HN(CH_2CH_2OH)_3$ and $N(CH_2CH_2OH)_3$, eq 4a, with $pK_a(^+HTEOA)$ = 7.8. Control of pH was important in these experiments to ensure long-term surface stability of the adsorbed complex. Given the acid−base equilibrium, in eq 4a, the concentration of TEOA is given by eq 4b with $[TEOA]_T$ as the total concentration of TEOA, [TEOA] + [$^+$HTEOA].

$$^+HN(CH_2CH_2OH)_3 \rightleftharpoons H^+ + N(CH_2CH_2OH)_3 \qquad K_a \qquad (4a)$$

$$[TEOA] = K_a[TEOA]_T/([H^+] + K_a) \qquad (4b)$$

The notable decrease in $t_{1/2}$ for reappearance of Ru^{II} with added TEOA is consistent with a competition for

Scheme 1

$$TiO_2\text{-}Ru^{II} \xrightarrow{h\nu} TiO_2\text{-}Ru^{II}* \xrightarrow{k_{inj}} TiO_2(e^-)\text{-}Ru^{III} \xrightarrow{k_{bet}(k_d)} TiO_2\text{-}Ru^{II}$$

$$2TiO_2(c^-)\text{-}Ru^{III} + TEOA \xrightarrow{k_D} 2TiO_2(c^-)\text{-}Ru^{II} + TEOA_{ox}$$

Table 1. Dynamics of TiO_2-Ru^{II} Regeneration as a Function of [TEOA] at pH 6.7, I = 0.2 M (by $LiClO_4$) by Analysis of the Data in Figure *1*; the Total Absorbance Change, ΔA in mOD Units, Is Also Listed

$[TEOA]_T$ (mM)	ΔA (mOD)	percent recovery in 5 μs (%)	$t_{1/2}$ (μs)[a]	τ_{ave} (μs)[b]
0	−53.2	50	5.2	16.6
1	−57.1	58	2.5	13.1
2	−48.8	60	2.1	12.3
4	−48.7	62	1.9	12.7
10	−50.9	64	1.7	12.2
20	−50.6	63	1.5	12.4
80	−50.4	68	1.2	8.7

[a] Equation 2b. [b] Equation 2a; 5 μs data only.

$TiO_2(e^-)-Ru^{III}$, produced at the photoanode, between $TiO_2(e^-)-Ru^{III} \rightarrow TiO_2-Ru^{II}$ back electron transfer and reductive scavenging by TEOA, Scheme 1.

A kinetic model for TEOA oxidation in the TiO_2 films is shown in eqs 5−7 with the associated rate law in eqs 8 and 9. The first step is partitioning of TEOA from the acid−base equilibrium in the external solution, eq 4a, into the film, $TEOA_f$. The partition equilibrium constant is given by K_p. The protonation state/distribution between acid and base forms within the film is unknown.

The base form of TEOA is redox active and, after partitioning, is oxidized by $TiO_2(e^-)-Ru^{III}$ by rate constant k_D in eq 6. The importance of diffusion and partitioning into the film is shown by the appearance of rate saturation in TEOA above ~10 mM in the external solution, Table 1 and Figure 2.

$$TEOA \underset{k_{-p}}{\overset{k_p}{\rightleftharpoons}} TEOA_f \qquad K_p \tag{5}$$

$$TiO_2(e^-) - Ru^{III} + TEOA_f \xrightarrow{k_D} TiO_2(e^-) - Ru^{II} + TEOA^{+\cdot} \tag{6}$$

$$TiO_2(e^-) - Ru^{III} + TEOA^{+\cdot} \xrightarrow{-e^-,2H^+} TiO_2(e^-) - Ru^{II} + TEOA_{ox} \qquad \text{(rapid)} \tag{7}$$

TEOA is an irreversible electron transfer donor. The one electron oxidized product $TEOA^{+\bullet}$ is unstable toward disproportionation to give TEOA and $TEOA_{ox}$ with $k = 3.3 \times 10^6\ M^{-1}\ s^{-1}$.[32] In the presence of strong oxidants, it undergoes rapid, further $1e^-$ oxidation to give $TEOA_{ox}$ which is assumed in eq 7.

Approximate rate constants for TEOA oxidation in the films were obtained by comparing the results of nsec transient absorbance measurements with and without added TEOA. In this analysis, rate constants were taken to be $1/t_{1/2}$ for the whole data set. This is clearly an approximation because neither $t_{1/2}$ nor τ_{ave} gives an accurate representation of the complete data set. The 5 μs data set used to calculate τ_{ave} represents only 50−70% of the total absorbance change.

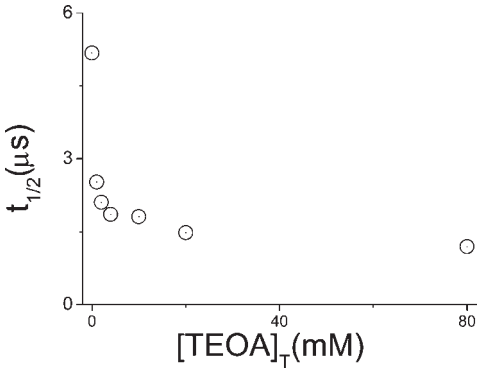

Figure 3. Variations in half time ($t_{1/2}$) (eq 2b) for the entire A(t)−t data set for Ru(II) regeneration following laser flash excitation.

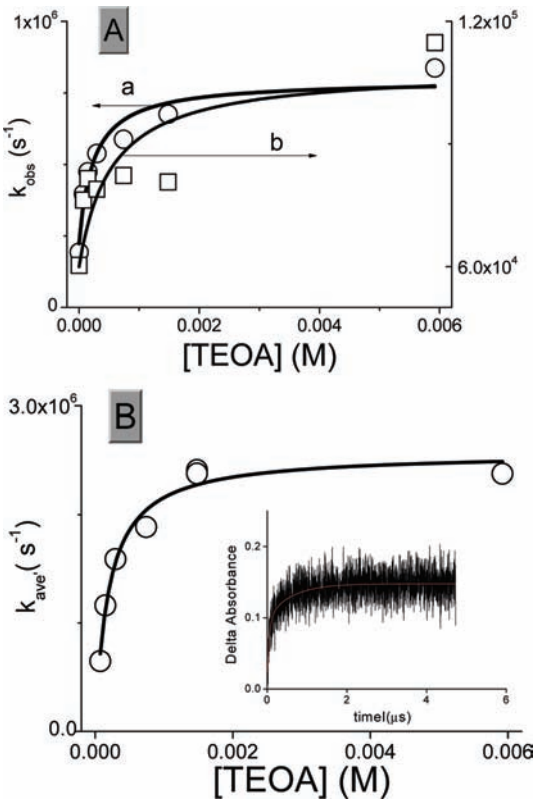

Figure 4. Plots of k_{obs} vs [TEOA] with [TEOA] = 0.074 $[TEOA]_T$ (A) (a) $k_{obs} = 1/t_{1/2}$ (○) and (b) $k_{obs} = 1/\tau_{ave}$ with $k_{obs} = 1/\tau_{ave}$ and τ_{ave} obtained from a fit of the absorbance−time traces in Figure 2A to eq 2a for the 5 μs data (□). (B) k_{obs} obtained from a fit of the ΔA_t−time difference traces to the biexponential function in eq 10a. The inset shows a ΔA_t−time trace in the presence of 10 mM TEOA and a fit of the data to eq 10a with $A_1 = 0.075$, $\tau_1 = 57.8$ ns, $A_2 = 0.049$, and $\tau_2 = 600$ ns with $\tau_{ave} = 530$ ns.

Plots of the data in Table 1 fit to eq 9 with $k_{obs} = 1/t_{1/2}$ and $k_{obs} = 1/\tau_{ave}$ are shown in Figure 4A (curves a and b). Fits to the $1/t_{1/2}$ data in Figure 4A are shown fit with the parameters $k_o = 2.2 \times 10^5\ s^{-1}$, $K_p = 4200\ M^{-1}$, and $k_D = 2.9 \times 10^5\ M^{-1}\ s^{-1}$. Similarly, for the $k_{obs} = 1/\tau_{ave}$ data of curve b, $k_o = 6.0 \times 10^4\ s^{-1}$, $K_p = 1850$

Table 2. Summary of Rate and Equilibrium Constants for TEOA Reduction of $TiO_2(e^-)-Ru^{III}$ from the Data in Figure 4[a]

k_{obs} (s^{-1})	k_D (M^{-1} s^{-1})	K (M^{-1})	k_0 (s^{-1})
$1/t_{1/2}$ (eq 2b)	2.9×10^5	4190	2.2×10^5
$1/\tau_{ave}$ (eq 2a)	2.4×10^4	1830	6.0×10^4
$1/\tau_{ave}'$ (eq 10b)	1.3×10^6	5220	

[a] At pH = 6.7, I = 0.2 M.

M^{-1}, and $k_D = 2.4\times10^4$ M^{-1} s^{-1}. Differences between the two methods of analysis are expected given the different fractions of data they represent and their limited insight into underlying film dynamics.

An alternate treatment gave more satisfactory results. In this treatment, absorbance−time traces in the absence of TEOA were subtracted from traces with added TEOA as a way of isolating the donor contribution to electron-transfer dynamics. The insert in Figure 4B shows the results of this analysis when applied to a typical data set. The ΔA_t−time traces, with $\Delta A_t = A_{t,D} - A_{t,o}$ and with $A_{t,D}$ and $A_{t,o}$ being the absorbances at time t with and without added TEOA, were fit to the biexponential kinetic decay function in eq 10a. A typical trace is shown in the inset in Figure 4B. The physical origin for the biexponential kinetics is not clear. It may be a manifestation of a distribution of sites and rate constants rather than representing two discrete dynamic processes.

Application of eq 9 to k_{obs} values obtained from the difference procedure, $k_{obs,D}$, in Figure 4B gave $K_p = 5220$ M^{-1} and $k_D = 1.3 \times 10^6$ M^{-1} s^{-1}. The value of k_D is in good agreement with $k = 6 \times 10^6$ M^{-1} s^{-1} for TEOA oxidation by $Ru(bpy)_3^{3+}$ in solution.[33] Rate and equilibrium constants obtained by all three procedures are summarized in Table 2.

$$d[TiO_2 - Ru^{II}]/dt = -d[TiO_2 - Ru^{III}]/dt = \{k_o + 2k_D K_P[TEOA]/(1 + K_p[TEOA])\}[TiO_2 - Ru^{III}] \quad (8)$$

$$k_{obs} = (k_o + 2k_D K_p[TEOA]_f) \quad (9)$$

$$A = A_1 e^{-t/\tau 1} + A_2 e^{-t/\tau 2} \quad (10a)$$

$$\tau_{ave} = \langle\tau\rangle = (A_1\tau_1^2 + A_2\tau_2^2)/(A_1\tau_1 + A_1\tau_2) \quad (10b)$$

H_4EDTA. EDTA is also an irreversible electron transfer donor with redox properties related to those of TEOA.[32] The final of the four pK_a values for −COOH group is 2.67. At pH > 2.7, the acid is deprotonated and in the $EDTA^{4-}$, tetra-anionic form. The pK_a value for the phosphonate protons for surface-bound $[Ru(bpy)_2(4,4'\text{-}(PO_3H_2)_2bpy)]^{2+}$ is ∼2,[34] eq 11a. For the surface $Ti-OH_2^+/TiOH$ acid−base equilibrium, pK_a ∼ 5.[35−38] Surface oxidation of TiO_2-Ru^{II} to TiO_2-Ru^{III} above pH ∼ 2 results in TiO_2-Ru^{III} and a net positive charge on the complex, eq 11b. Between pH = 3 and 5 with H_4EDTA completely deprotonated, there may be an electrostatic affinity for $EDTA^{4-}$ both at the surface and to the complex.

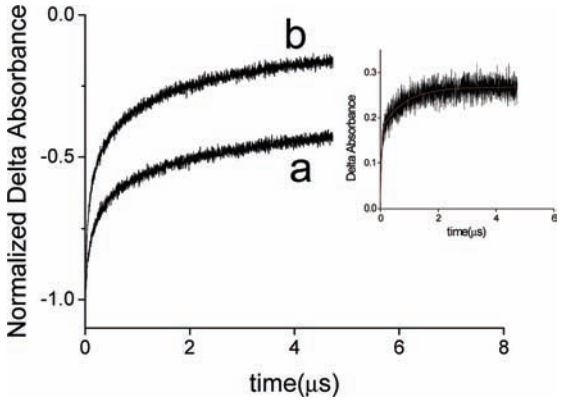

Figure 5. Normalized transient absorbance−time traces after laser flash excitation of TiO_2-Ru^{II} at 532 nm in a 20 mM acetate buffer at pH = 4.5, 0.18 M in $LiClO_4$ in trace a and with 20 mM added H_4EDTA in trace b: 4.0 mJ/pulse, monitored at 450 nm, surface coverage, $\Gamma \sim 2 \times 10^{-8}$ mol cm^{-2}. Inset: $\Delta A_t = A_{t,D} - A_{t,o}$ vs time trace; trace b − trace a fit to eq 10a with $A_1 = 0.079$, $\tau_1 = 808$ ns, $A_2 = 0.160$, and $\tau_2 = 39$ ns with $\tau_{ave} = 740$ ns. Equivalent results were obtained at 10 mM and 40 mM EDTA.

$$(TiO_2)2Ti - \{((OP(O)(OH))_2bpy)Ru(bpy)_2\}^{2+} = (TiO_2)2Ti - \{((OP(O)O)_2bpy)Ru(bpy)_2\}^0 + 2H^+ \quad (11a)$$

$$(TiO_2)2Ti - \{((OP(O)O)_2bpy)Ru(bpy)_2\}^0 - e^- \rightarrow (TiO_2)2Ti - \{((OP(O)O)_2bpy)Ru(bpy)_2\}^+ \quad (11b)$$

An enhanced affinity for $EDTA^{4-}$ in the films is evident from an enhanced reactivity compared to TEOA. This can be seen in the absorbance−time traces in Figure 5. The data in Figure 5 show that with 20 mM H_4EDTA added at pH = 4.5, ∼85% of TiO_2-Ru^{II} is recovered from $TiO_2(e^-)-Ru^{III}$ after 5 μs compared to 68% with 80 mM added TEOA at pH 6.7.

Transient Absorption. Kinetic Analysis. By comparing transient absorption−time data with and without added TEOA or $EDTA^{4-}$, Figures 4 and 5, it is clear that, even with $EDTA^{4-}$ as scavenger, there is a competition between reduction of Ru^{III} by the scavenger and back electron transfer from the semiconductor. The fraction of excitation events that results in back electron transfer was used to estimate the maximum absorbed photon-to-current efficiency (APCE) that could be extracted in a photoelectrochemical cell assuming that all efficiency losses were from back electron transfer.

In principle, APCE values can be calculated by using eqs 12 and 13[39] with Φ_{inj} the injection efficiency and η_{coll} the electron collection efficiency. The injection efficiency is given by $k_{inj}/(k_{inj} + 1/\tau)$ with k_{inj} the injection rate constant and τ the excited state lifetime in the absence of quenching.

In eq 13, k_0 is the back electron transfer rate constant in the absence of donor, and k_{obs} is the observed rate constant with added donor. As mentioned above, it was not possible to obtain a satisfactory mathematical representation of the data over the entire absorbance−time range. Rather than rely on the kinetic data, electron collection efficiencies were calculated from the difference in absorbance changes with, $\Delta A_{max,D}$, and without added scavenger, $\Delta A_{max,o}$, eq 14. For the representative

Scheme 2

Photoanode

$$TiO_2\text{-}Ru^{II} \xrightarrow{h\nu} TiO_2\text{-}Ru^{II}* \xrightarrow{k_{inj}} TiO_2(e^-)\text{-}Ru^{III} \xrightarrow{k_{BET}(k_0)} TiO_2\text{-}Ru^{II}$$

$$2\ TiO_2(e^-)\text{-}Ru^{III} + TEOA \xrightarrow{k_D} 2\ TiO_2(e^-)\text{-}Ru^{II} + TEOA_{ox} + 2\ H^+$$

Cathode

$$2\ TiO_2(e^-) + 2H^+ \xrightarrow{Pt,k_{H2}} H_2$$

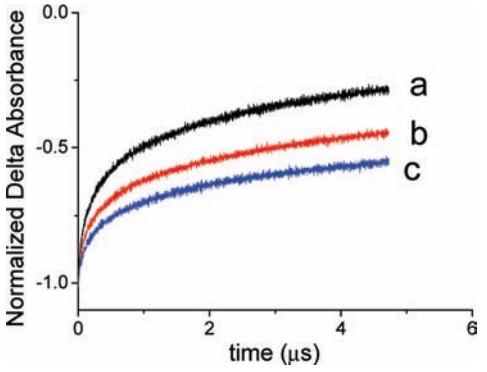

Figure 6. Transient absorption−time traces following excitation of TiO_2−Ru^{II} in the presence of 80 mM TEOA at pH 6.7 ($\Gamma \sim 3.0 \times 10^{-8}$ mol cm^{-2}, λ_{ex} = 532 nm, 4.0 mJ/pulse) with monitoring at 450 nm. Trace a, open circuit (black); trace b, short circuit (red); trace c, 0.2 V bias (blue) vs NHE.

absorbance−time traces in Figure 1, this gave $\eta_{coll} \sim 18\%$ with 80 mM added TEOA at pH 6.7 and 28% for 20 mM $EDTA^{4-}$ at pH = 4.5, Figure 3.

$$APCE = \Phi_{inj} \times \eta_{coll} \quad (12)$$

$$\eta_{coll} k_D[D]/(k_0 + k_D[D]) = (k_{obs} - k_0)/k_{obs} \quad (13)$$

or

$$\eta_{coll} = [\Delta A_{max,D} - \Delta A_{max,0})]/A_{initial} \quad (14)$$

Transient Absorption. Kinetic Analysis in a Complete Photoelectrochemical Cell. We also explored back electron transfer dynamics in a complete circuit with hydrogen evolution at the cathode, Scheme 2. In these experiments, saturation conditions in TEOA (80 mM at pH 6.7) and $EDTA^{4-}$ (20 mM at pH = 4.5) were used. Shown in Figures 5 and 6 are kinetic traces for TiO_2−Ru^{II} regeneration both under open-circuit and short-circuit conditions and with 0.2 V applied bias (vs NHE).

Equations 12−14 give ideal efficiencies on the basis solely of competition between back electron transfer and reductive scavenging. In a PEC under operating conditions, the maximum efficiency is obtained when all photoproduced electrons reach the cathode for proton reduction to hydrogen.[18] This entails thermal activation from trap states to the TiO_2 conduction band with electron transport to the FTO collector electrode followed by H_2 production at the Pt cathode. Electron collection and H_2 production are in competition with back electron transfer.[40−43]

In Figures 6 and 7 are shown absorbance−time traces with added TEOA and $EDTA^{4-}$ under open-circuit and short-circuit

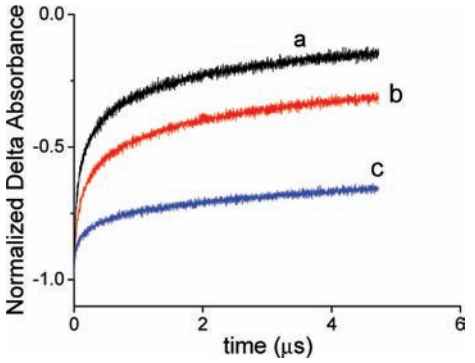

Figure 7. As in Figure 6 with 20 mM added $EDTA^{4-}$ at pH 4.5.

conditions and with a 0.2 V applied bias (vs NHE). Under these conditions, quasi-Fermi level at TiO_2 was defined by the $1/2H_2/H^+$ couple (short circuit) or external bias.[40,43−46] As shown by the data in Figures 6 and 7, there is a marked decrease in back electron transfer rate under closed-circuit conditions with added reductive scavenger both with and without applied bias consistent with electron loss and H_2 production.

On the basis of Absorbance changes under open-circuit conditions and with 0.2 V applied bias (vs NHE) and the data for TEOA in Figure 6, it can be estimated that ∼28% of the injected electrons escape to the external circuit with 0.2 V applied bias. Only ∼17% escape without bias. With $EDTA^{4-}$ at pH 4.5 as donor, this value increases to ∼50% at 0.2 V applied bias (Figure 7). Electron collection efficiencies obtained by transient photocurrent measurements following laser flash photolysis were comparable, see below.

Kinetic parameters—$t_{1/2}$, τ_{ave}, fraction of ΔA_{max} recovery after 5 μs—obtained by analysis of absorbance−time traces as a function of applied bias are listed in Table 3. Data for both TEOA at pH 6.7 and $EDTA^{4-}$ at pH = 4.5 are shown plotted against $t_{1/2}$ in Figure 8.

From the data with added TEOA, the half time for back electron transfer decreases with applied bias reaching a plateau at ∼−0.4 V (curve a). At this potential, the time scale for back electron transfer is minimized and electron collection efficiency is maximized with no further advantage with increases in applied bias. For $EDTA^{4-}$ at pH 4.5, a similar behavior is observed with an onset potential at ∼0 V versus NHE (curve b). The difference in behavior with pH is qualitatively predictable on the basis of the pH dependences of E_{CB} and associated TiO_2 trap states.[18,38,44,46−51] Back electron transfer dynamics in the absence of added sacrificial donors displays a comparable pH dependent bias effect consistent with this interpretation (Figure S3 of the Supporting Information).

Transient Photocurrents. Transient photocurrent measurements following laser flash photolysis operated at 1 Hz were also investigated under the conditions used in the transient absorption measurements. The response time of the measurements, 1 ms, was limited by the response time of the potentiostat. On the basis of earlier results, spontaneous growth in photocurrent following injection from TiO_2−$Ru^{II}*$ is expected on the sub-ms time scale depending on light intensity and film thickness.[43,52−55] For a typical DSSC solar cell with the I_3^-/I^- carrier couple, the half time for photocurrent rise under 1 sun conditions is typically <1 ms.

In Figure 9 are shown current−time traces obtained after laser flash excitation of TiO_2−Ru^{II} in the presence of TEOA and $EDTA^{4-}$ and without electron transfer donor (in 0.2 M $LiClO_4$).

Table 3. Summary of Back Electron Transfer Kinetic Parameters with Applied Bias (vs NHE)[a]

	fraction of recovery in 5 μs (%)		$t_{1/2}$ (μs)		τ_{ave} (μs) (5 μs time scale)[b]	
	TEOA[c]	EDTA[d]	TEOA[c]	EDTA[d]	TEOA[c]	EDTA[d]
open circuit	72	86	1.0	0.19	7.7	5.5
short circuit	56	69	3.0	0.76	14	11
Bias (vs NHE)						
−0.8	100		0.012		0.012	
−0.6	84	99	0.4	0.02	4.8	0.55
−0.5	66	94	1.4	0.09	9.4	2.7
−0.4	50	84	4.7	0.29	15	5.9
−0.3	48	73	5.5	0.72	21	8.6
−0.2	41	61	6.0	1.7	20	14
0	47	43	5.7	8.0	19	24
0.2	45	34	6.0	13	22	34
0.4	47	34	6.1	14	20	35

[a] λ_{ex} = 532 nm, 4 mJ/pulse, monitored at 450 nm, $\Gamma \sim 2.5 \times 10^{-8}$ mol cm^{-2}. [b] See text, eq 2a. [c] TEOA: 80 mM, pH 6.7. [d] EDTA: 20 mM, pH 4.5.

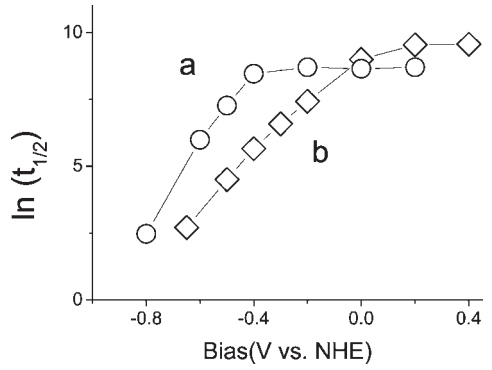

Figure 8. Plot of ln($t_{1/2}$, ns); vs applied bias for the data in Table 3 with added TEOA (curve *a*, o), pH 6.7; $EDTA^{4-}$ (curve *b*, ◊), pH 4.5.

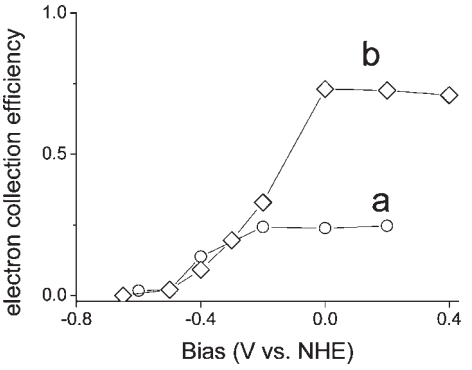

Figure 10. Variation in electron collection efficiency (eq 15) with external bias in 80 mM TEOA at pH 6.7 (curve a, o) and in 20 mM $EDTA^{4-}$ at pH 4.5 (curve b, ◊).

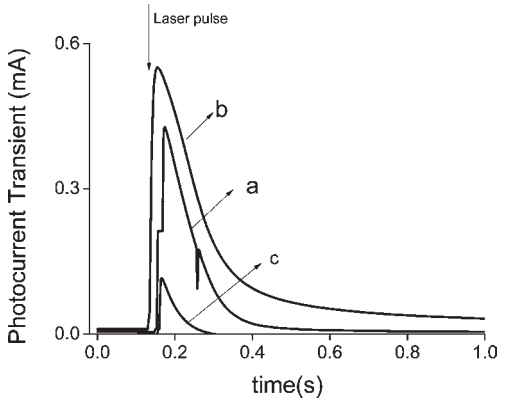

Figure 9. Current−time traces following laser flash excitation (a) with 80 mM added TEOA at pH 6.7, (b) with 20 mM $EDTA^{4-}$ at pH 4.5, and (c) in the absence of donors with 0.2 V bias vs NHE. $\Gamma \sim 3.0 \times 10^{-8}$ mol cm^{-2}, λ_{ex} = 532 nm, 4.0 mJ/pulse.

The electron collection efficiency in the external circuit (η) was calculated from these data as the ratio of charge passed (e_{ex}, from integrated current−time traces) and the number of injected electrons (e_{inj}), eq 15. The latter was calculated from photons that were absorbed by photoanode assuming unit injection yield (eq 16, where I_0 is the laser energy/pulse in einstein and A is the absorbance of photoanode at 532 nm).

$$\eta = e_{ex}/e_{inj} \quad (15)$$

$$e_{inj} = I_0 \times (1 - 10^{-A}) \quad (16)$$

Electron collection efficiencies plotted as a function of applied bias are shown in Figure 10 for both TEOA and $EDTA^{4-}$. In the absence of reductive scavenger, $\eta \sim 2\%$. For TEOA, a plateau in the efficiency curve is reached at ∼−0.3 V versus NHE and at 0 V for $EDTA^{4-}$. This result is consistent with the applied bias dependence obtained in the transient absorption experiments with a decrease in back electron transfer rate because of a decreased electron population in trap states lying below the conduction band. In the plateau region, integrated current−time traces are bias independent. Enhanced current spikes and increasingly rapid current transient decays as the bias is increased within this region are consistent with voltage-controlled discharge of electrons collected at the FTO collector electrode by electron transfer to the cathode (Figure S4 of the Supporting Information).

IPCE and APCE. Incident photon-to-current conversion efficiency measurements in the PEC configuration were performed

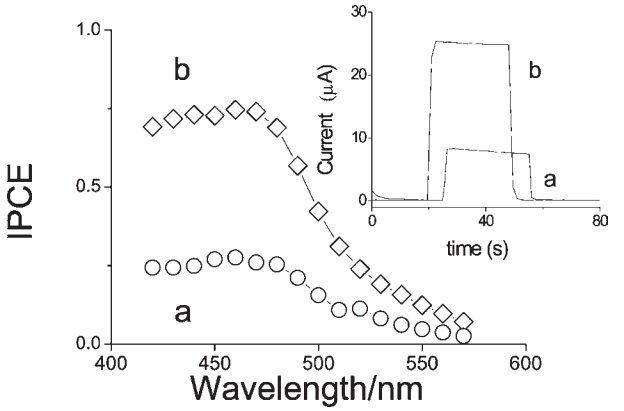

Figure 11. Wavelength-dependent incident photon-to-current conversion efficiencies in the presence of 20 mM TEOA at pH 6.7 (curve a) and 20 mM EDTA at pH 4.5 (curve b). Averaged photocurrents obtained within 30 s of initiation of the irradiation period were used to calculate IPCE. Insert: current−time profiles with 460 nm illumination (~0.1 mW). Surface coverage was $\Gamma \sim 4.5 \times 10^{-8}$ mol cm^{-2}.

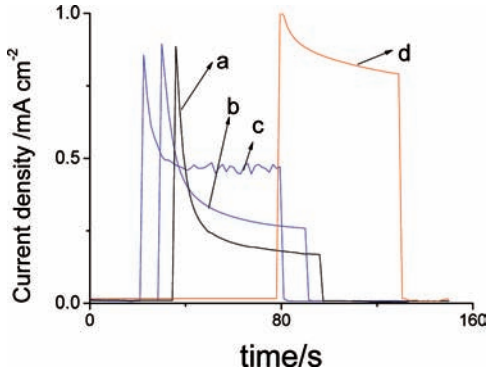

Figure 12. Current−time profiles under steady state illumination (~9.5 mw/cm^2 at 445 ± 10 nm) in the presence of (a) 20 mM TEOA pH = 6.7, (b) 80 mM TEOA, (c) 80 mM TEOA with mass flow by argon bubbling in the photoanode compartment, and (d) 20 mM EDTA^{4-} at pH = 4.4. Bias: 0.2 V vs NHE. Surface coverage was $\Gamma = 3.2 \times 10^{-8}$ mol cm^{-2}.

in the presence of 80 mM TEOA at pH = 6.7 and with 20 mM EDTA^{4-} at pH = 4.5 with 0.2V bias. The excitation dependence of the IPCE response (Figure 11) matches the spectrum of the TiO_2−Ru^{II} photoanode. IPCE values were ~3 times lower for TEOA as electron donor than for EDTA^{4-} consistent with the higher scavenging efficiency of EDTA^{4-}.

With TEOA as scavenger, photocurrents decreased significantly with time as incident light intensity was increased. Data are shown in Figure 12 at ~9.6 mW cm^{-2} at 445 ± 10 nm with 20 mM TEOA as scavenger (Figure 12, curve a). The long-term decrease in steady-state photocurrents appears to arise from depletion of TEOA in the films with the rate of solution to film equilibration, TEOA → TEOA$_f$, rate-limiting. The latter conclusion is supported by the higher steady state currents reached at 80 mM added TEOA (Figure 12, curves a and b) and by the effect of promoted mass flow at the electrode by Ar bubbling (curve c). With its higher affinity in the film, photocurrent losses with time for EDTA^{4-} were far less (Figure 12, curve d).

As shown in Figure 13 with 20 mM EDTA^{4-} at pH = 4.4, absorbed photon-to-current conversion efficiencies (APCE), eq 17, are

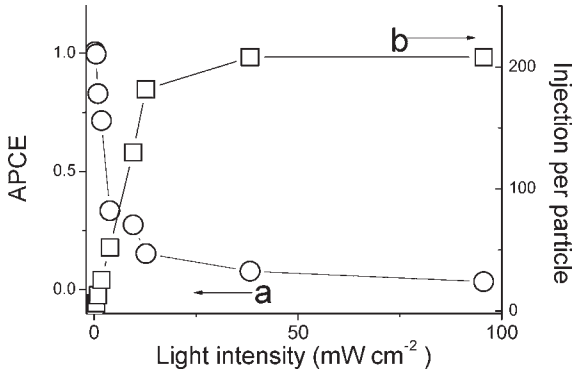

Figure 13. Plot of APCE (curve a) in 20 mM EDTA^{4-} at pH 4.4 (○) and the corresponding number of injection events per particle (□) (curve b, Calculation in Supporting Information) plotted vs light intensity.

light-intensity dependent. In eq 17, A_λ is the absorbance of the photoanode at wavelength λ (background subtracted for light scattering/reflection at underivatized TiO_2). Variations in APCE with incident light intensity are shown in Figure 13 with 445 nm irradiation (curve a). At low intensities, APCE approaches 1, but a significant decrease is observed above 2 mW cm^{-2}. By 90 mW cm^{-2}, the APCE has fallen to ~3%

$$\text{APCE} = \text{IPCE}/(1 - 10^{-A_\lambda}) \qquad (17)$$

The origin of the light-intensity effect has been discussed and documented elsewhere.[25,41,57] At high intensities, multiple injection events occur per TiO_2 nanoparticle (Figure 13, curve b). Multiple injection enhances the rate of back electron transfer, $TiO_2(e^-)$−Ru^{III} → TiO_2−Ru^{II}, at the expense of reductive capture by added EDTA^{4-}. Back electron transfer is nonlinear in electron concentration while the scavenger at the photoanode is limited.[31,57] The calculated number of injected electrons per nanoparticle is shown on the right axis in Figure 13. In DSSCs with I^- as scavenger in nonaqueous solvents, efficiency losses from this effect are far less.[53] Film concentrations of the added scavenger are higher, and rates of reduction of Ru(III) are more rapid.[58,59]

Current-voltage Profiles. Cyclic voltammetry (CV) measurements were conducted on TiO_2−Ru^{II} with 80 mM added TEOA at pH 6.7 and 20 mM added EDTA^{4-} at pH 4.4 with and without illumination. As shown in Figure 14, the significant reductive current in the CV with an onset at ~−0.3 V (vs NHE) at pH 6.7 is due to reduction of TiO_2 trap sites with reoxidation of $TiO_2(e^-)$ occurring at E_p = −0.55 V versus NHE, close to the TiO_2 conduction band potential at pH 7.[47] This wave shifts to −0.4 V at pH = 4.5 consistent with the expected pH dependence (Figure 15).

The photocurrent dependence on applied bias is consistent with the bias-dependent results described above including the bias dependence of $\ln(t_{1/2})$ shown in Figure 8. It arises from enhanced back electron transfer at negative potentials because of an increase in electron population of trap states.

H_2 Evolution. Photoelectrochemical hydrogen evolution measurements were conducted with both TEOA, 20 mM at pH = 6.7 (Figure 16, trace a), and EDTA^{4-}, 20 mM at pH = 4.5 (Figure 16, trace b), as donors under ~3.7 mW cm^{-2} illumination with 0.2 V applied bias (vs NHE). Photocurrents with EDTA^{4-} as donor were stable and were sustained for hours.

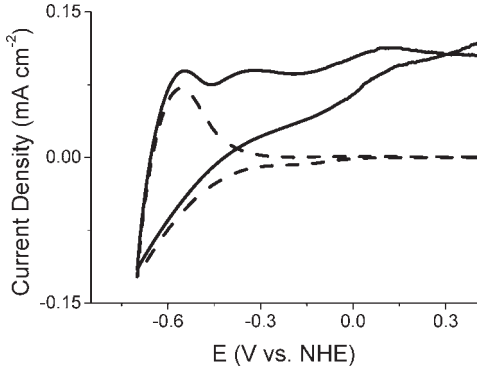

Figure 14. Cyclic voltammetry scans of TiO_2—Ru^{II} at 5 mV/s in the presence of 80 mM TEOA at pH 6.7 under illumination (3.7 mW cm^{-2} at 445 nm, solid line) and in the dark (dashed line).

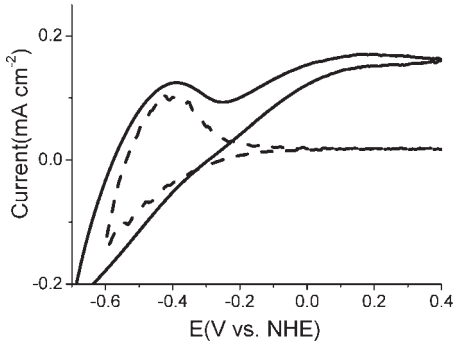

Figure 15. As in Figure 14, I—V profile for TiO_2—Ru^{II} with 20 mM added EDTA at pH 4.4 (~3 mW at 445 nm, solid line) in the dark (dashed line).

Generation of H_2 was confirmed by quantitative gas chromatography (GC) measurements. In a series of three consecutive experiments in Figure 16, 0.37 μM of H_2 was generated in trace a with added TEOA after 2000 s. In the experiments in b, with added $EDTA^{4-}$, the amount of H_2 generated during three consecutive photoelectrolysis intervals over a total photolysis period of 600 s was 0.51, 0.5, and 0.45 μM. In these experiments, H_2 was produced with a Faradaic efficiency of 92.3 ± 1.8%. Quantum yields (QY) for hydrogen production were found to be 14.7% for $EDTA^{4-}$, that is, 29.4% on a per equivalent basis over a 10 min photolysis period.

Quantum yields were calculated from eq 18 with I_o the incident absorbed light intensity at the excitation wavelength (445 nm) and $A(445)$ the absorbance at 445 nm.

$$QY = n_{H2}/(I_0 \times (1 - 10^{-A(445)}) \times t) \qquad (18)$$

DISCUSSION

The results of the combined transient absorption, transient photocurrent, steady-state photocurrent, and H_2 evolution studies at TiO_2—Ru^{II} with added reductive scavengers TEOA and $EDTA^{4-}$ are insightful and mechanistically revealing. They reinforce earlier conclusions pointing to the importance of back electron transfer in dictating the overall efficiency of electron collection and H_2 production in the DSPEC configuration with added scavengers.

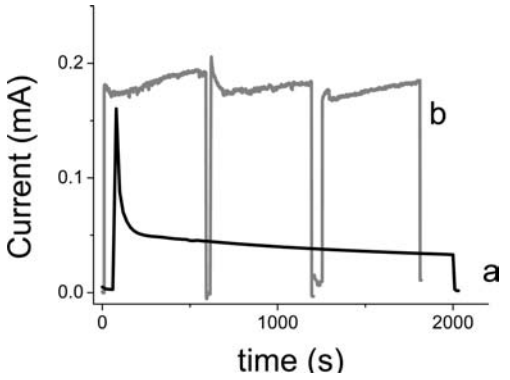

Figure 16. Photoelectrolysis current—time profiles: (a) 20 mM TEOA at pH 6.7 over 2000 s with A_{445} = 1.0 and (b) 20 mM $EDTA^{4-}$ at pH 4.4 over three 600 s photolysis intervals, A_{445} = 0.37.

Back electron transfer is dominated by electron occupation of trap states lying below the conduction band. They are populated following rapid injection and thermal equilibration. Rates of back electron transfer to the surface-bound oxidized dye ($TiO_2(e^-)$—Ru^{III} → TiO_2—Ru^{II}) are nonlinear in electron occupation as shallow states become occupied.[30,31,42,60] Both conduction band and trap state energies are pH dependent increasing by 59 mV/pH unit over a broad pH range.[44,46,50]

With added reductive scavengers, I^- in nonaqueous solvents and $EDTA^{4-}$ in water, a competition is set up between reductive capture of TiO_2—Ru^{III} by back electron transfer and reaction with the scavenger. Back electron transfer is influenced by changes in pH, applied bias, and light intensity and their influence on trap state occupation. Capture by added scavengers is kinetically limited by partitioning into the film, K_p in eq 5, and by the rate constant for reduction, k_D in Scheme 1.

This kinetic model provides a systematic basis for explaining both our transient absorption and photocurrent results with added reductive scavengers TEOA and $EDTA^{4-}$.Comparison of transient absorption kinetics for back electron transfer with and without added TEOA at pH = 6.7 has allowed both the partition equilibrium constant for TEOA into the film TEOA = $TEOA_f$ ($K_p \sim 5200\ M^{-1}$) and the rate constant for $TEOA_f$ reduction of TiO_2—Ru^{III} ($k_D \sim 1 \times 10^6\ M^{-1}\ s^{-1}$) to be evaluated. Reduction of TiO_2—Ru^{III} by $EDTA^{4-}$ occurs with a comparable rate constant, but $EDTA^{4-}$ is more effective as a scavenger by a factor of ~3 because of its higher affinity in the film possibly because of an electrostatic component.

Light intensity, concentration, and stir rate dependent photocurrents are observed for TEOA as scavenger. At high incident light intensities, steady-state photocurrents appear to be rate limited by TEOA diffusion into the film which can be increased by agitation by argon bubbling. Photocurrents with $EDTA^{4-}$ as scavenger under comparable conditions are relatively stable with little loss of photocurrent over periods of hours even at relatively high incident light intensities.

Analysis of open-circuit absorbance—time traces gave electron collection efficiencies, η_{coll}, of ~18% with 80 mM added TEOA at pH 6.7 and 28% for 20 mM $EDTA^{4-}$ at pH = 4.5. Marked decreases in back electron transfer rates under closed-circuit conditions occur with added reductive scavengers both with and without applied bias. On the basis of ΔA changes with TEOA at pH = 6.7 under open-circuit conditions and with 0.2 V applied bias, ~28% of injected electrons escape to the external circuit

under open-circuit conditions and ~17% under short-circuit conditions. With $EDTA^{4-}$ at pH 4.5, the collection efficiency increases to ~50% at 0.2 V bias. These values are qualitatively consistent with values obtained by transient photocurrent measurements.

The half time ($t_{1/2}$) for back electron transfer from transient absorbance measurements increases with applied bias reaching a plateau at ~−0.4 V for TEOA at pH = 6.7 and at ~0 V for $EDTA^{4-}$ at pH 4.5. The pH dependence of the plateau behavior is qualitatively consistent with the influence of pH on the potentials of the conduction band and associated trap states.

Electron collection efficiencies reach a plateau with applied bias reaching limiting values of ~70% for $EDTA^{4-}$ at pH = 4.5 and ~24% for TEOA at pH = 6.7 because of the 3 times increased scavenger efficiency of $EDTA^{4-}$. Photocurrents and hydrogen production are maximized and back electron transfer is minimized as the bias potential is increased to the plateau region, ~−0.4 V at pH = 6.7 and 0 V at pH = 4.5 again reflecting a decrease in back electron transfer because of a decrease in electron occupation in low-lying trap states as the bias potential is increased.

The excitation dependence of the IPCE response matches the spectrum of TiO_2−Ru^{II} with IPCE values ~3 times higher for $EDTA^{4-}$ than for TEOA under saturation conditions in electron-transfer donor. APCE values are highly light intensity dependent because of the effect of multiple injection in increasing trap state occupation and its influence on back electron transfer.

On the basis of voltammetry measurements, the bias dependence leads to decreasing photocurrents at potentials below $E \sim E_{CB}$. This is due to population of trap states in TiO_2 which increases back electron transfer and is due to the loss of driving force for electron transfer to the cathode. With 0.2 V applied bias, H_2 is produced in high Faradaic efficiency (92.3 ± 1.8%) but with limiting quantum yields of 2% for TEOA and 14.7% for $EDTA^{4-}$.

CONCLUSIONS

On the basis of the combined results of transient absorption, photocurrent, and IPCE measurements, we have obtained clear insight into the factors that dictate the efficiency of hydrogen production in a DSPEC configuration based on $[(Ru(bpy)_2(4,4'\text{-}(PO_3H_2)_2bpy)]^{2+}$ attached to TiO_2 (TiO_2−Ru^{II}) with added reductive scavengers $EDTA^{4-}$ and TEOA. The key is the competition between back electron transfer—which is affected by pH, light intensity, and applied bias—and reduction of $TiO_2(e^-)$−Ru^{III} by the added scavengers. The latter is limited by the affinity of the film for the scavenger and its rate of reduction in the film.

At low incident light intensities, APCE values approach 1 maximizing cell efficiency and H_2 production. The key to successful operation of the cell under these conditions with low incident light intensities is the low electron occupation of trap states to minimize back electron transfer. The use of an applied bias for water splitting at TiO_2 was first noted by Fujishima and Honda in their experiments based on direct band gap excitation.[61] The bias effect arises from electron occupation of low-lying trap states and their influence on back electron transfer and is a fundamental limitation. The interplay between light intensity and applied bias to achieve high efficiencies poses a fundamental limitation in the use of TiO_2 in these applications.

ASSOCIATED CONTENT

Supporting Information. This material is available free of charge via the Internet at http://pubs.acs.org.

AUTHOR INFORMATION

Corresponding Author
*tjmeyer@unc.edu.

ACKNOWLEDGMENT

This work was funded by the UNC Energy Frontier Research Center (EFRC) "Solar Fuels and Next Generation Photovoltaics", an EFRC funded by the U.S. Department of Energy, Office of Science, Office of Basic Energy Sciences, under Award DE-SC0001011, supporting MKB, JJC, JWJ, PGH, HL, KH and TJM. Partial funding for W.S. by the CCHF, an EFRC funded by the U.S. Department of Energy, Office of Science, Office of Basic Energy Sciences, under Award Number DE-SC0001298 at the University of Virginia, is also gratefully acknowledged. We acknowledge support for the purchase of instrumentation from UNC EFRC (Solar Fuels and Next Generation Photovoltaics, an Energy Frontier Research Center funded by the U.S. Department of Energy, Office of Science, Office of Basic Energy Sciences under Award Number DE-SC0001011) and UNC SERC ("Solar Energy Research Center Instrumentation Facility" funded by the US Department of Energy-Office of Energy Efficiency & Renewable Energy under Award Number DE-EE0003188).

REFERENCES

(1) O'Regan, B.; Gratzel, M. *Nature* **1991**, *353*, 737.
(2) Desilvestro, J.; Graetzel, M.; Kavan, L.; Moser, J.; Augustynski, J. *J. Am. Chem. Soc.* **1985**, *107*, 2988.
(3) Gao, F.; Wang, Y.; Zhang, J.; Shi, D.; Wang, M.; Humphry-Baker, R.; Wang, P.; Zakeeruddin, S. M.; Grätzel, M. *Chem. Commun.* **2008**, 2635.
(4) Nazeeruddin, M. K.; De Angelis, F.; Fantacci, S.; Selloni, A.; Viscardi, G.; Liska, P.; Ito, S.; Takeru, B.; Grätzel, M. *J. Am. Chem. Soc.* **2005**, *127*, 16835.
(5) Treadway, J. A.; Moss, J. A.; Meyer, T. J. *Inorg. Chem.* **1999**, *38*, 4386.
(6) Alstrum-Acevedo, J. H.; Brennaman, M. K.; Meyer, T. J. *Inorg. Chem.* **2005**, *44*, 6802.
(7) Concepcion, J. J.; Jurss, J. W.; Brennaman, M. K.; Hoertz, P. G.; Patrocinio, A. O. v. T.; Murakami Iha, N. Y.; Templeton, J. L.; Meyer, T. J. *Acc. Chem. Res.* **2009**, *42*, 1954.
(8) Gagliardi, C. J.; Westlake, B. C.; Kent, C. A.; Paul, J. J.; Papanikolas, J. M.; Meyer, T. J. *Coord. Chem. Rev.* **2010**, *254*, 2459.
(9) Brimblecombe, R.; Koo, A.; Dismukes, G. C.; Swiegers, G. F.; Spiccia, L. *J. Am. Chem. Soc.* **2010**, *132*, 2892.
(10) Li, L.; Duan, L.; Xu, Y.; Gorlov, M.; Hagfeldt, A.; Sun, L. *Chem. Commun.* **2010**, *46*, 7307.
(11) Youngblood, W. J.; Lee, S.-H. A.; Kobayashi, Y.; Hernandez-Pagan, E. A.; Hoertz, P. G.; Moore, T. A.; Moore, A. L.; Gust, D.; Mallouk, T. E. *J. Am. Chem. Soc.* **2009**, *131*, 926.
(12) Seger, B.; Kamat, P. V. *J. Phys. Chem. C* **2009**, *113*, 18946.
(13) Meekins, B. H.; Kamat, P. V. *ACS Nano* **2009**, *3*, 3437.
(14) Zuo, F.; Wang, L.; Wu, T.; Zhang, Z.; Borchardt, D.; Feng, P. *J. Am. Chem. Soc.* **2010**, *132*, 11856.
(15) Astuti, Y.; Palomares, E.; Haque, S. A.; Durrant, J. R. *J. Am. Chem. Soc.* **2005**, *127*, 15120.
(16) Reisner, E.; Powell, D. J.; Cavazza, C.; Fontecilla-Camps, J. C.; Armstrong, F. A. *J. Am. Chem. Soc.* **2009**, *131*, 18457.

(17) Woolerton, T. W.; Sheard, S.; Reisner, E.; Pierce, E.; Ragsdale, S. W.; Armstrong, F. A. *J. Am. Chem. Soc.* **2010**, *132*, 2132.
(18) Hambourger, M.; Gervaldo, M.; Svedruzic, D.; King, P. W.; Gust, D.; Ghirardi, M.; Moore, A. L.; Moore, T. A. *J. Am. Chem. Soc.* **2008**, *130*, 2015.
(19) Hambourger, M.; Liddell, P. A.; Gust, D.; Moore, A. L.; Moore, T. A. *Photochem. Photobiol. Sci.* **2007**, *6*, 431.
(20) Caramori, S.; Cristino, V.; Argazzi, R.; Meda, L.; Bignozzi, C. A. *Inorg. Chem.* **2010**, *49*, 3320.
(21) Trammell, S. A.; Moss, J. A.; Yang, J. C.; Nakhle, B. M.; Slate, C. A.; Odobel, F.; Sykora, M.; Erickson, B. W.; Meyer, T. J. *Inorg. Chem.* **1999**, *38*, 3665.
(22) Lee, S.-H. A.; Abrams, N. M.; Hoertz, P. G.; Barber, G. D.; Halaoui, L. I.; Mallouk, T. E. *J. Phys. Chem. B* **2008**, *112*, 14415.
(23) Gallagher, L. A.; Serron, S. A.; Wen, X.; Hornstein, B. J.; Dattelbaum, D. M.; Schoonover, J. R.; Meyer, T. J. *Inorg. Chem.* **2005**, *44*, 2089.
(24) Jurss, J. W.; Concepcion, J. C.; Norris, M. R.; Templeton, J. L.; Meyer, T. J. *Inorg. Chem.* **2010**, *49*, 3980.
(25) Brennaman, M. K.; Patrocinio, A. O. T.; Song, W.; Jurss, J. W.; Concepcion, J. J.; Hoertz, P. G.; Traub, M. C.; Murakami Iha, N. Y.; Meyer, T. J. *ChemSusChem* **2011**, *4*, 216
(26) Ardo, S.; Meyer, G. J. *Chem. Soc. Rev.* **2009**, *38*, 115.
(27) Hasselmann, G. M.; Meyer, G. J. *J. Phys. Chem. B* **1999**, *103*, 7671.
(28) Kelly, C. A.; Farzad, F.; Thompson, D. W.; Stipkala, J. M.; Meyer, G. J. *Langmuir* **1999**, *15*, 7047.
(29) Kuciauskas, D.; Freund, M. S.; Gray, H. B.; Winkler, J. R.; Lewis, N. S. *J. Phys. Chem. B* **2000**, *105*, 392.
(30) Nelson, J.; Chandler, R. E. *Coord. Chem. Rev.* **2004**, *248*, 1181.
(31) Nelson, J.; Haque, S. A.; Klug, D. R.; Durrant, J. R. *Phys. Rev. B* **2001**, *63*, 205321.
(32) Sun, H.; Hoffman, M. Z. *J. Phys. Chem.* **1994**, *98*, 11719.
(33) Kalyanasundaram, K.; Kiwi, J.; Grätzel, M. *Helv. Chim. Acta* **1978**, *61*, 2720.
(34) Montalti, M.; Wadhwa, S.; Kim, W. Y.; Kipp, R. A.; Schmehl, R. H. *Inorg. Chem.* **1999**, *39*, 76.
(35) Connor, P. A.; Dobson, K. D.; McQuillan, A. J. *Langmuir* **1999**, *15*, 2402.
(36) Dobson, K. D.; Connor, P. A.; McQuillan, A. J. *Langmuir* **1997**, *13*, 2614.
(37) Peri, J. B.; Tadros, T. F.; Boehm, H. P.; Lyklema, J.; Hockey, J.; Knozinger, H.; Uytterhoeven, J. B.; Parkyns, N. D.; Munuera, G.; Zecchina, A.; Szabo, Z. G.; Rochester, C. H.; Eltekov, Y. A.; Bogacheva, E. K.; Cerruti, L.; Guglielminotti, E.; Schindler, P. W.; Gamsjager, H.; Gray, T. J. *Discuss. Faraday Soc.* **1971**, *52*, 276.
(38) Watson, D. F.; Marton, A.; Stux, A. M.; Meyer, G. J. *J. Phys. Chem. B* **2004**, *108*, 11680.
(39) Lees, A. C.; Evrard, B.; Keyes, T. E.; Vos, J. G.; Kleverlaan, C. J.; Alebbi, M.; Bignozzi, C. A. *Eur. J. Inorg. Chem.* **1999**, *1999*, 2309.
(40) Haque, S. A.; Tachibana, Y.; Klug, D. R.; Durrant, J. R. *J. Phys. Chem. B* **1998**, *102*, 1745.
(41) Haque, S. A.; Tachibana, Y.; Willis, R. L.; Moser, J. E.; Gratzel, M.; Klug, D. R.; Durrant, J. R. *J. Phys. Chem. B* **1999**, *104*, 538.
(42) O'Regan, B. C.; Durrant, J. R. *Acc. Chem. Res.* **2009**, *42*, 1799.
(43) O'Regan, B.; Moser, J.; Anderson, M.; Graetzel, M. *J. Phys. Chem.* **1990**, *94*, 8720.
(44) Lyon, L. A.; Hupp, J. T. *J. Phys. Chem. B* **1999**, *103*, 4623.
(45) Wang, H.; Nicholson, P. G.; Peter, L.; Zakeeruddin, S. M.; Grätzel, M. *J. Phys. Chem. C* **2010**, *114*, 14300.
(46) Yan, S. G.; Hupp, J. T. *J. Phys. Chem. B* **1997**, *101*, 1493.
(47) Hagfeldt, A.; Grätzel, M. *Chem. Rev.* **1995**, *95*, 49.
(48) Rothenberger, G.; Fitzmaurice, D.; Graetzel, M. *J. Phys. Chem.* **1992**, *96*, 5983.
(49) Redmond, G.; Fitzmaurice, D. *J. Phys. Chem.* **1993**, *97*, 1426.
(50) Enright, B.; Redmond, G.; Fitzmaurice, D. *J. Phys. Chem.* **1994**, *98*, 6195.
(51) Moss, J. A.; Yang, J. C.; Stipkala, J. M.; Wen, X.; Bignozzi, C. A.; Meyer, G. J.; Meyer, T. J. *Inorg. Chem.* **2004**, *43*, 1784.
(52) Anderson, A. Y.; Barnes, P. R. F.; Durrant, J. R.; O'Regan, B. C. *J. Phys. Chem. C* **2010**, *114*, 1953.
(53) Cao, F.; Oskam, G.; Meyer, G. J.; Searson, P. C. *J. Phys. Chem.* **1996**, *100*, 17021.
(54) Schwarzburg, K.; Willig, F. *Appl. Phys. Lett.* **1991**, *58*, 2520.
(55) Frank, A. J.; Kopidakis, N.; Lagemaat, J. v. d. *Coord. Chem. Rev.* **2004**, *248*, 1165.
(56) Bergeron, B. V.; Kelly, C. A.; Meyer, G. J. *Langmuir* **2003**, *19*, 8389.
(57) Robel, I.; Subramanian, V.; Kuno, M.; Kamat, P. V. *J. Am. Chem. Soc.* **2006**, *128*, 2385.
(58) Grätzel, M. *Inorg. Chem.* **2005**, *44*, 6841.
(59) Wang, P.; Wenger, B.; Humphry-Baker, R.; Moser, J.-E.; Teuscher, J.; Kantlehner, W.; Mezger, J.; Stoyanov, E. V.; Zakeeruddin, S. M.; Grätzel, M. *J. Am. Chem. Soc.* **2005**, *127*, 6850.
(60) Durrant, J. R.; Haque, S. A.; Palomares, E. *Coord. Chem. Rev.* **2004**, *248*, 1247.
(61) Fujishima, A.; Honda, K. *Nature* **1972**, *238*, 37.

JACS
JOURNAL OF THE AMERICAN CHEMICAL SOCIETY

COMMUNICATION

pubs.acs.org/JACS

Diffusion-Controlled Luminescence Quenching in Metal−Organic Frameworks

Cheng Wang and Wenbin Lin*

Department of Chemistry, CB#3290, University of North Carolina, Chapel Hill, North Carolina 27599, United States

Supporting Information

ABSTRACT: Diffusion-controlled luminescence quenching of a phosphorescent metal−organic framework built from the $Ru(bpy)_3^{2+}$-derived bridging ligand (MOF-**1**) was studied using a series of amines of different sizes as quenchers. The dynamics of amine diffusion into solvent-filled MOF-**1** channels was probed by modeling time-dependent luminescence quenching data, which provide quantitative diffusion coefficients for the amine quenchers. Triethylamine, tripropylamine, and tributylamine were found to follow Fickian diffusion with a diffusivity of $(1.1 \pm 0.2) \times 10^{-13}$, $(4.8 \pm 1.2) \times 10^{-14}$, and $(4.0 \pm 0.4) \times 10^{-14}$ m^2/s, respectively. Diisopropylethylamine (DIPEA), on the other hand, was found to be too large to enter the MOF channels. Despite its size, 4-MeOPhNPh$_2$ can enter the MOF channels via a slow, complicated framework/guest intercalation process to result in extensive framework distortion as revealed by powder X-ray diffraction. This work represents the first quantitative study of the dynamics of molecular diffusion into solvent-filled MOF channels. Such quantitative information on molecular diffusion in MOFs is of fundamental importance to many of their potential applications (e.g., heterogeneous catalysis).

Metal−organic frameworks (MOFs), constructed from a variety of molecular linkers and metal or metal cluster connecting points, have emerged as a new class of molecularly tunable porous solids.[1−5] While the application of MOFs in gas storage and separation has been extensively explored in the past decade,[6−8] other important areas such as liquid-phase separation,[9,10] drug delivery,[11,12] chemical sensing,[13−16] biomedical imaging,[17,18] and particularly selective catalysis of various organic transformations[19−23] have started to attract interest recently. In many of these applications, mass transport properties of MOFs play a dominant role on their performances. Diffusion coefficient (or diffusivity) of MOFs, a key parameter characterizing the transport process, is thus an important physical quantity to be determined.

Guest molecule diffusivity in MOFs was first computationally studied using molecular dynamics (MD) simulations. Sarkisov et al. first reported theoretical predictions of self-diffusion coefficient D_s of several alkanes in MOF-**5**.[24] Sholl, Johnson, Schmid, and others also examined self-diffusion coefficient D_s and transport diffusion coefficient D_t of simple alkanes, hydrogen, carbon dioxide, benzene, and other small molecules in several MOFs including the IRMOF series and HKUST-**1**.[25−29]

In contrast to a wealth of literature on simulation efforts, there are only a few published experimental studies of measuring diffusivity in MOFs. Stallmach et al. first reported self-diffusivity of hydrocarbons in MOF-**5**,[30] and more recently in HKUST-**1**,[31] using the pulsed-field gradient NMR technique. Jobic and Maurin used quasi-elastic neutron scattering method to study self-diffusion of H_2, CO_2, and alkanes in MIL-47(V) and MIL-53(Cr).[32−35] In another direction, Kärger and co-workers used interference microscopy[36] and infrared microscopy[37] to study respectively transport diffusion of methanol into vacuum-activated manganese formate and alkanes into vacuum-activated HKUST-**1**. Quartz crystal microbalance measurement of thin films was also employed by Zybaylo et al. to estimate the diffusivity of pyridine in vacuum-activated HKUST-**1**.[38]

These measurements provide invaluable information for the applications of MOFs in gas-phase adsorption and separation. However, many of interesting applications of MOFs, such as heterogeneous catalysis, involve liquid suspensions of MOFs. In these cases, diffusion occurs when MOF channels are already filled with solvent molecules. The realistic physical picture involves continuous exchange of diffusant molecules (e.g., substrate or product molecules in MOF catalysis) with solvent molecules during their transport through MOF channels, instead of self-diffusion or transport diffusion into vacuum-activated MOFs. This kind of diffusion process is expected to be much slower than self-diffusion or transport diffusion. There were two studies on molecular diffusion into solvent-filled MOF channels,[39,40] but quantitative diffusivities could not be determined in these experiments.

In our exploration of photoactive MOFs, we encountered an interesting diffusion-controlled quenching phenomenon, in which amine quenchers in solution diffuse into MOF channels and gradually quench the MOF emission from the $Ru(bpy)_3^{2+}$-derived bridging ligand via a redox quenching mechanism.[41] We proposed that such time-dependent luminescence quenching behaviors can be utilized to model the diffusion processes of different quenchers in MOFs in solution. In a related study, diffusion coefficients of fluorescein in lysozyme crystals were obtained by modeling the fluorescence intensities determined by confocal laser scanning microscopy.[42]

The phosphorescent MOF (**1**) used in this study contains a $Ru(bpy)_3^{2+}$ derivative H_2**L**, which was synthesized by directly reacting *cis*-$[Ru(bpy)_2Cl_2]$ with 2,2′-bipyridine-5,5′-dicarboxylate

Received: December 12, 2010
Published: March 08, 2011

Scheme 1. Synthesis of Phosphorescent MOF-1 and Chemical Structures of Amine Quenchers of Varying Sizes

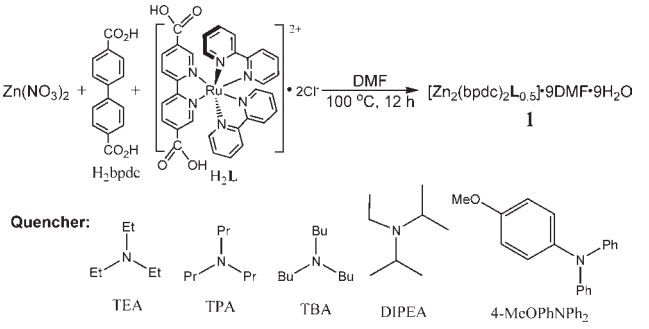

acid.[43] H_2**L** was mixed with 4,4′-biphenyldicarboxylic acid (H_2BPDC) and then reacted with $Zn(NO_3)_2 \cdot 6H_2O$ in DMF at 100 °C for 12 h to obtain yellow-red crystals with thin-plate or feather-like morphologies (Scheme 1).

1 crystallizes in the orthorhombic $C222_1$ space group, as revealed by a single-crystal X-ray diffraction study. The three-dimensional (3D) framework of **1** is built from linking $[Zn_2(\mu_2\text{-}CO_2)_3]$ SBUs with ditopic BPDC and **L** bridging ligands (Figure 1a). The asymmetric unit of **1** contains 5/2 of the dicarboxylate ligands (2 BPDC and 0.5 **L** ligands) and one Zn_2 SBU (Figure 1b). The **L** and BPDC ligands are found to randomly occupy two of the three independent ligand positions (see Supporting Information [SI] for detailed treatment of occupancy disorder), with the third ligand position exclusively occupied by the BPDC ligand. Such an occupancy disorder precludes precise determination of the **L**/BPDC ratio by X-ray crystallography. Instead, the Ru complex content **L**/(BPDC + **L**) in **1** was determined by quantitative UV−vis spectroscopy and ICP-MS to be 20%, leading to a framework formula of $Zn_2\mathbf{L}_{0.5}(BPDC)_2$ for **1**.

Three bidentate carboxylate groups bridge the two Zn atoms in the equatorial positions of the Zn_2 SBU, and the tetrahedral coordination environment of each Zn center is completed by a monodentate carboxylate group in the axial positions of the Zn_2 SBU. The Zn_2 SBUs are thus connected to each other by five dicarboxylate ligands to form a 3D framework of five-connected **bnn** topology (Figure 1c) that exhibits enormous void space (Figures S4.1 and S4.2 [SI]) and readily accommodates a second framework via interpenetration, leading to a two-fold interpenetrating structure for **1**. Even with two-fold interpenetration, **1** exhibits large open channels that are filled with solvent molecules. A combination of TGA and ^{1}H NMR analysis affords the complete formula of $[Zn_2\mathbf{L}_{0.5}(BPDC)_2] \cdot 9DMF \cdot 9H_2O$ for **1**. As a result of disordered nature of the **L** ligands in the frameworks, the open channel sizes along the [001] direction vary from 0.4 nm × 0.7 nm to 0.9 nm ×1.2 nm (Figure 1a).

Luminescence quenching experiments were performed on plate-like single crystals of **1** affixed to the bottom of a quartz fluorescent cuvette, with faces perpendicular to the cuvette bottom and immersed in cyclohexane (Scheme 2). The original DMF/H_2O solvent molecules inside the channels of **1** were first exchanged with CH_2Cl_2 and then with cyclohexane. The O_2 molecules inside the channels were removed by keeping the crystal in degassed cyclohexane overnight to prevent the luminescence quenching by O_2 via an energy-transfer pathway. The thicknesses of plate-like crystals of **1** were measured using a

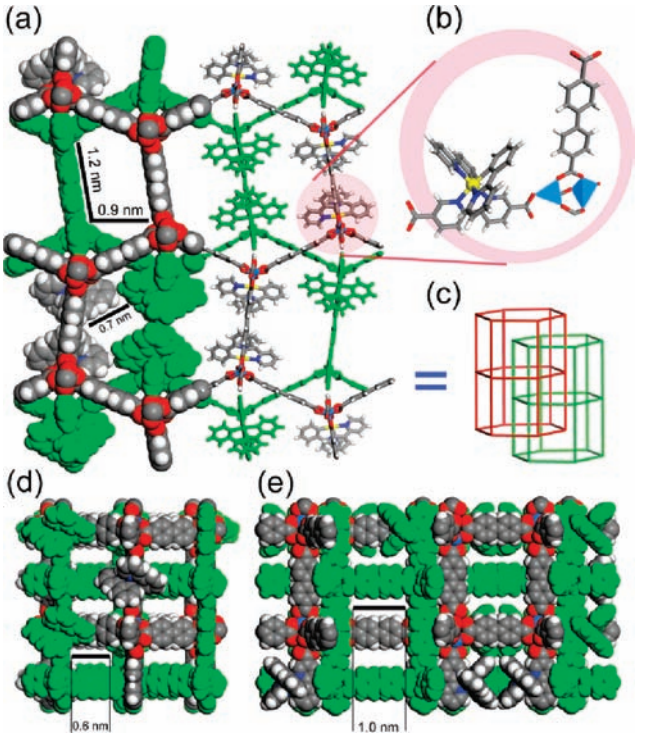

Figure 1. Structure model of MOF-**1**. (a) Space-filling and stick model viewed along the [001] direction, showing different channel sizes due to different local distributions of **L** ligands. (b) Building blocks of **1**. (c) Schematic showing two-fold interpenetrating frameworks of the **bnn** topology. (d) Space-filling model viewed along the [100] direction. (e) Space-filling model viewed along the [010] direction.

Scheme 2. Schematic of the Experimental Setup Used for Luminescence Quenching Measurements

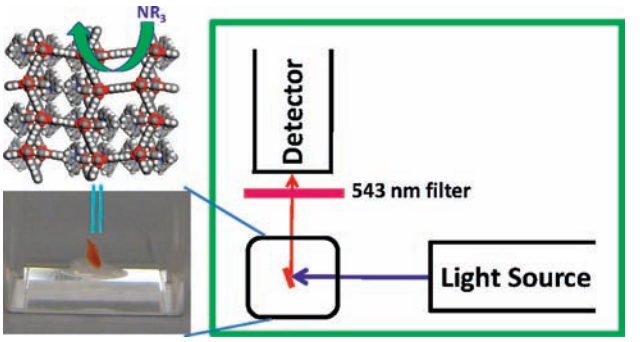

microscope with a built-in ruler. In the quenching experiment, a MOF-**1** crystal was excited at a wavelength of 452 nm, and the emission intensity at 627 nm was recorded at different time points after the addition of a predetermined amount of amine quenchers. The amines or solutions of amines were fully degassed before use. Structures of the amines are shown in Scheme 1. Excitation light was blocked from impinging on the crystal during the intervals between different emission measurements to avoid photodecomposition of the amine and other irreversible photochemical processes. A typical emission measurement took about 2 to 3 s, during which time the crystal and quenchers were exposed to light. The average value of the emission signals was recorded, and the experimental error for

dx.doi.org/10.1021/ja111197d |J. Am. Chem. Soc. 2011, 133, 4232–4235

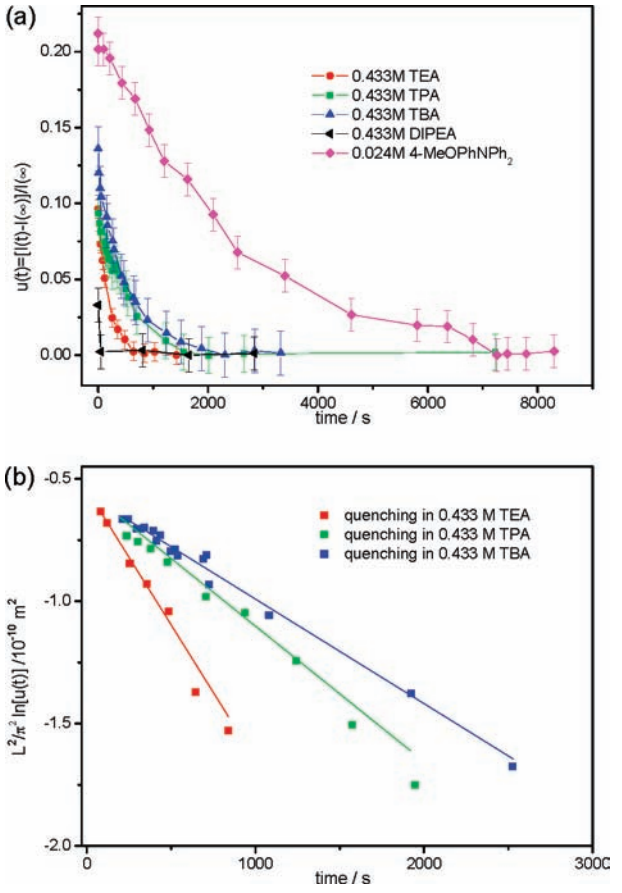

Figure 2. (a) Plots of $u(t) = [I(t) - I(\infty)]/I(\infty)$ vs t for different amine quenchers: TEA (red), TPA (green), TBA (blue), DIPEA (black), and 4-MeOPhNPh$_2$ (purple) (see SI for more detailed plots). (b) Linear fitting of $(L^2/\pi^2)\ \ln[u(t)]$ vs t of TEA (red), TPA (green), and TBA (blue). Only the data points of $t > 100$ s for TEA and $t > 200$ s for TPA and TBA were used in these fits (see SI for more detailed analyses).

each time point was estimated from the signal fluctuations within the 2 to 3 s. Spectra of the crystals were taken before and after the quenching studies to ensure that no substantial spectra change had occurred (Figure S6.1 [SI]).

The time-dependent intensity $I(t)$ was normalized against the equilibrium intensity after a long time $I(\infty)$. A plot of $u(t) = [I(t) - I(\infty)]/I(\infty)$ vs time is shown in Figure 2a. Exponential decay of the emission intensities over time to 80−85% of their initial values was observed in solutions of 0.433 M triethylamine (TEA), tripropylamine (TPA), tributylamine (TBA), and 0.024 M 4-methoxylphenyldiphenylamine (4-MeOPhNPh$_2$) as a result of diffusion-controlled luminescence quenching of **1** by these amines. The amount of time required for the emission to reach equilibrium after adding TEA, TPA, TBA, and 4-MeOPhNPh$_2$ is approximately 10, 30, 30, and 120 min, respectively. This order of increase in time required to reach equilibrium correlates well with the sizes of these amines.

For diisopropylethylamine (DIPEA) quenching, however, the intensity dropped instantaneously to 96% of its original value and remained unchanged after that. This behavior is likely a result of surface quenching only, suggesting that DIPEA cannot enter the MOF channels. To confirm this, we investigated the reverse process of amine diffusing out of the MOF channels. Crystals fully soaked in amine solutions were put back into freshly degassed cyclohexane under N_2 protection, and the changes in emission intensities were monitored. An increase of signal over time was observed for TPA- and 4-MeOPhNPh$_2$-treated MOFs, indicating the release of absorbed quenchers. In contrast, for the MOFs soaked in DIPEA, no signal increase was detected. This result supports the notion that no DIPEA can enter in MOF channels, presumably owing to its large size (Figure S7.1 [SI]). Further evidence comes from GC analysis of the absorbed amine in the MOF channels. Amine-treated **1** released substantial amounts of TPA, TBA, and 4-MeOPhNPh$_2$, but no DIPEA (SI). These results unambiguously prove the accessibility of the MOF channels to all the amines except DIPEA.

Geometry-optimized structure of 4-MeOPhNPh$_2$ is much larger than that of DIPEA (SI), so their different uptake behaviors by **1** cannot be explained simply based on their sizes. Instead, we believe that different uptake behaviors of the two amines stem from their disparate affinities toward the MOF channels. 4-MeOPhNPh$_2$, as an aromatic amine, can strongly interact with the MOF channel wall via $\pi-\pi$ interactions, whereas aliphatic chains of DIPEA do not provide such a driving force for inclusion. PXRD patterns of amine-treated crystals of **1** were taken to provide insights into these different uptake behaviors. While the PXRD patterns of all the aliphatic amine-treated MOFs closely resemble that of the as-synthesized **1**, the pattern of 4-MeOPhNPh$_2$−treated MOF crystals lose all of the diffraction peaks due to **1** (Figure S9.1 [SI]). The severe framework structure distortion of 4-MeOPhNPh$_2$-treated **1** suggests that 4-MeOPhNPh$_2$ enters the MOF by intercalating into the framework via $\pi-\pi$ interactions instead of simple Fickian diffusion.

We quantitatively analyze the diffusion of TEA, TPA, and TBA in the framework of Fickian diffusion. In other words, we assume a constant diffusivity, D, independent of local concentration of amine quenchers. By taking advantage of thin-plate morphology of the MOF crystals, we further simplify the diffusion process into a 1D diffusion described by Fick's second law (Eq 1) with the boundary conditions and initial conditions expressed in Eq 2 and Eq 3, respectively:

$$\frac{\partial c(x,t)}{\partial t} = D\frac{\partial^2 c(x,t)}{\partial x^2} \qquad \text{(Eq 1)}$$

$$c(0,t) = c(L,t) = c_0 \qquad \text{(Eq 2)}$$

$$c(x,0) = 0 (0 < x < L) \qquad \text{(Eq 3)}$$

For the emission quenching, we assume a rapid, reversible quenching behavior that can be described by the Stern−Volmer equation. In addition, activity correction for amine concentration inside MOF channels, the sample dependent crystal geometry and position factor, and the contribution from surface emission have also been considered. Using this model, the time-dependent normalized emission intensity was derived (SI), and can be expressed with Eq 4:

$$u(t) \approx A\exp\left(-\left[\pi^2 Dt\right]/L^2\right) \qquad \text{(Eq 4)}$$

where A is independent of time t and is expressed by $A = (1/(1 + \delta))\ ([4\alpha\beta c_0]/[1 + \alpha\beta c_0])\ ([\in L]/[\cos\theta])/([(\in L)/(\cos\theta)]^2 + \pi^2)$ (α, β, $\in$, θ, and δ are introduced to account for Stern−Volmer quenching, activity correction, crystal absorption, crystal positioning, and surface emission, respectively, see SI); L is thickness of the crystal, and D is the Fickian diffusivity.

dx.doi.org/10.1021/ja111197d |J. Am. Chem. Soc. 2011, 133, 4232–4235

Plots of $(L^2/\pi^2)\ln[u(t)]$ vs t gave straight lines (Figure 2b), indicating the validity of the Fickian diffusion model as described by Eq 4. Diffusivities of TEA, TPA, and TBA in MOF-**1** could be obtained from the slopes of these linear fits, and were determined to be $(1.1 \pm 0.2) \times 10^{-13}$, $(4.8 \pm 1.2) \times 10^{-14}$, and $(4.0 \pm 0.4) \times 10^{-14}$ m^2/s, respectively. These values are 1−2 orders of magnitude smaller than the transport diffusivity reported for methanol into vacuum-activated porous manganese formate crystals,[36] a system that has a similar diffusant/channel size ratio as our present case. This discrepancy is expected since the two diffusion processes are of very different natures. The diffusivity derived in our present study is much more relevant to many applications that involve liquid suspensions of MOFs.

In summary, we have examined diffusion-controlled luminescence quenching of a $Ru(bpy)_3^{2+}$-incorporated MOF by a series of amines of different sizes. TEA, TPA, and TBA can diffuse through the MOF channels according to the time-dependent quenching data, whereas DIPEA is too large to enter the MOF channels. Despite its large size, 4-MeOPhNPh$_2$ can enter the MOF channels via a slow, complicated framework/guest intercalation process to result in extensive framework distortion as revealed by PXRD. The time-dependent quenching curves of TEA, TPA, and TBA were fitted quantitatively with a 1D Fickian diffusion model to afford diffusivities on the order of 10^{-14}−10^{-13} m^2/s. These diffusivities are 1−2 orders of magnitude smaller than that of a transport diffusion system of a similar diffusant/channel size ratio. The dynamics of molecular diffusion into solvent-filled MOF channels reported herein is of fundamental importance to many MOF applications in solution.

■ ASSOCIATED CONTENT

Supporting Information. Experimental procedures, characterization data, detailed derivations of the diffusion equations, and complete ref 11. This material is available free of charge via the Internet at http://pubs.acs.org.

■ AUTHOR INFORMATION

Corresponding Author
wlin@unc.edu

■ ACKNOWLEDGMENT

We acknowledge financial support from NSF. We made use of the UNC EFRC instrumentation facility which is funded jointly by the U.S. Department of Energy Office of Science (BES, DE-SC0001011) and Office of Energy Efficiency & Renewable Energy (DE-EE0003188).

■ REFERENCES

(1) Bradshaw, D.; Warren, J. E.; Rosseinsky, M. J. *Science* **2007**, *315*, 977.
(2) Evans, O. R.; Lin, W. *Acc. Chem. Res.* **2002**, *35*, 511.
(3) Ferey, G.; Mellot-Draznieks, C.; Serre, C.; Millange, F. *Acc. Chem. Res.* **2005**, *38*, 217.
(4) Kitagawa, S.; Kitaura, R.; Noro, S. *Angew. Chem., Int. Ed.* **2004**, *43*, 2334.
(5) Ockwig, N. W.; Delgado-Friedrichs, O.; O'Keeffe, M.; Yaghi, O. M. *Acc. Chem. Res.* **2005**, *38*, 176.
(6) Li, J. R.; Kuppler, R. J.; Zhou, H. C. *Chem. Soc. Rev.* **2009**, *38*, 1477.
(7) Pan, L.; Olson, D. H.; Ciemnolonski, L. R.; Heddy, R.; Li, J. *Angew. Chem., Int. Ed.* **2006**, *45*, 616.
(8) Ma, L.; Mihalcik, D. J.; Lin, W. *J. Am. Chem. Soc.* **2009**, *131*, 4610.
(9) Alaerts, L.; Maes, M.; Giebeler, L.; Jacobs, P. A.; Martens, J. A.; Denayer, J. F. M.; Kirschhock, C. E. A.; De Vos, D. E. *J. Am. Chem. Soc.* **2008**, *130*, 14170.
(10) Maes, M.; Alaerts, L.; Vermoortele, F.; Ameloot, R.; Couck, S.; Finsy, V.; Denayer, J. F. M.; De Vos, D. E. *J. Am. Chem. Soc.* **2010**, *132*, 2284.
(11) Horcajada, P.; et al. *Nat. Mater.* **2010**, *9*, 172.
(12) Rieter, W. J.; Pott, K. M.; Taylor, K. M.; Lin, W. *J. Am. Chem. Soc.* **2008**, *130*, 11584.
(13) Allendorf, M. D.; Houk, R. J.; Andruszkiewicz, L.; Talin, A. A.; Pikarsky, J.; Choudhury, A.; Gall, K. A.; Hesketh, P. J. *J. Am. Chem. Soc.* **2008**, *130*, 14404.
(14) Chen, B.; Wang, L.; Xiao, Y.; Fronczek, F. R.; Xue, M.; Cui, Y.; Qian, G. *Angew. Chem., Int. Ed.* **2009**, *48*, 500.
(15) Lan, A.; Li, K.; Wu, H.; Olson, D. H.; Emge, T. J.; Ki, W.; Hong, M.; Li, J. *Angew. Chem., Int. Ed.* **2009**, *48*, 2334.
(16) Xie, Z.; Ma, L.; deKrafft, K. E.; Jin, A.; Lin, W. *J. Am. Chem. Soc.* **2010**, *132*, 922.
(17) deKrafft, K. E.; Xie, Z.; Cao, G.; Tran, S.; Ma, L.; Zhou, O. Z.; Lin, W. *Angew. Chem., Int. Ed.* **2009**, *48*, 9901.
(18) Lin, W.; Rieter, W. J.; Taylor, K. M. *Angew. Chem., Int. Ed.* **2009**, *48*, 650.
(19) Lee, J.; Farha, O. K.; Roberts, J.; Scheidt, K. A.; Nguyen, S. T.; Hupp, J. T. *Chem. Soc. Rev.* **2009**, *38*, 1450.
(20) Lin, W. B. *MRS Bull.* **2007**, *32*, 544.
(21) Ma, L.; Abney, C.; Lin, W. *Chem. Soc. Rev.* **2009**, *38*, 1248.
(22) Ma, L.; Falkowski, J. M.; Abney, C.; Lin, W. *Nat. Chem.* **2010**, *2*, 838.
(23) Song, F.; Wang, C.; Falkowski, J. M.; Ma, L.; Lin, W. *J. Am. Chem. Soc.* **2010**, *132*, 15390.
(24) Sarkisov, L.; D., T.; Snurr, Q. R. *Mol. Phys.* **2004**, *102*, 211.
(25) Amirjalayer, S.; Schmid, R. *Microporous Mesoporous Mater.* **2009**, *125*, 90.
(26) Amirjalayer, S.; Tafipolsky, M.; Schmid, R. *Angew. Chem., Int. Ed.* **2007**, *46*, 463.
(27) Keskin, S.; Sholl, D. S. *Langmuir* **2009**, *25*, 11786.
(28) Seehamart, K.; Nanok, T.; Karger, J.; Chmelik, C.; Krishna, R.; Fritzsche, S. *Microporous Mesoporous Mater.* **2010**, *130*, 92.
(29) Skoulidas, A. I.; Sholl, D. S. *J. Phys. Chem. B* **2005**, *109*, 15760.
(30) Stallmach, F.; Groger, S.; Kunzel, V.; Karger, J.; Yaghi, O. M.; Hesse, M.; Muller, U. *Angew. Chem., Int. Ed.* **2006**, *45*, 2123.
(31) Wehring, M.; Gascon, J.; Dubbeldam, D.; Kapteijn, F.; Snurr, R. Q.; Stallmach, F. *J. Phys. Chem. C* **2010**, *114*, 10527.
(32) Jobic, H.; Rosenbach, N.; Ghoufi, A.; Kolokolov, D. I.; Yot, P. G.; Devic, T.; Serre, C.; Ferey, G.; Maurin, G. *Chem.—Eur. J.* **2010**, *16*, 10337.
(33) Rosenbach, N.; Jobic, H.; Ghoufi, A.; Salles, F.; Maurin, G.; Bourrelly, S.; Llewellyn, P. L.; Devic, T.; Serre, C.; Ferey, G. *Angew. Chem., Int. Ed.* **2008**, *47*, 6611.
(34) Salles, F.; Jobic, H.; Ghoufi, A.; Llewellyn, P. L.; Serre, C.; Bourrelly, S.; Ferey, G.; Maurin, G. *Angew. Chem., Int. Ed.* **2009**, *48*, 8335.
(35) Salles, F.; Jobic, H.; Maurin, G.; Koza, M. M.; Llewellyn, P. L.; Devic, T.; Serre, C.; Ferey, G. *Phys. Rev. Lett.* **2008**, 100.
(36) Kortunov, P. V.; Heinke, L.; Arnold, M.; Nedellec, Y.; Jones, D. J.; Caro, J.; Karger, J. *J. Am. Chem. Soc.* **2007**, *129*, 8041.
(37) Chmelik, C.; Karger, J.; Wiebcke, M.; Caro, J.; van Baten, J. M.; Krishna, R. *Microporous Mesoporous Mater.* **2009**, *117*, 22.
(38) Zybaylo, O.; Shekhah, O.; Wang, H.; Tafipolsky, M.; Schmid, R.; Johannsmann, D.; Woll, C. *Phys. Chem. Chem. Phys.* **2010**, *12*, 8092.
(39) Choi, H. J.; Suh, M. P. *J. Am. Chem. Soc.* **2004**, *126*, 15844.
(40) Han, S. B.; Wei, Y. H.; Valente, C.; Lagzi, I.; Gassensmith, J. J.; Coskun, A.; Stoddart, J. F.; Grzybowski, B. A. *J. Am. Chem. Soc.* **2010**, *132*, 16358.
(41) Kalyanasundaram, K. *Coord. Chem. Rev.* **1982**, *46*, 159.
(42) Cvetkovic, A.; Picioreanu, C.; Straathof, A. J. J.; Krishna, R.; van der Wielent, L. A. M. *J. Am. Chem. Soc.* **2005**, *127*, 875.
(43) Xie, P. H.; Hou, Y. J.; Zhang, B. W.; Cao, Y.; Wu, F.; Tian, W. J.; Shen, J. C. *J. Chem. Soc., Dalton Trans.* **1999**, 4217.

THE JOURNAL OF PHYSICAL CHEMISTRY A

ARTICLE

pubs.acs.org/JPCA

Structural and pH Dependence of Excited State PCET Reactions Involving Reductive Quenching of the MLCT Excited State of $[Ru^{II}(bpy)_2(bpz)]^{2+}$ by Hydroquinones

Natalia V. Lebedeva,[†] Robert D. Schmidt,[†] Javier J. Concepcion,[†] M. Kyle Brennaman,[†] Ian N. Stanton,[‡] Michael J. Therien,[‡] Thomas J. Meyer,[†] and Malcolm D. E. Forbes*[,†]

[†]Department of Chemistry Caudill Laboratories University of North Carolina, Chapel Hill, North Carolina 27599-3290, United States

[‡]Department of Chemistry French Family Science Center Duke University, Durham, North Carolina 27708, United States

Supporting Information

ABSTRACT: The proton-coupled electron transfer (PCET) reaction between the bpz-based photoexcited ^{3}MLCT state of $[Ru^{II}(bpy)_2(bpz)]^{2+}$ (bpy = 2,2′-bipyridine, bpz = 2,2′-bipyrazine) and a series of substituted hydroquinones (H_2Q) has been studied by transient absorption (TA) and time-resolved electron paramagnetic resonance (TREPR) spectroscopy at X-band. When the reaction is carried out in a CH_3CN/H_2O mixed solvent system with unsubstituted hydroquinone, the neutral semiquinone radical (**4a**) and its conjugate base, the semiquinone radical anion (**4b**), are both observed. Variation of the acid strength in the solvent mixture allows the acid/base dependence of the PCET reaction to be investigated. In solutions with very low acid concentrations, TREPR spectra exclusively derived from radical anion **4b** are observed, while at very high acid concentrations, the spectrum is assigned to the protonated structure **4a**. At intermediate acid concentrations, either a superposition of spectra is observed (slow exchange between **4a** and **4b**) or substantial broadening in the TREPR spectrum is observed (fast exchange between **4a** and **4b**). Variation of substituents on the H_2Q ring substantially alter this acid/base dependence and provide a means to investigate electronic effects on both the ET and PT components of the PCET process. The TA results suggest a change in mechanism from PCET to direct ET quenching in strongly basic solutions and with electron withdrawing groups on the H_2Q ring system. Changing the ligand on the Ru complex also alters the acid/base dependence of the TREPR spectra through a series of complex equilibria between protonated and deprotonated hydroquinone radicals and anions. The relative intensities of the signals from radical **4a** versus **4b** can be rationalized quantitatively in terms of these equilibria and the relevant pK_a values. An observed equilibrium deuterium isotope effect supports the conclusion that the post−PCET $HQ^{\bullet}/Q^{\bullet-}$ equilibrium is the most important in determining the **4a**/**4b** ratio at early delay times.

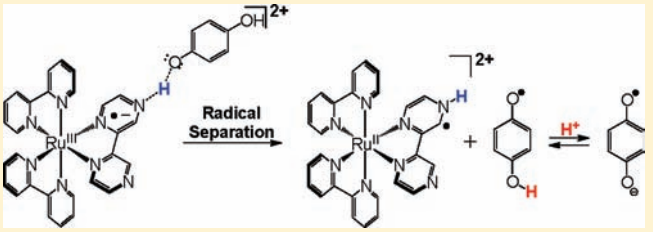

INTRODUCTION

Proton-coupled electron transfer (PCET) reactions are ubiquitous in nature.[1] They are also found in many non-natural chemical reactions involving catalysis and redox reactions such as artificial photosynthesis[2] and fuel cell technology.[3] Indeed, the construction of chemical systems that effectively mimic plant photosystem II (PSII) remains a "holy grail" for researchers in solar fuels[4] and other alternative energy resources.[5] Within the overall mechanism of action of PSII, there is a cascade of PCET reactions that eventually shuttle four electrons and four protons to the correct location for water oxidation.[6] The buildup of multiple redox equivalents at a single site is made possible by these PCET reactions, which are only successful if they avoid high−energy reactive intermediates. The mechanistic details and intermediate species involved in thermal and excited state PCET reactions are therefore a topic of high current interest.

In 2007, we reported the novel PCET reaction shown in Scheme 1, which involves the reductive quenching of **2**, the ^{3}MLCT state (formally Ru^{III}) of $[Ru^{II}(bpy)_2(bpz)]^{2+}$ (**1**, bpy = 2,2′-bipyridine, bpz = 2,2′-bipyrazine) by hydroquinone (H_2Q).[7] In this reaction, a hydrogen bond forms between the OH of the H_2Q and the peripheral nitrogen on the bpz ligand of **2**, created after photoexcitation of **1** at 355 nm. The H-bond forms exclusively with the excited state of the complex because the pK_b of the ligand nitrogen is substantially raised in the MLCT state due to a large increase in electron density in the ligand. The quenching reaction takes place on the ∼100 ns time scale by concerted proton transfer (PT) from H_2Q to the peripheral bpz nitrogen and electron transfer (ET) from the H_2Q oxygen to Ru^{III}. The resulting intermediates formed are the semiquinone radical $HQ^{\bullet}$ (**4a**) and a ligand-based free radical of the initial Ru complex (**3**) formed by the ET component of the PCET process.

Received: January 13, 2011
Revised: February 10, 2011
Published: March 24, 2011

Scheme 1

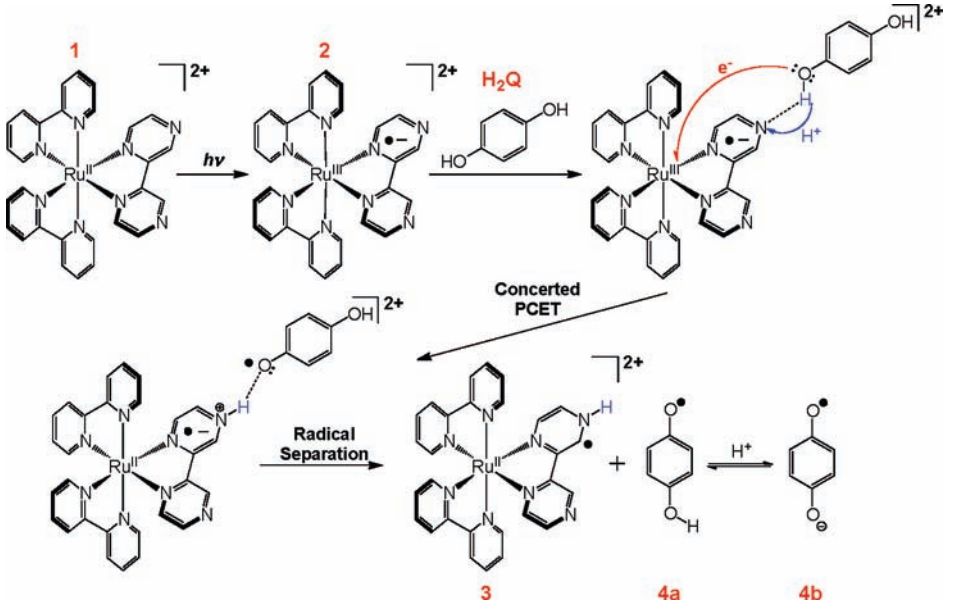

In dry acetonitrile solvent, the $HQ^{\bullet}$ radical **4a** is the only organic radical observed, but if the reaction is run in water/acetonitrile mixtures, deprotonation of **4a** to semiquinone anion radical **4b** is facile and both radicals are produced by the PCET reaction.

Ligand-based radical **3** is easily detected in solution via nanosecond transient absorption (TA) spectroscopy. It has characteristic absorption features with large extinction coefficient changes at 350, 440, and 535 nm. However, the intensity of the absorption band at ca. 440 nm is so high that direct observation of the $HQ^{\bullet}$ radical **4a** is rendered extremely difficult. Radical **4a** absorbs at 415 nm with an extinction coefficient of 4300 M^{-1} cm^{-1}.[8] To detect this radical by TA requires a large increase in the concentration of H_2Q in the solution. However, as demonstrated in our previous paper, time-resolved electron paramagnetic resonance (TREPR) spectroscopy[9] can be used to detect radical **4a** (or **4b**) without interference from the ligand-based radical **3**. This is because radical **3** is TREPR silent, at least in solution on the microsecond time scale, presumably due to rapid electron spin relaxation induced by the metal center. In fact, one can draw a resonance structure from the radical structure shown in Scheme 1 for **3** to another that places the unpaired electron on a nitrogen atom directly adjacent to Ru. Thus, the TREPR spectrum initially reported by us in 2007 for the system in Scheme 1 displayed only one radical (**4a**) in dry acetonitrile solution after irradiation of the Ru complex at 355 nm.

Electron spin relaxation rates in the radicals are important here because the TREPR experiment usually detects spin polarized radicals, i.e. the observed transitions show enhanced absorption or emission. This is due to non-Boltzmann spin state populations from various (well understood) mechanisms of chemically induced electron spin polarization (CIDEP).[10] For the reaction shown in Scheme 1, the predominant CIDEP process is from the triplet mechanism,[11] which is a net effect (from rapid and anisotropic intersystem crossing)[12] leading to emissive transitions for each line in the TREPR spectrum of **4a** (**4b**). The polarization is easily incorporated into existing simulation routines for solution phase TREPR spectra.

Because the populations in radical **3** have relaxed to Boltzmann levels, they are not detected in the TREPR experiment. However, after their creation by the PCET reaction, radical **4a** (**4b**) is no longer coupled to the metal center and does not have access to an efficient spin relaxation mechanism. Therefore, radical **4a** (**4b**) is easily observed at delay times ranging from 100 ns to 2 μs after the laser flash, that is, within the expected electron spin relaxation time of an organic free radical in liquid solution. Figure 1A shows representative spectra from the photochemistry illustrated in Scheme 1, in the CH_3CN/H_2O mixed solvent system at an excitation wavelength of 355 nm. A superposition of spectra due to radicals **4a** and **4b** is observed. Figure 1B shows a spectrum from irradiation of the same system run in CH_3CN/D_2O, where the −OH proton of the H_2Q has undergone almost complete exchange with D_2O (leading to "D_2Q"). The deuterated analog of **4a** shows a 1:2:1 triplet due to hyperfine coupling to the ortho protons. The meta and the −OD proton coupling constants are smaller than the line width and are not resolved. Also, in Figure 1B it should be noted that three of the five lines from radical anion **4b** are obscured due to overlapping transitions with radical **4a**. To facilitate interpretation of the data in Figure 1, we have provided a deconvolution of the spectral components in the Supporting Information.

The spectra in Figure 1 are easily simulated by using literature values for the protonated and deprotonated H_2Q radicals,[13] and we have added the emissive triplet mechanism spin polarization by using an in-house simulation routine for CIDEP mechanisms. In addition to the magnetic parameters used in the simulations, the CIDEP mechanism (phase and intensity) and the relative ratio of each radical signal match well with those reported recently by Jäger et al. in a TREPR study of benzoquinone photochemistry in alcohol solutions.[14] The hyperfine coupling constants and g−factors used for the simulation are listed in the caption to Figure 1. Our simulations unambiguously assign all spectral features to the two radicals (**4a** and **4b**), with no spectral contribution from radical **3**, as expected.

There are several noteworthy features of this chemistry: (1) The observed strong emissive spin polarization is of great interest, as there are very few metal-containing photochemical systems reported in the literature that exhibit strong CIDEP, by any mechanism. It is somewhat surprising that TREPR signals are observed in the first place, because spin relaxation in the rapidly formed MLCT state is expected to be quite efficient. It is possible that relaxation is indeed still occurring, but because the polarization is very large, the overpopulation is still substantially higher than the Boltzmann populations at the time of observation. (2) Most photochemical reactions that form free radicals produce radical pairs, that is, two neutral radicals are observed (for example by bond cleavage or H-atom abstraction reactions). Alternatively, a radical cation/anion pair is observed (for example by electron transfer). Our TA experiments reported in 2007 clearly indicate the formation of two radicals from this photochemistry, however, only one is observed by TREPR. This is an unusual situation, and for such TREPR-detected photochemical reactions involving a Ru complex, there is only one other system reported in the literature,[15] where alkyl radicals were observed after a direct bond cleavage reaction from Re−C or Ru−C bonds. (3) The PCET reaction in Scheme 1 represents a new method for the formation of organic free radicals that deserves further mechanistic scrutiny.

We note that radicals **4a** and **4b** are capable of exchanging their −OH protons, which is probably not rapid at this acid strength (pH meter reading of 4.9 for 1:1 v/v CH_3CN/H_2O). Variations in acid strength should alter the ratio of the two radicals and may also affect the PCET reaction mechanism itself. Additionally, the presence of electron withdrawing or electron donating groups is predicted to have an effect on the chemistry through the redox potentials for the relevant PCET and ET couples, as shown in eq 1.[7]

$$\Delta G^0 = E^{0'}(M^{II}L/M^{II}L^{\bullet -}) + E_{00}(M^{III}L^{\bullet -}) - E^{0'}(H_2Q^{\bullet +}/H_2Q) + 0.059(pK_a(H_2Q^{\bullet +}) - pK_a(M^{II}L^{\bullet}H)) \quad (1)$$

Here $E^{0'}(M^{II}L/M^{II}L^{\bullet -})$ is the potential for bpz-based reduction, $E_{00}(M^{III}L^{\bullet -})$ is the free energy content of the excited state above the ground state, $E^{0'}(H_2Q^{\bullet +}/H_2Q)$ is the reduction potential for the $H_2Q^{\bullet +}/H_2Q$ couple, and $pK_a(H_2Q^{\bullet +})$ and $pK_a(M^{II}L^{\bullet}H)$ are the pK_a values for the oxidized hydroquinone and $1e^-$ reduced complex, respectively.

Proceeding qualitatively at first, substituent effects on H_2Q are summarized in Scheme 2. The presence of an electron−donating group on the H_2Q ring system should provide stabilization of positive charge and destabilization of negative charge. In the framework of the PCET reaction, this should "push" the ET part of the reaction forward and simultaneously "pull" the PT part backward. Conversely, an electron-withdrawing group on H_2Q should "pull" the ET reaction back and "push" the PT reaction forward. These classical concepts from physical organic chemistry will be used in the present paper to present a structure−reactivity study and pH dependence of the PCET reaction in Scheme 1, studied using TREPR.

To put this on a more quantitative footing, eq 1 shows that the overall driving force for the PCET reaction is a function of several variables. Two are of particular interest in this work. The proton transfer (PT) part of the PCET reaction should vary with the pK_a of the H_2Q protons. This pK_a value will also affect the H-bonding ability of H_2Q and, hence, the stability of its complex with the

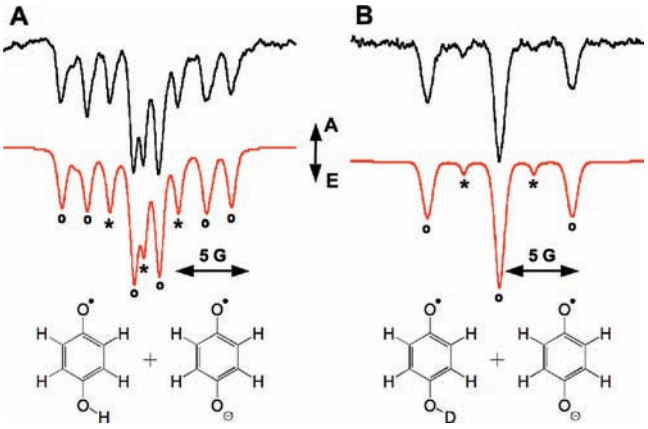

Figure 1. Experimental TREPR (black spectra) data collected 500 ns after a 355 nm laser pulse for the PCET reaction between **1** and H_2Q affording spectra of **4a** (indicated by °) and **4b** (indicated by *) in (A) 1:1 CH_3CN/H_2O and (B) 1:1 CH_3CN/D_2O solution prepared at 150 μM in **1** and 0.5 M in H_2Q. Simulation (red spectra) parameters for (A) **4a**: g = 1.99535, A(*o*-H) = 5.0 G (2H), A(-OH) = 1.7 G (1H), 66% of mixture; **4b**: g = 1.99548, A(-H) = 2.37 G (4H), 33% of mixture. (B) **4a**: g = 1.99260, A(*o*-H) = 5.1 G (2H), A(-OD) = 1.755/6.5 = 0.27 G (1D, unresolved), 91% of mixture; **4b**: g = 1.99267, A(ring H) = 2.43 G (4H), 9% of mixture. For $HQ^{\bullet}$ radicals, the *meta*-proton hyperfine couplings are unresolved in both data sets.

Scheme 2

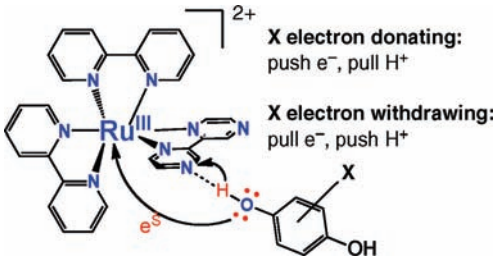

MLCT excited state. Furthermore, the reduction potential of H_2Q, altered by substituents, should have a strong affect on the ET component of the PCET reaction. Table 1 lists the relevant E^0 and pK_a values that are most relevant to the discussion below.[16] The underlying trend in these numbers tells us that the thermodynamics of the ET component in Scheme 1 are strongly affected by the efficacy of the PT component. In other words, a larger and more negative driving force in eq 1 is provided by a larger and more positive E^0 value (driving the ET component) and a smaller pK_a value of H_2Q (driving the PT component). At the same time it must be recognized that when the acid/base equilibrium of H_2Q/HQ^- is considered, the relevant pK_a value in eq 1 changes. It is within this framework that the pH dependence of our TREPR spectra, acquired after the PCET reaction in Scheme 1 is complete, will be presented and discussed.

EXPERIMENTAL SECTION

Materials. Hydroquinone and derivatives were purchased from Aldrich and recrystallized from ethyl acetate/hexanes before use. 2,2′-Bipyrazine (bpz) and $[Ru^{II}(bpy)_2(bpz)](PF_6)_2$ were prepared and purified according to literature methods.[17,18]

Table 1. pK_a and E^0 Data Relevant to Scheme 1 PCET Reactions[a]

H_2Q species	pK_a $H_2Q \rightarrow HQ^-$	pK_b $HQ^- \rightarrow Q^{2-}$	pK_s $HQ^\bullet \rightarrow Q^{\bullet-}$	E_0 (H_2Q/Q; mV)	E_0 ($HQ^-/HQ^\bullet$; mV)	E_0 ($Q^{\bullet-}/Q$; mV)
2,6-dimethylhydroquinone	10.35	12.4	4.75	+588	+350	−80
hydroquinone	9.85	11.2	4.1	+700	+482	+81
2,5-dichlorohydroquinone	7.9	10.0	2.1	+723	+623	+223
2,3,5,6-tetrachlorohydroquinone	5.6	8.2	0.0	+699	+726	+336

[a] Data taken from ref 15.

TREPR Spectroscopy. Our TREPR apparatus has been described in several recent publications.[19] Briefly, the YAG-pumped OPO laser is fired at a repetition rate of 10 Hz, while sampling the direct detection EPR signal from the microwave bridge (CW mode) using a gated boxcar signal averager. The external magnetic field is swept over 4 min with 300 ns gates, sampling the EPR signal ~5 times at each magnetic field point. Samples (freshly prepared in the appropriate solvent system with 0.5 M H_2Q and 150 μM Ru complex) were flowed through a quartz flat cell (0.4 mm path length) placed in the center of the microwave resonator using a micropump from a reservoir that was constantly purged with nitrogen gas bubbles (for 10 min prior to and during EPR experiments). All spectra have a center field of approximately 3385 G, a microwave frequency of 9.47 GHz, and a microwave power of 10 mW. Transitions appearing below the baseline in each spectrum represent emissive spin polarization, that is, the upper electron spin state of each radical is overpopulated (see above for details on the origin of the emissive polarization).

Acid/Base Strength Modifications. The acid/base strength of the solutions (initially 1:1 CH_3CN/H_2O) was modified by the addition of 2 M aqueous solutions of HCl or NaOH. The apparent change in pH was checked with an aqueous-calibrated pH meter to confirm deviation from the initial value, and provide an approximate scale of acid/base strength of the solution. The deviation from the true solution pH of the measured pH value for a 1:1 mixture of CH_3CN/H_2O obtained at about 25 °C with an aqueous electrode has been shown to be about −0.26 pH units.[20]

Transient Absorption Spectroscopy. Transient absorption (TA) spectroscopy data was collected on an Edinburgh LP920 Laser Flash Photolysis System. An Opotek Vibrant LD 355 laser system provided wavelength tunable nanosecond pulses (5 ns fwhm) for pump excitation and a pulsed 450 W xenon lamp provided the white light probe source. Spectra were collected on an Andor iStar ICCD and the transient plots were generated through Edinburgh's L900 Software. The Opotek Vibrant was operated at 1 Hz, tuned to 430 nm, and its power was maintained at 2.75 ± 0.1 mJ: (440 nm, 3 mJ for Figure 4B) using OD filters to avoid photodegradation from high power pulses. Typical settings for the spectral collection were recorded in the time domain from 10 ns to 50.01 μs, with time intervals of 5 μs, 20 transient spectra averaged per step, and a spectrograph slit width of 3 nm. Sample solutions were freshly prepared in 1:1 CH_3CN/H_2O at about 57 μM in Ru^{II} complex, 0.47 M H_2Q, and 0.1 M KPF_6 for ionic strength, then argon-purged in quartz cuvettes (1 × 1 cm) for a minimum of 25−30 min.

RESULTS AND DISCUSSION

Acid/Base Strength Dependence: TREPR Studies. Figure 2 shows the time dependence of the PCET reaction in Scheme 1 in 1:1 CH_3CN/H_2O at what we refer to as "ambient" acid strength,

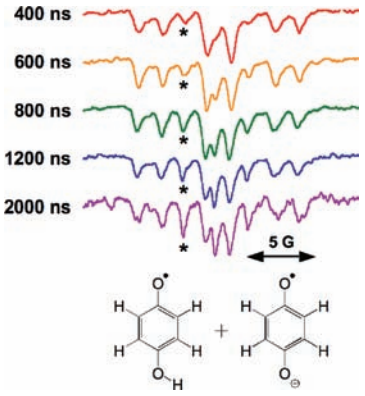

Figure 2. Evolution of the TREPR spectrum of **4a**/**4b** collected at different delay times following a 355 nm laser pulse in 1:1 CH_3CN/H_2O prepared at 150 μM in **1** and 0.5 M in H_2Q (pH meter reading = 4.9). Growth over time of spectral features corresponding to radical anion **4b** are indicated with a *.

that is, there is no added acid or base in the solution. On an aqueous calibrated pH meter, this reads 4.9 pH units for this particular solvent system, but it should be noted that for mixed solvents there should be a correction factor applied to this measurement (−0.26 for the CH_3CN/H_2O system).[20] Because the correction factor is small and acid strength affects the spectra in a systematic way, we will report only the uncorrected pH meter readings for all reaction conditions. One transition associated with radical **4b** is highlighted in Figure 2 to show the growth of this species in time; the spectra are not normalized. The later delay time spectra, which show weaker signals due to electron spin relaxation processes (with ~1 μs time constant for both radicals at room temperature in liquid solution) have been scaled up to show that the ratio of the two radicals is not the same at each delay time.

The signal for protonated radical **4a** is more intense at early delay times, while the anion radical **4b** grows over time. Because both radicals have very similar electron spin relaxation rates,[14] this difference in intensities is best explained as the gradual deprotonation of radical **4a** to give radical **4b** on this time scale. It is also important to note that, at this acid strength, the observed spectrum is always that of a superposition of the two radical species, meaning that the time scale for the deprotonation reaction is slow compared to the time scale of observation (300 ns window of integration). This is consistent with expectations for these structures in a moderate acid strength environment.

A rough estimate of the equilibrium ratio of **4b** to **4a** can be made using the acid strength ("pH" in the mixed solvent = 4.9) and the pK_a for $HQ^\bullet$ = 4.1 (labeled as pK_s in Table 1). The ratio of anion to neutral species obtained in this fashion is ~3. The data in Figure 2 show that this system is not at equilibrium at time 0 (the transitions due to the anion are clearly less intense than those from the neutral species). However, it is clear that the system is

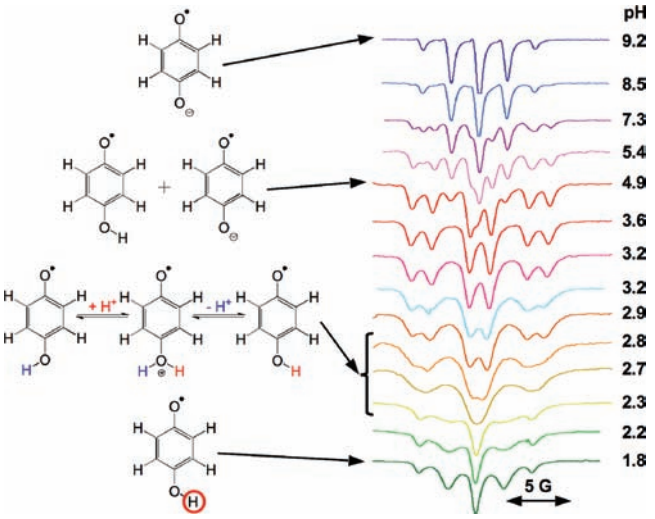

Figure 3. Variation of TREPR spectrum of **4a**/**4b** mixture collected at 500 ns after a 355 nm laser pulse with acid/base strength of a 1:1 CH_3CN/H_2O solution prepared at 150 μM in **1** and 0.5 M in H_2Q. The unadjusted "natural" solution spectrum is shown for an uncorrected pH meter reading of 4.9.

moving toward the equilibrium ratio (growth of **4b** and decay of **4a**) over the first few microseconds after the PCET event. It should be noted that this assessment based on TREPR intensities has validity only if the electron spin relaxation times are comparable. In fact, not only are they comparable, they are quite long (~5 μs),[14] so they do not impact the time dependence in Figure 2 significantly.

Figure 3 shows the complete acid strength dependence of the TREPR spectra for the system in Scheme 1, collected at the same delay time (500 ns) after the laser flash. There are many interesting features in these spectra, not the least of which is that this PCET chemistry is remarkably robust; it should be noted that the overall reaction returns both the Ru complex and the HQ radicals to their starting condition, that is, the entire process is fully reversible and appears to be so at all "pH" values, including some rather extreme conditions. Indeed, to collect one TREPR spectrum we apply a minimum of 6000 laser pulses, and all of the spectra in Figure 3 were obtained with the same sample without loss of signal strength at any point in the experiments. It should also be noted that there is a small absorption of the H_2Q species (and its conjugate base HQ^-) at 355 nm. However, the PCET reaction is not observed by either TA or TREPR spectroscopy unless the Ru complex is present, and we observe similar TREPR spectra when exciting at 440 nm, but with poorer S/N ratios (due to lower laser pulse energies). For this reason, all TREPR experiments reported here were carried out at 355 nm.

At low acid strengths (high "pH"), the deprotonated radical anion **4b** is the only species detected. There are four equivalent protons in the radical anion, leading to a sharp 1:4:6:4:1 quintet in the TREPR spectrum. As the acid strength is increased, the spectrum due to protonated structure **4a** appears in the spectrum, superimposed on that from **4b**. Radical **4a** has a different splitting pattern, due to changes in the ring proton hyperfine coupling constants that are no longer equivalent, plus the addition of a new hyperfine coupling from the −OH proton. The resulting pattern is therefore a triplet of doublets of triplets (the smallest triplet is not easily resolved in this solvent system), making each radical clearly distinguishable. Further increase in acid strength leads to an increase in the ratio of signals from **4a** to those from **4b**, as expected.

As the system moves to a strongly acidic medium, the protonated structure gradually becomes the only paramagnetic species observed in the TREPR experiment (pH meter reading of 3.6). However, further increases in acid strength reveal a broadening of all transitions, followed by sharpening to a final TREPR spectrum at very high acid strength (low "pH") that again consists of five lines. The broadening observed at low pH values can be attributed to the observation of the exchange process between the −OH proton in the solvent. This reaction will scramble the spin state of this proton, first leading to broadening and then to a sharp spectrum when the exchange reaction is fast relative to the time scale of observation. The maximum broadening is defined by the difference in resonant frequencies for hyperfine lines of the neutral vs the protonated species, which is about 4×10^6 s^{-1} (based on the 1.7 G −OH hyperfine couping constant). The rate of proton exchange for phenol, a related structure with a similar pK_a, at similar acid strengths has been reported in the literature to be 1.7×10^7 s^{-1} M^{-1}.[21] Applying this bimolecular rate constant to a concentration of H_2Q = 0.47 M, an exchange rate of 8×10^6 s^{-1} M^{-1} is expected, which is in reasonable agreement with the experimentally observed exchange rate.

The fully sharpened spectrum at high acid strength appears as if the −OH proton is absent, similar to the broadening or even disappearance of transitions when there is fast exhange of −OH protons in NMR spectroscopy with water or alcohol solvents. This observation is also consistent with the spectra of Jäger et al.[14] The five line spectrum observed at the bottom of Figure 3 represents a structure where the nuclear spin state of the −OH proton is indeterminate, and the remaining ring protons all have similar coupling constants. In fact, the ring protons are not quite equivalent, as the observed transitions are still quite broad; the spectrum is probably better described as two almost overlapping triplets rather than a true quintet.

Acid/Base Strength Dependence: TA Studies. In our previous communication,[7] TA experiments were carried out using an apparatus that, for technical reasons, provided rather coarse spectral resolution. As a result, significant interpolation around the transient signal from radical **4a** was necessary. Figure 4 shows TA data, acquired at two different acid strengths for the system in Scheme 1, acquired on an apparatus specifically constructed to avoid interpolation in order to clearly observe radical **4a**. This was accomplished by recording the full spectra at one time point instead of the previous method recording single wavelength intensity and lifetime and building up the full spectra. Each complete spectrum of the transient data was acquired per laser pulse, and built up to display the transient data through averaging 20 pump and pump−probe spectra for the transient subtraction. Each spectrum was acquired in a single shot with many more data points on the wavelength axis than the TA spectrum reported in ref 6.

The primary spectral features of the ruthenium complex (ligand-based radical **3**) are apparent at about 435 and 535 nm in Figure 4A. There is a shoulder on the high energy side of the 435 nm band at about 415 nm, which is known to correspond to the semiquinone radical, $HQ^\bullet$ (radical **4a**).[7] This spectrum was acquired at a low pH (meter reading of pH = 1.8) by the addition of 2 M HCl. The TA data set acquired in the unaltered (natural) pH = 4.9 is shown for comparison in Figure 4C. The changes observed in the behavior of the complex-based species

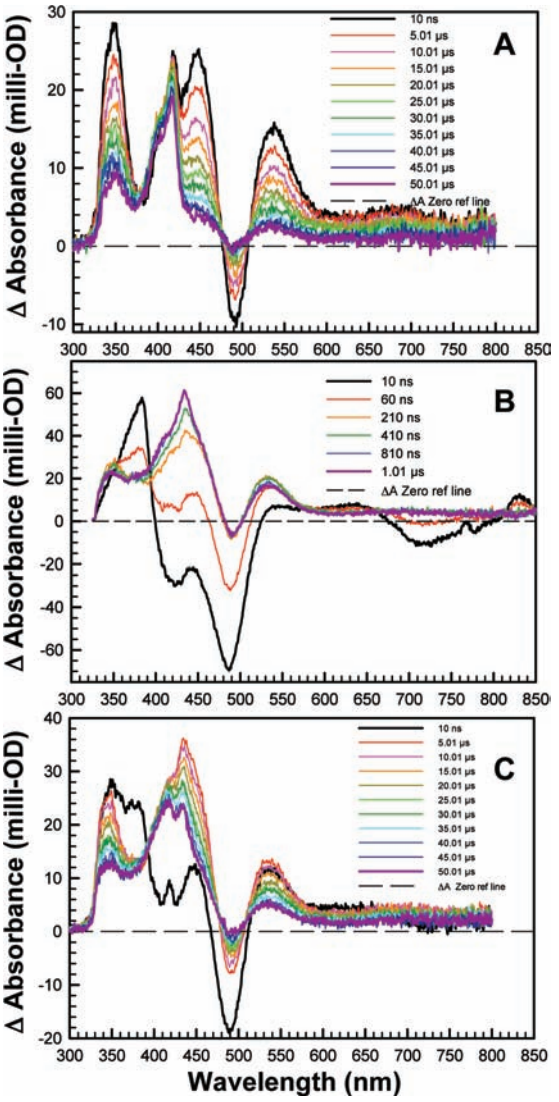

Figure 4. Transient optical absorption spectra for the PCET reaction between **1** and H_2Q collected at varying delay times following a laser pulse in 1:1 CH_3CN/H_2O prepared at 57 μM in **1** and 0.1 M in KPF_6 for ionic strength. (A) 0.47 M H_2Q, pH meter reading = 1.8, 5 μs steps, (B) 0.2 M H_2Q, pH meter reading = 2.0, 50−200 ns steps, (C) 0.47 M H_2Q, unadjusted pH meter reading = 4.9, 5 μs steps.

(**3**) are, most notably, a more rapid decay and spectral shift of the 435 nm feature to lower energy at the higher acid strength. This uncovers the 415 nm shoulder of **4a**, and the faster decay of the excited state spectrum allows for better resolution of the total peak shape of the semiquinone feature. Also, at the earliest possible observation time (Figure 4A, 10 ns spectrum), the 415 nm peak due to **4a** is immediately observed at a pH meter reading of 1.8, but at a lower acid strength (pH meter reading of 4.9), this peak has not yet appeared (Figure 4C, 10 ns spectrum). This observation is in line with the prediction above that the PCET reaction kinetics will depend on the pK_a of the donor, that is, the thermodynamics of the proton transfer component can assist the electron transfer component of the PCET event. The data in Figure 4B were also acquired at high acid strength but with a lower concentration of H_2Q, showing that the rise of the signal from **4a** at 415 nm can be resolved under these conditions.

Chart 1

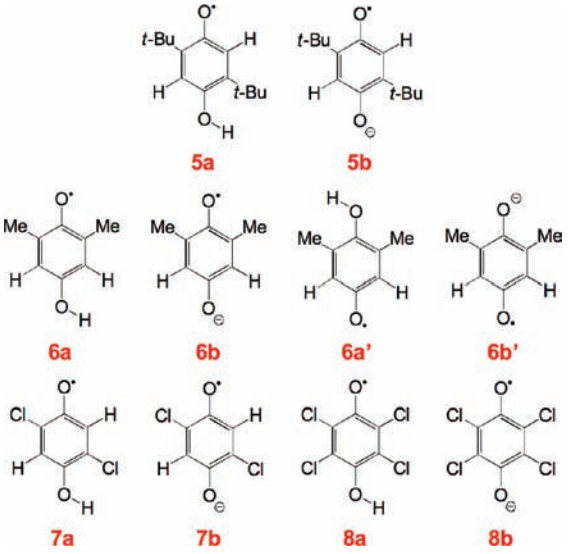

At high "pH" values (low acid strength or strongly basic solutions), there may be significant quenching of the Ru complex excited state by the hydroxide ion itself. While it has been suggested that this can take place via formation of molecular oxygen through Ru complex reduction by hydroxide ion,[22] it is more likely to be due to photosubstitution. An additional complication is that the H_2Q may already be deprotonated in the H-bonded complex (pK_a = 9.5). This means that the quenching mechanism may switch from PCET to direct ET. The same radical (**4b**) will be observed in this case, so we cannot distinguish these processes by TREPR. Indeed, TA spectra obtained at high "pH" values (not shown) show a dramatic change in their kinetics due to a much faster quenching process. While it is not possible to determine a partitioning between the two quenching agents (hydroxide or hydroquinone) by TA, we know that at least some of the quenching must be due to the hydroquinone because we observe a significant signal from radical **4b** under basic conditions in both TA and TREPR spectra. If all of the quenching were due to hydroxide ion, no TREPR spectrum of either **4a** or **4b** would be observed. The possibility of direct ET quenching will arise again in our discussion below regarding H_2Q substituent effects on this photochemistry.

H_2Q Substituent Effects. As part of our investigation into the PCET mechanism for these complexes, we investigated the role of electron withdrawing versus electron donating substituents. The structures of the different H_2Qs and the ensuing radicals from the PCET reaction are shown in Chart 1. Our reasoning for investigating two alkyl-substituted H_2Q structures was to understand the differences between symmetrically and unsymmetrically substituted radicals. In other words, for the 2,5-di-*tert*-butyl substitution pattern, it does not matter which OH group of the H_2Q molecule binds to the complex in the excited state due to the inherent C_{2h} symmetry. However, for 2,6-dimethyl substitution, the H-bond between H_2Q and the Ru complex can form with the OH group either ortho (**6a**/**b**) or meta (**6a′**/**6b′**) to the methyl groups. The radicals or radical anions produced in each case should be easily distinguished by their hyperfine coupling constants.

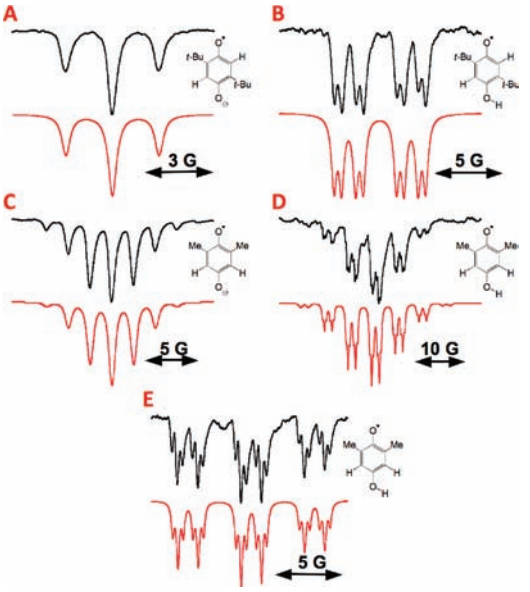

Figure 5. TREPR spectra (black = experimental, red = simulated) collected after a 355 nm laser pulse for the PCET reaction between **1** (150 μM) with 2,5-di-*tert*-butylH_2Q (~0.1 M, A,B), and **1** with 2,6-dimethylH_2Q (0.5 M, C, D, E). (A) Spectrum of **5b** collected at 500 ns at "pH" = 11.7; (B) Spectrum of **5a** collected at 500 ns at "ambient" pH (ca. pH = 5); (C) Spectrum of **6b** collected at 500 ns in basic solution; (D) Spectrum of **6a** collected at 800 ns ca. pH = 5; (E) Central lines of **6a** from (D). Simulation parameters: **5b**, A(-H) = 2.21 G (2H); **5a**, A(*o*-H) = 4.65 G (1H), A (*m*-H) = 0.56 G (1H), A(-OH) = 1.61 G (1H); **6b**, A(-Me) = 2.01 G (6H); A(-H) = 0.20 G (2H); **6a**, A(-Me) = 4.69 G (6H), A(-H) = 0.39 G (2H), A(-OH) = 1.5 G (1H).

Figure 5 shows TREPR spectra obtained at low (Figure 5A) and high (Figure 5B) acid strengths for the $[Ru^{II}(bpy)_2bpz]^{2+}$ complex with 2,5-di-*tert*-butylhydroquinone. The hyperfine splitting pattern in the anion radical **5b** is a 1:2:1 triplet from two equivalent protons. The methyl groups on the *tert*-butyl group do not couple effectively to the ring system, therefore, the two equivalent ring protons are the only couplings observed. Note the extreme base strength required to observe radical anion **5a**.

Dropping the base strength even slightly from these conditions leads to the TREPR spectrum from the protonated structure (**5a**), shown in Figure 5B. For this radical, the ring protons are no longer equivalent, and the resulting spectrum is a doublet of doublets that is further split into another set of doublets by the −OH proton. Spectral simulation reveals an interesting feature: the intensity ratio of each transition within a set of doublets should be 1:1, as in the simulation. Experimentally, this is clearly not the case, with the high field line more intense in each doublet. Analysis of this effect, which is unique to the smallest coupling constant in each radical, has no effect on the relative intensity ratio of radical **4a** to radical **4b**. This effect is most likely due to a spin polarization process connected to the rate of separation of the radicals after the PCET event is complete. We will address this issue in a separate future publication.

Figure 5C and D show TREPR spectra obtained from PCET reactions with 2,6-dimethylhydroquinone under basic and acidic conditions, respectively. There are two interesting and distinctive features of these spectra: (1) the radical anion (structure **6b** in Chart 1) produced is clearly that from a PCET reaction involving H-bonding between the Ru complex and the OH closer to the methyl groups. At first glance this seems counterintuitive: the position of methyl groups should favor H-bonding to the *meta*-OH group, based on both steric and electronic arguments. However, H-bonding involving the closer OH group might be favored if it places the methyl groups above and below the ligand π system, known to be a stabilizing interaction.[23] (2) From the simulation of the 2,6-dimethyl radical **6a** in Figure 5E (only the central transitions are shown), an additional intensity discrepancy is observed for the two equivalent ring protons: A 1:2:1 intensity is expected, but once again the high field transition has stronger emissive polarization than the low field one for each triplet in the spectrum. Note that this phenomenon repeats across the entire spectrum, even on the high field side, suggesting that it is a multiplet polarization phenomenon connected to the hyperfine coupling constant. Again, we attribute this to a CIDEP process that depends on the radical separation rate, and this will be analyzed and discussed in a separate paper. We note here that these intensity discrepancies are within mulitplets assigned to one individual radical, and are not related to the overall integrated intensity.

Finally, we examined the chemistry in Scheme 1 with electron withdrawing groups on the H_2Q ring, leading to chlorinated radicals **7b** and **8b** in Chart 1. For these substitutions on the ring, it is highly unlikely that the protonated structure can be formed in CH_3CN/H_2O solutions (Table 1 lists $pK_a = 0$ for $HQ^{\bullet}$ with this substitution pattern). It is also more likely that the quenching mechanism is direct ET rather than PCET (again from Table 1, E^0 for this substitution pattern is +699 mV). We proceeded with these experiments mainly to test the robustness of the system and for completeness, that is, to run the reaction under all pH ranges and H_2Q structures. Running the experiments in carefully dried CH_3CN might allow for the creation of the protonated species **7a** and **8a** by removing the possibility of deprotonation by the solvent. Figure 6 shows the TREPR results for these compounds. In Figure 6A, a triplet from radical anion **7b** is clearly observed. Removal of water from the solvent system leads to the spectrum shown in Figure 6B. In this spectrum there is now an additional splitting (a large doublet) and the two ring protons have lost their equivalence. The substantial broadening of these transitions may be due to the presence of trace water in the system, that could provide a mechanism for a nominal amount of −OH proton exchange leading to broadening (the spec sheet for the solvent used lists a maximum water content of 50 ppm, which corresponds to 2.7 mM).

Figure 6C shows the TREPR spectrum obtained for the tetrachlorinated H_2Q compound, which has no protons and therefore shows a single line in basic solution due to radical anion **8b**. In dry CH_3CN, the spectrum is unusual in appearance (Figure 6D); the sharp singlet from **8b** appears to be superimposed on a broad signal that is also somewhat anisotropic in its line shape. It is possible that complete protonation of the tetrachlorinated anion may not be possible even under our driest conditions. The −OH proton in this structure is expected to be extremely acidic. We note the complete reversibility of the system even under these extreme conditions, with no evidence for degradation over substantial time periods.

Ligand Substitution Effects. Because the effects of substitution on the H_2Q ring system are so pronounced in this chemistry, it is of interest to investigate the effect of different ligands as well. In this regard, the same photochemistry was carried out with the 6,7-dimethyl-2-(pyridin-2-yl)quinoxaline ($[Ru^{II}(bpy)_2(Me_2\text{-}PQ)]^{2+}$), whose structure is shown in Chart 2. Figure 7 shows the TREPR spectrum obtained from the PCET reaction in Scheme 1 using $[Ru^{II}(bpy)_2(Me_2\text{-}PQ)]^{2+}$ and the parent H_2Q molecule, in

Scheme 3

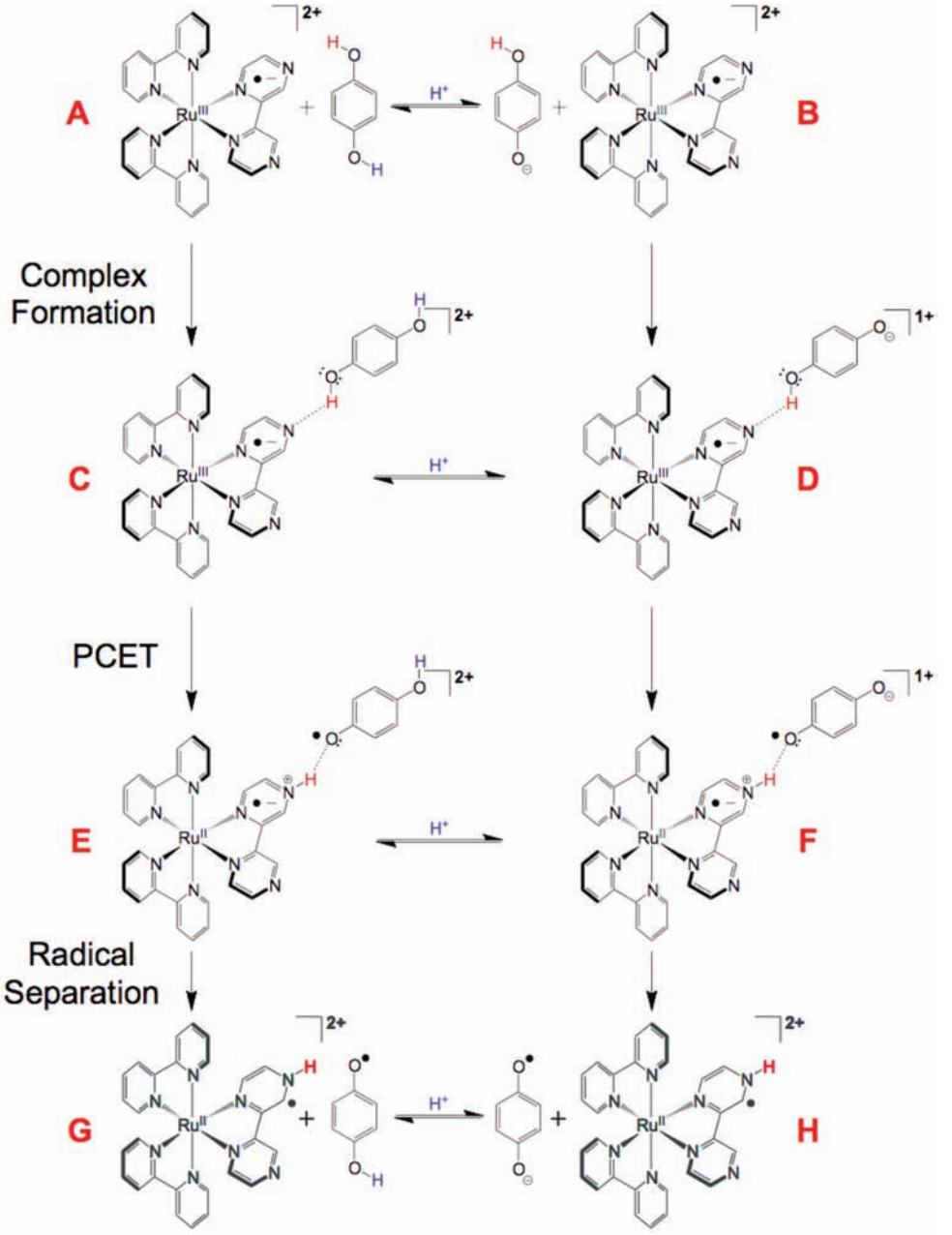

comparison to that obtained using the $[Ru^{II}(bpy)_2(bpz)]^{2+}$ compound, under acid strength conditions that were adjusted to be nearly equal. Comparison of Figure 7A to Figure 7B indicates that the ratio of **4a** to **4b** changes significantly between the two complexes (see labeled arrows in Figure).

To understand the differences between the spectra in Figure 7, it is useful to consider the four acid/base equilibria outlined in Scheme 3 and to assess their involvement in the PCET reaction in regard to TREPR spectral intensities. There is no measurable interaction between the Ru complexes and added H_2Q in their ground states, and the presence of H_2Q does not change the measured acid strengths in these solutions. For these reasons, we do not expect the A/B acid/base equilibrium to be of any consequence in this photochemistry. While complex formation is more favorable for A than for B (pK_a for H_2Q is 9.85 versus 11.2 for HQ^-, Table 1), on the nanosecond time scale, the TREPR and TA experiments are insensitive to the A/B equilibrium. The C/D equilibrium should follow the same trend in pK_a values as the A/B equilibrium (this assumes that the weak H-bond in the complex exerts a minimal effect on the acid strength of the para OH group proton). This means that below pH values of 9.5, structure C will dominate.

The E/F equilibrium is important because now we are dealing with structures similar to $HQ^\bullet$ and $Q^{\bullet-}$ (Scheme 3, note that the ligand in E and F is drawn as the zwitterionic resonance structure). With the pK_a of $HQ^\bullet$ = 4.1, the E/F reaction will be rapidly reversible at pH values near 4. The position of this equilibrium is a function of the relative strengths of the O−H

dx.doi.org/10.1021/jp200381n |*J. Phys. Chem. A* 2011, 115, 3346–3356

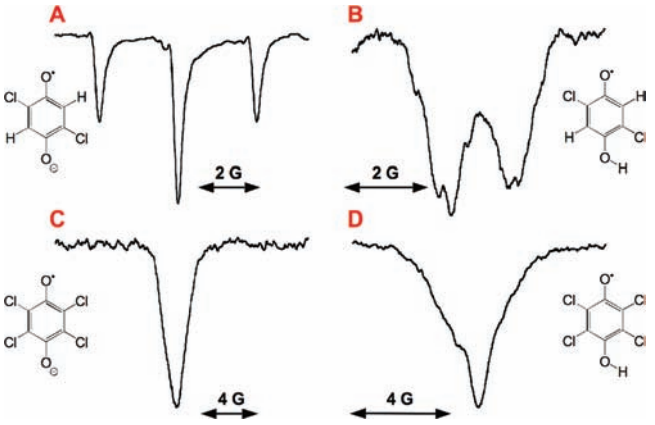

Figure 6. TREPR spectra collected 500 ns after a 355 nm laser pulse for the PCET reaction between **1** (150 μM) and 2,5-dichlorohydroquinone (A, B, 0.5 M) and 2,3,5,6-tetrachlorohydroquinone (C, D, 0.5 M). (A) Spectrum of **7b** in CH_3CN/H_2O; (B) Spectrum of **7a** in anhydrous CH_3CN; (C) Spectrum of **8b** in CH_3CN/H_2O; (D) Spectrum of **8a** in anhydrous CH_3CN.

Chart 2

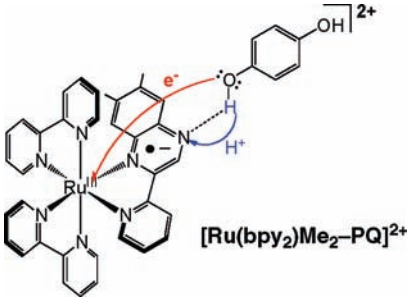

bonds and the N−H bonds in the two complexes (E or F) *after* the PCET reaction has taken place. The O−H bond strengths are determined more by the nature of the H_2Q moiety, whereas the N−H bond strengths are mostly determined by the ligand properties, particularly their relative base strengths. Empirical calculations of the pK_a values for the protonated ligands have been carried out:[24] for Me_2-PQ the pK_a is 0.03 ± 0.19, and for bpz the pK_a is −0.63 ± 0.1. We hypothesize that the more basic ligand will have a stronger N−H bond and as such should facilitate radical separation. If the separation rate is comparable to the E/F interconversion rate, then the ratio of **4a** to **4b** in the TREPR spectrum should be governed by the E/F equilibirum, which we established above is a function of the ligand base strength.

Figure 7 shows this to be precisely the case. The PCET reaction involving the more basic Me_2-PQ ligand shows a stronger TREPR signal for radical **4a**, while that involving the less basic bpz ligand shows a larger signal for radical **4b**. In other words, the intensity ratio of these two radicals in the TREPR experiment at the earliest delay times is determined by the E/F equilibrium. It is instructive to consider a comparison of spectra collected by Jäger et al.[14] for the photochemical reduction of benzoquinone at similar delay times (1 μs) to the data presented here for the $[Ru^{II}(bpy)_2(bpz)]^{2+}$ compound in Figure 2 (1.2 μs). We observe a larger intensity of the anion, which reflects the

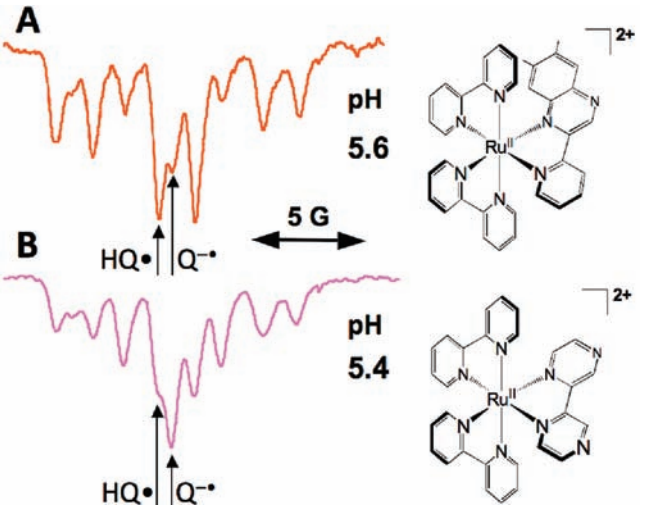

Figure 7. TREPR spectra collected 500 ns after a 355 nm laser pulse in 1:1 CH_3CN/H_2O solution during the PCET reaction between H_2Q (0.5 M) with the ^{3}MLCT state of (A) $[Ru^{II}(bpy)_2(Me_2\text{-}PQ)]^{2+}$ (Chart 2, 150 μM), and (B) $[Ru^{II}(bpy)_2(bpz)]^{2+}$ (**1**, Scheme 1, 150 μM). Note the change in intensity of radical **4a** to **4b** as a function of the ligand.

influence of the E/F equilibrium and the role of the ligand in observed **4a**/**4b** ratio in this work.

At longer delay times, the G/H equilibrium (shown with the Ru complex radicals faded in Scheme 3 as they are not involved) is more important than the A/B equilibrium because the pK_a values are now much lower (4.1 for $HQ^\bullet$ (**4a**) in G/H vs 9.85 for H_2Q in A/B). This is exemplified by the time dependence in Figure 2, where the TREPR spectrum due to **4b** becomes gradually more intense on the microsecond time scale. If the ligand had no effect on either the E/F equilibrium or the radical separation rate, the ratio of **4a** to **4b** would be expected to be the same at similar pH values, and the G/H equilibrium would then dominate all observed spectral intensities.

Our observation that the ratio of **4a** to **4b** in the TREPR spectra is largely determined by the E/F equilibrium strongly suggests that there should exist an equilibrium isotope effect[25] in this chemistry. Indeed, comparison of Figures 1A and 1B show different ratios of radicals **4a** to **4b** as a function of deuteriation of the −OH proton. This ratio (from integrated TREPR intensities) is 67:33 for the protonated structure and 91:9 for the deuteriated compound. This correlates well with the observed pK_a values for phenol vs deuteriated phenol (9.95 vs 9.99, respectively[26]), i.e., we observe a greater TREPR intensity for radical **4a** when we have the less acidic −OD group present.

We make one final comment about the relative signal intensities between spectra collected using $[Ru^{II}(bpy)_2(bpz)]^{2+}$ versus $[Ru^{II}(bpy)_2(Me_2\text{-}PQ)]^{2+}$ and H_2Q (Figures 7A and 7B). The spectrum from $[Ru^{II}(bpy)_2(Me_2{-}PQ)]^{2+}$ is substantially weaker, and there may be several reasons for this. It is possible that there is simply less triplet mechanism spin polarization created in the ^{3}MLCT state of $[Ru^{II}(bpy)_2(Me_2\text{-}PQ)]^{2+}$, or the triplet states of the two complexes may have different electron spin relaxation times. These two possibilities are unlikely because of the similarities in orbital symmetry and metal oxidation state. A third possibility could arise from different electron spin relaxation rates in the H-bonded complex. This might be caused by the different base strengths of the ligands. If the PT component of the PCET reaction "leads" slightly before the ET component,

significant radical character can build up on the ligand. Because this radical center is close to the metal center, its electron spin will relax at a faster rate, destroying polarization. Because Me_2-PQ is a stronger base than bpz, proton transfer is expected to go faster for this ligand. We favor this explanation because it is based on ligand rather than metal properties.

CONCLUSIONS

The PCET reaction between the $[Ru^{II}(bpy)_2bpz]^{2+3}$MLCT state (**2**) and several H-bonded H_2Q molecules has been studied in detail by TREPR and TA. The large spin polarization from the triplet mechanism of CIDEP, coupled with the fast spin relaxation of the ligand radical, allows for clean observation of the $HQ^{\bullet}$ radicals in equilibrium with their conjugate bases in CH_3CN/H_2O mixtures. There is a strong acid strength dependence of this chemistry, leading to a change in mechanism from PCET to ET in either basic solution or with strong electron withdrawing groups on the H_2Q ring through their influence on E^0 for the H_2Q donor. Depending on the acid strength of the solution, either a superposition of $HQ^{\bullet}$ (**4a**) and $Q^{\bullet-}$ (**4b**) is observed or a broad spectrum is observed due to their dynamic equilibrium. Substituent effects on H_2Q or the Ru complex alter the acid strength dependence substantially, and these effects manifest themselves as changes in the TREPR signal intensities, in particular, the **4a**/**4b** ratios for each system. The TA results show a major change in the kinetics in basic solution indicating that direct ET quenching is operational under these conditions. This PCET system overall remains robust under all conditions, making it ideal for further study in regard to new catalytic reactions, especially potential CO_2 reduction or other chemical reactions using the ligand radical **3**.

ASSOCIATED CONTENT

Supporting Information. Deconvolution of the spectral simulations presented in Figures S1 and S2. This material is available free of charge via the Internet at http://pubs.acs.org.

AUTHOR INFORMATION

Corresponding Author
*E-mail: mdef@unc.edu.

ACKNOWLEDGMENT

This material is based upon work supported as part of the UNC EFRC: Solar Fuels and Next Generation Photovoltaics, an Energy Frontier Research Center funded by the U.S. Department of Energy, Office of Science, Office of Basic Energy Sciences under Award Number DE-SC0001011, supporting the work of J. J.C. (synthesis), M.K.B. (photophysical measurements), R.D.S. and N.V.L. (electron paramagnetic resonance measurements). M.D.E.F. thanks the NSF for partial support of the TREPR instrumentation through Grant No. CHE-0809530. T.J.M. acknowledges partial support from NSF through Grant CHE-0957215 for experiment design and synthesis. M.J.T. thanks the NSF for infrastructural support through the NSEC program (DMR-04-25780). We also acknowledge support for the purchase of instrumentation from UNC EFRC (Solar Fuels and Next Generation Photovoltaics, an Energy Frontier Research Center funded by the U.S. Department of Energy, Office of Science, Office of Basic Energy Sciences under Award Number DE-SC0001011) and UNC SERC ("Solar Energy Research Center Instrumentation Facility" funded by the U.S. Department of Energy, Office of Energy Efficiency and Renewable Energy under Award Number DE-EE0003188).

REFERENCES

(1) (a) Cukier, R. I.; Nocera, D. G. *Annu. Rev. Phys. Chem.* **1998**, *49*, 337. (b) Huynh, M. H. V.; Meyer, T. J. *Chem. Rev.* **2007**, *107*, 5004. (c) Reece, S. Y.; Hodgkiss, J. M.; Stubbe, J.; Nocera, D. G. *Philos. Trans. R. Soc., B* **2006**, *361*, 1351. (d) Reece, S. Y.; Nocera, D. G. *Annu. Rev. Biochem.* **2009**, *78*, 673.

(2) (a) Hammarström, L.; Hammes-Schiffer, S. *Acc. Chem. Res.* **2009**, *42*, 1859. (b) Alstrum-Acevedo, J. H.; Brennaman, M. K.; Meyer, T. J. *Inorg. Chem.* **2005**, *44*, 6802. (c) Mayer, J.; Rhile, I.; Larsen, F.; Mader, E.; Markle, T.; DiPasquale, A. *Photosynth. Res.* **2006**, *87*, 3. (d) Meyer, T. J. *Acc. Chem. Res.* **1989**, *22*, 163. (e) Wasielewski, M. R. *Chem. Rev.* **1992**, *92*, 435.

(3) (a) O'Regan, B.; Grätzel, M. *Nature* **1991**, *353*, 737. (b) Grätzel, M. *Nature* **2001**, *414*, 338–344. (c) Grätzel, M. *Inorg. Chem.* **2005**, *44*, 6841.

(4) (a) Gust, D.; Moore, T. A.; Moore, A. L. *Acc. Chem. Res.* **2000**, *34*, 40. (b) Lewis, N. S.; Nocera, D. G. *Proc. Natl. Acad. Sci. U.S.A.* **2006**, *103*, 15729. (c) Gust, D.; Moore, T. A.; Moore, A. L. *Acc. Chem. Res.* **2009**, *42*, 1890. (d) Gagliardi, C. J.; Westlake, B. C.; Kent, C. A.; Paul, J. J.; Papanikolas, J. M.; Meyer, T. J. *Coord. Chem. Rev.* **2010**, *254*, 2459.

(5) Dresselhaus, M. S.; Thomas, I. L. *Nature* **2001**, *414*, 332.

(6) (a) Rappaport, F.; Boussac, A.; Force, D. A.; Peloquin, J.; Brynda, M.; Sugiura, M.; Un, S.; Britt, R. D.; Diner, B. A. *J. Am. Chem. Soc.* **2009**, *131*, 4425. (b) Jenson, D. L.; Barry, B. A. *J. Am. Chem. Soc.* **2009**, *131*, 10567.

(7) Concepcion, J. J.; Brennaman, M. K.; Deyton, J. R.; Lebedeva, N. V.; Forbes, M. D. E.; Papanikolas, J. M.; Meyer, T. J. *J. Am. Chem. Soc.* **2007**, *129*, 6968.

(8) Patel, K. B.; Willson, R. L. *J. Chem. Soc., Faraday Trans. I* **1973**, *69*, 814.

(9) Clancy, C. M. R.; Tarasov, V. F.; Forbes, M. D. E., Time-Resolved EPR Studies in Organic Photochemistry. In *Specialist Periodical Report: Electron Paramagnetic Resonance*; The Royal Society of Chemistry: Cambridge, Great Britian, 1998; Vol. 16, p 50.

(10) Harbron, E. J.; Forbes, M. D. E. Chemically-Induced Nuclear and Electron Polarization (CIDNP and CIDEP). *Encyclopedia of Chemical Physics and Physical Chemistry*; IOP Publishing: London, 2001; Chapter B1.16, p 1389.

(11) Atkins, P. W.; Evans, G. T. *Chem. Phys. Lett.* **1974**, *25*, 108.

(12) Kuciauskas, D.; Monat, J. E.; Villahermosa, R.; Gray, H. B.; Lewis, N. S.; McCusker, J. K. *J. Phys. Chem. B* **2002**, *106*, 9347.

(13) Smith, I. C. P.; Carrington, A. *Mol. Phys.* **1967**, *12*, 439.

(14) Jäger, M.; Yu, B. C.; Norris, J. R. *Mol. Phys.* **2002**, *100*, 1323.

(15) (a) van Slageren, J.; Martino, D. M.; Kleverlaan, C. J.; BussandriA. P.; van Willigen, H.; Stufkens, D. J. *J. Phys. Chem. A* **2000**, *104*, 5969–5973. (b) Kleverlaan, C. J.; Martino, D. M.; van Slageren, J.; van Willigen, H.; Stufkens, D. J. *Appl. Magn. Reson.* **1998**, *15*, 203–214. (c) Martino, D. M.; Kleverlaan, C. J.; van Slageren, J.; Bussandri, A.; van Willigen, H. *Appl. Magn. Reson.* **2004**, *26*, 489.

(16) Rich, P. R.; Bendall, D. S. *Biochim. Biophys. Acta* **1980**, *592*, 506.

(17) Boully, L.; Turck, A.; Plé, N.; Darabantu, M. *J. Heterocycl. Chem.* **2005**, *42*, 1423.

(18) Rillema, D. P.; Allen, G.; Meyer, T. J.; Conrad, D. *Inorg. Chem.* **1983**, *22*, 1617.

(19) (a) Lebedeva, N. V.; Forbes, M. D. E. Carbon-Centered Radicals and Radical Cations. In *Wiley Series on Reactive Intermediates in Chemistry and Biology*; Forbes, M. D. E., Ed.; Wiley: New York, 2010; Vol. 3, Chapter 14, p 323. (b) Forbes, M. D. E. *Photochem. Photobiol.* **1997**, *65*, 73.

(20) Gagliardi, L. G.; Castells, C. B.; Rafols, C.; Roses, M.; Bosch, E. *Anal. Chem.* **2007**, *79* (8), 3180.

(21) Grunwald, E.; Puar, M. S. *J. Phys. Chem.* **1967**, *71*, 1842.

(22) Creutz, C.; Sutin, N. *Proc. Natl. Acad. Sci. U.S.A.* **1975**, *72* (8), 2858.

(23) (a) Suezawa, H.; Yoshida, T.; Umezawa, Y.; Tsuboyama, S.; Nishio, M. *Eur. J. Inorg. Chem.* **2002**, *2002*, 3148–3155.(b) Nishio, M.; Hirota, M.; Umezawa, Y., *The CH/pi Interaction: Evidence, Nature, and Consequences*; Wiley-VCH: New York, 1998. (c) Rozas, I.; Alkorta, I.; Elguero, J. *J. Phys. Chem. A* **1997**, *101*, 9457.

(24) Calculated using *Advanced Chemistry Development Software*, V11.02; ACD/Laboratories: Toronto, CA, 1994−2011.

(25) (a) Knyazev, D. A.; Myasoedov, N. F.; Bochkarev, A. V. *Russ. Chem. Rev.* **1992**, *61*, 204. (b) Sheinkman, A. K.; Suminov, S. I.; Kost, A. N. *Russ. Chem. Rev.* **1973**, *42*, 642.

(26) Matsumoto, M.; Espenson, J. H. *Organometallics* **2005**, *24*, 2780.

THE JOURNAL OF PHYSICAL CHEMISTRY Letters

LETTER

pubs.acs.org/JPCL

Photoinduced Stepwise Oxidative Activation of a Chromophore−Catalyst Assembly on TiO_2

Wenjing Song, Christopher R. K. Glasson, Hanlin Luo, Kenneth Hanson, M. Kyle Brennaman, Javier J. Concepcion, and Thomas J. Meyer*

Department of Chemistry, University of North Carolina at Chapel Hill, Chapel Hill, North Carolina 27599, United States

Supporting Information

ABSTRACT: To probe light-induced redox equivalent separation and accumulation, we prepared ruthenium polypyridyl molecular assembly $[(dcb)_2Ru(bpy\text{-}Mebim_2py)Ru(bpy)(OH_2)]^{4+}$ ($Ru_a^{II}-Ru_b^{II}-OH_2$) with Ru_a as light-harvesting chromophore and Ru_b as water oxidation catalyst (dcb = 4,4′-dicarboxylic acid-2,2′-bipyridine; bpy-Mebim$_2$py = 2,2′-(4-methyl-[2,2′:4′,4″-terpyridine]-2″,6″-diyl)bis(1-methyl-1H-benzo[*d*]imidazole); bpy = 2,2′-bipyridine). When bound to TiO_2 in nanoparticle films, it undergoes MLCT excitation, electron injection, and oxidation of the remote $-Ru_b^{II}-OH_2$ site to give $TiO_2(e^-)-Ru_a^{II}-Ru_b^{III}-OH_2^{3+}$ as a redox-separated transient. The oxidized assembly, $TiO_2-Ru_a^{II}-Ru_b^{III}-OH_2^{3+}$, similarly undergoes excitation and electron injection to give $TiO_2(e^-)-Ru_a^{II}-Ru_b^{IV}=O^{2+}$, with $Ru_b^{IV}=O^{2+}$ a known water oxidation catalyst precursor. Injection efficiencies for both forms of the assembly are lower than those for $[Ru(bpy)_2(4,4'\text{-}(PO_3H_2)_2bpy)]^{2+}$ bound to TiO_2 (TiO_2-Ru^{2+}), whereas the rates of back electron transfer, $TiO_2(e^-) \rightarrow Ru_b^{III}-OH_2^{3+}$ and $TiO_2(e^-) \rightarrow Ru_b^{IV}=O^{2+}$, are significantly decreased compared with $TiO_2(e^-) \rightarrow Ru^{3+}$ back electron transfer.

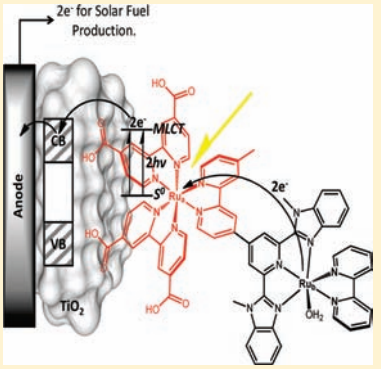

SECTION: Energy Conversion and Storage

Utilization of dye-sensitized photoelectrosynthesis cells (DSPEC) for water splitting into H_2 and O_2 or photodriven reduction of CO_2 is a promising approach to generate solar fuels.[1−4] In these applications, sequential accumulation of multiple redox equivalents at catalytic sites by multiphoton excitation is a key feature to avoid high energy $1e^-$ intermediates.[1,5] Additional complications arise from nonproductive electron−hole recombination (back electron transfer) in competition with activation and chemical conversion at the catalyst site. Successful competition with back electron transfer has been achieved with added scavengers, but the reactivity challenge is far greater for the multielectron, multiproton half reactions for water oxidation, $2H_2O \rightarrow O_2 + 4H^+ + 4e^-$, or CO_2 reduction, for example, $CO_2 + 2e^- + 2H^+ \rightarrow CO + H_2O$. Recently, Karlsson et al. reported a one chromophore−two donor system that forms a 2-hole (2-oxidative equivalent) redox-separated state following transient laser excitation with close to unit efficiency.[6]

One approach to functional DSPEC configurations is based on chromophore−catalyst assemblies on TiO_2 and other large band gap metal oxide semiconductors. Photo-oxidation is driven by excitation and injection by a surface-bound chromophore. Oxidative equivalents produced at the interface are delivered to a catalyst site held spatially separated from the electrode−solution interface.

We previously demonstrated that the surface-bound complex $[Ru(Mebim_2py)(4,4'\text{-}(CH_2PO_3H_2)_2(bpy))(OH_2)]^{2+}$ (**2P**) (Mebim$_2$py =2,6-bis(1-methyl-1*H*-benzo[*d*]imidazol-2-yl) pyridine; P$_2$bpy =4,4′-bis-(methylenephosphonato)-2,2′-bipyridine) on indium-doped tin oxide (ITO) electrochemically catalyzes water oxidation efficiently in aqueous solution and propylenecarbonate (PC)−water mixtures.[7−10] Water oxidation occurs by stepwise proton-coupled electron transfer (PCET) activation to $Ru^{IV}=O^{2+}$, further oxidation to $Ru^{V}=O^{3+}$, O-atom attack on water to give an intermediate peroxide, and further oxidation to release O_2 (Figure 1).

In this Letter, we describe the photophysical properties of a designed molecular chromophore−catalyst assembly on TiO_2. The assembly incorporates a ruthenium polypyridyl chromophore and water oxidation catalyst, $[(dcb)_2Ru(bpy\text{-}Mebim_2py)Ru(bpy)(OH_2)](OTf)_4$ (**1C**: $Ru_a^{II}-Ru_b^{II}-OH_2$, Figure 2, for synthesis and characterization details; see the Supporting Information, S1) (dcb = 4,4′-dicarboxylic acid-2,2′-bipyridine; bpy-Mebim$_2$py = 2,2′-(4-methyl-[2,2′:4′,4″-terpyridine]-2″,6″-diyl)bis(1-methyl-1*H*-benzo[*d*]imidazole); bpy = 2,2′-bipyridine). The current study explored possible photoinduced generation of catalytically active forms (Ru^{IV} and Ru^{V}) at the remote Ru_b site for organic/water oxidations in DSPECs.

Our early observation that **2P** catalyzes water oxidation efficiently in PC−water mixtures[10] is potentially important in the utilization of carboxylate-derivatized complexes such as **1C** for surface binding. Carboxylate-derivatized complexes typically have limited stability on oxide surfaces in water, especially

Received: June 8, 2011
Accepted: June 24, 2011
Published: July 08, 2011

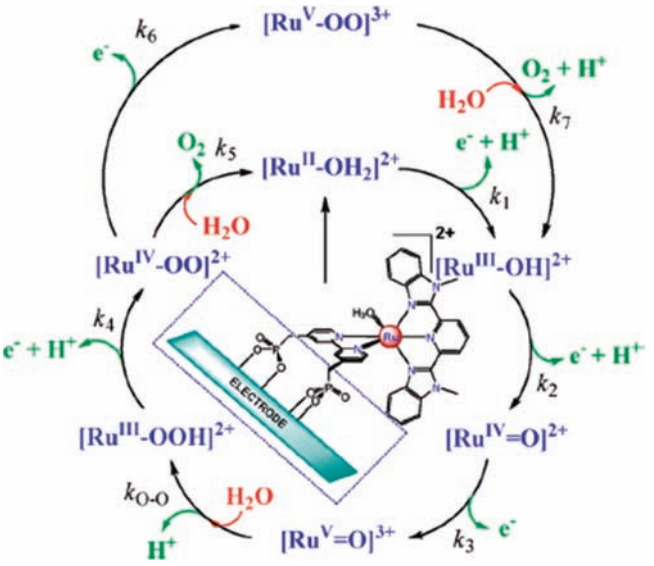

Figure 1. Water oxidation catalysis cycle for the surface bound water oxidation catalyst $[Ru(Mebim_2py)(4,4'\text{-}(CH_2PO_3H_2)_2(bpy))((OH_2)]^{2+}$ (**2P**) on oxide electrodes in aqueous solution.

at high pHs. An important aspect of the current study was to explore the possible use of PC−H_2O mixtures in DSPECs. This is especially relevant for organic oxidations given the favorable solubility and oxidative stability of propylenecarbonate and the fact that it is a noncoordinating solvent for Ru(II)−aqua complexes.[9,10]

In the UV−visible spectrum of **1C** in PC (Figure S3 of the Supporting Information), low-energy metal-to-ligand charge transfer (MLCT) absorption bands appear in the visible at ∼540 nm arising from a lowest energy $d\pi(Ru_b^{II}) \rightarrow \pi^*$(bpy-$Mebim_2py$) transition and overlapping $d\pi(Ru_a^{II}) \rightarrow \pi^*$(bpy-$Mebim_2py$) and $d\pi(Ru_a^{II}) \rightarrow \pi^*(4,4'\text{-}(COOH)_2bpy)$ transitions at 485 nm. The acceptor level in the lowest energy transition is largely based on the $Mebim_2py$ portion of the bridging ligand.

Photoexcitation of the MLCT absorption band of **1C** in PC results in a weakly emitting excited state (**1C***) with an emission maximum at λ_{em} = 850 nm (Figure S4 of the Supporting Information). Emission decay of the excited state, following 484 nm excitation, was dominated by a component with τ = 21 ns (83%) with a minor contributor (17%) with τ = 3.4 ns (Supporting Information, Figure S5). Transient absorption (TA) measurements following 532 nm excitation of **1C** in PC revealed a short-lived (<20 ns) excited state with maximum bleaches at the $d\pi(Ru_a^{II}) \rightarrow \pi^*$(bpy-$Mebim_2py$), $d\pi(Ru_b^{II}) \rightarrow \pi^*$(bpy-$Mebim_2py$) MLCT absorption maxima at 480 and 520 nm. A positive TA feature appeared at 600−700 nm arising from a low-energy $\pi-\pi^*$ absorption for the bpy-$Mebim_2py$ (BL) radical anion ($BL^{-\bullet}$) (Supporting Information, Figure S6). The TA results are consistent with MLCT excitation and subnanosecond decay to the lowest energy $^3[(d\pi^5(Ru_b^{III})\text{-}\pi^*(BL^{-\bullet})]$ MLCT state, eq 1.

$$(4,4'\text{-}(COOH)_2bpy)_2Ru_a^{II}(BL)Ru_b^{II}(bpy)(OH_2)^{4+} \xrightarrow{h\nu} {}^3(4,4'\text{-}(COOH)_2bpy)_2Ru_a^{II}(BL^{-\cdot})Ru_b^{III}(bpy)(OH_2)^{4+*} \quad (1)$$

1C was loaded onto optically transparent *nano*ITO,[11,12] ZrO_2, and TiO_2 thin films from stock solutions in methanol (Supporting Information). The maximum coverage of **1C** on TiO_2 was ∼7.2 × 10^{-8} mol cm^{-2} in a film of ∼6 μm thickness.

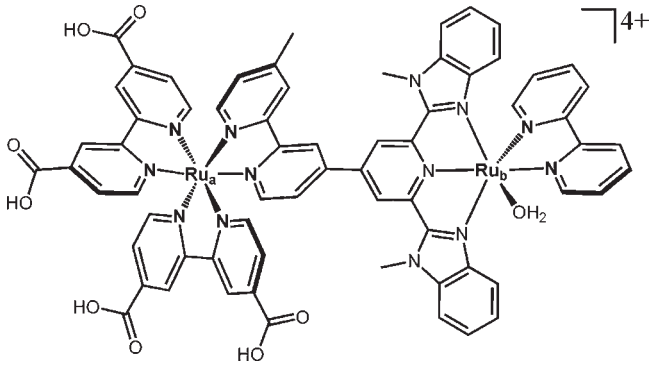

Figure 2. Structure of chromphore-catalyst assembly **1C** $[(dcb)_2Ru(bpy\text{-}Mebim_2py)Ru(bpy)(OH_2)]^{4+}$.

The redox properties of surface-attached **1C** were investigated by spectroelecrochemical measurements on *nano*ITO in 0.1 M KPF_6 in PC with 2% added water (v/v, %). Stepwise oxidation from *nano*ITO−Ru_a^{II}−Ru_b^{II}−OH_2^{2+} to *nano*ITO−Ru_a^{II}−Ru_b^{III}−OH_2^{3+} ($E_{1/2}$ = 0.82 V), to *nano*ITO−Ru_a^{II}−Ru_b^{IV}=O^{2+} ($E_{1/2}$ = 1.26 V), and to *nano*ITO−Ru_a^{III}−Ru_b^{IV}=O^{3+} ($E_{1/2}$ = 1.65 V) was observed (Figure 3B and Table 1). The proton changes at each oxidation step were assumed based on the pH dependent behavior of surface-attached $[Ru(Mebim_2py)(4,4'\text{-}(CH_2PO_3H_2)_2(bpy))((OH_2)]^{2+}$ (**2P**) under the same conditions.[10] The peak currents for the Ru_a^{II}−$Ru^{IV}{}_b$=O^{2+}/Ru_a^{II}−$Ru^{III}{}_b$−OH_2^{3+} wave are noticeably decreased because of slow interfacial oxidation/reduction for this couple as previously observed for **2P**.[9,10,12] Oxidation to *nano*ITO−Ru_a^{II}−Ru_b^{III}−OH_2^{3+} resulted in a decrease in absorbance in the 500−600 nm region with $\Delta\lambda_{max}$ at ∼536 nm indicative of loss of the $d\pi(Ru_b^{II}) \rightarrow \pi^*$(BL) transition. Difference spectra between Ru_a^{II}−Ru_b^{IV}=O^{2+} and Ru_a^{II}−Ru_b^{III}−OH_2^{3+}, between Ru_a^{III}−Ru_b^{IV}=O^{3+} and Ru_a^{II}−Ru_b^{IV}=O^{2+} are characterized by $\Delta\lambda_{max}$ = 500 and 482 nm, respectively (Table 1 and Figure 3A).

Spectroelectrochemistry of *nano*ITO-**1C** in 0.1 M $HClO_4$ aqueous solution reveal redox waves at $E_{1/2}$ = 0.92 V and 1.25 V versus NHE, with associated maximum spectral changes at 518 and 490 nm, respectively (Table 1). The expected wave for the Ru_a^{III}−Ru_b^{IV}=O^{3+}/Ru_a^{II}−Ru_b^{IV}=O^{2+} couple was masked by catalytic current from water oxidation (Supporting Information, Figure S7). Electrochemical generation of Ru_a^{II}−$Ru_b^{III}OH_2^{3+}$ and Ru_a^{II}−Ru_b^{IV}=O^{2+} on TiO_2 gave similar spectral changes (Supporting Information, Figure S8).

Transient spectral changes for **1C** on ZrO_2 (ZrO_2−Ru_a^{II}−Ru_b^{II}−OH_2^{2+}) resembled **1C*** in solution with a maximum ground-state bleach at 480 nm and <20 ns lifetime following 532 nm excitation (Figure S9 of the Supporting Information). In contrast, in the difference spectrum for TiO_2−Ru_a^{II}−Ru_b^{II}−OH_2^{2+} (in PC with 0.2 M $LiClO_4$ and 2% water) following 532 nm laser flash excitation (Figure 4, curve a), a maximum bleach appears between 520 and 540 nm with a much longer lifetime (Figure 4 insert and Table 2). These observations are consistent with the generation of the surface-assembly redox separated state, $TiO_2(e^-)$−Ru_a^{II}−Ru_b^{III}−OH_2^{3+}. Evidence for generation of $TiO_2(e^-)$ was a long-lived, positive absorption feature at 950 nm (Figure S10 of the Supporting Information).[13]

The transient spectral changes are consistent with the sequence of events in eq 2a. In this sequence, excitation of the

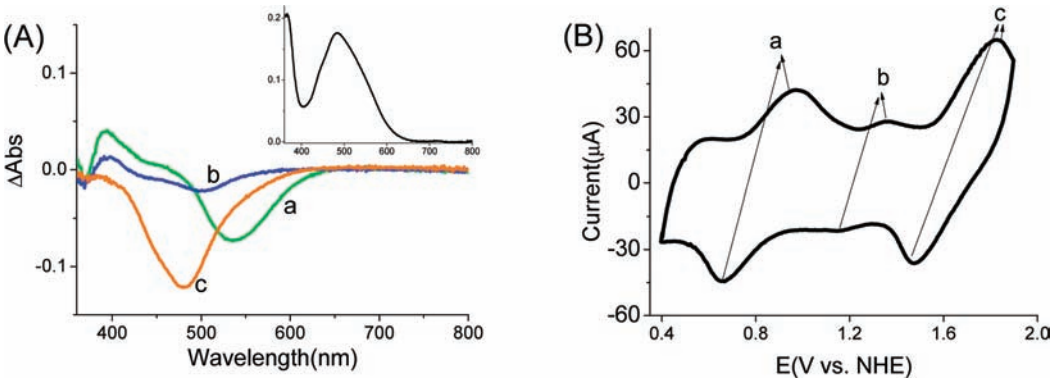

Figure 3. (A) Visible spectral changes in PC with 0.1 M KPF_6 and 2% water accompanying reversible oxidation of *nano*ITO−Ru_a^{II}−Ru_b^{II}−OH_2^{2+} to *nano*ITO−Ru_a^{II}−Ru_b^{III}−OH_2^{3+} (a, green), to *nano*ITO−Ru_a^{II}−Ru_b^{IV}=O^{2+}(b, blue) and to *nano*ITO−Ru_a^{III}−Ru_b^{IV}=O^{3+}(c, orange). Insert: spectrum of *nano*ITO−Ru_a^{II}−Ru_b^{II}−OH_2^{2+}. (B) Cyclic voltammogram of **1C** on *nano*ITO (10 mV/s). Surface coverage (Γ) was 9×10^{-9} mol cm^{-2}, 22 ± 2 °C.

Table 1. $E_{1/2}$ Values (vs NHE) for the Redox Couples of 1C on *nano*ITO, λ_{max} Values, and Differences in Molar Absorptivity ($\Delta\varepsilon$) between Reduced and Oxidized Forms at the Indicated Wavelengths

redox couple[a]	$E_{1/2}$, V		λ_{max}, nm		$\Delta\varepsilon$, mol cm^{-1}[b]	
Ru_a^{II}−Ru_b^{III}−OH_2^{3+}/Ru_a^{II}−Ru_b^{II}−OH_2^{2+}	0.82	0.92	536	518	7300	6600
Ru_a^{II}−Ru_b^{IV}=O^{2+}/Ru_a^{II}−Ru_b^{III}−OH_2^{3+}	1.26	1.25	500	490	2300	2100
Ru_a^{III}−Ru_b^{IV}=O^{2+}/Ru_a^{II}−Ru_b^{IV}=O^{2+}	1.65		482		12400	

[a] Electrolyte was 0.1 M KPF_6 in PC with 2% water (left column) or in 0.1 M $HClO_4$ (right column), 22 ± 2 °C. [b] Visible λ_{max} for Ru_a^{II}−$Ru_b^{II}OH_2^{2+}$ in PC appears at 485 nm (ε = 2.1 × 10^4 M^{-1} cm^{-1}). In 0.1 M $HClO_4$, λ_{max} for Ru_a^{II}−$Ru_b^{II}OH_2^{2+}$ was at 490 nm (ε = 2.2 × 10^4 M^{-1} cm^{-1}).

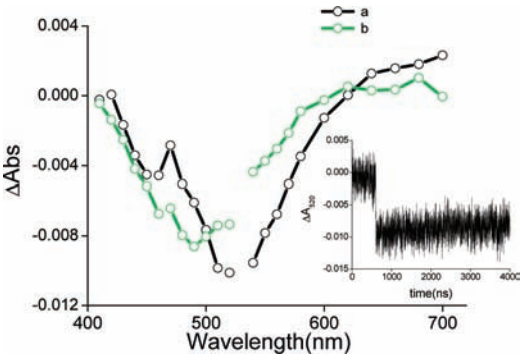

Figure 4. Transient absorption difference spectra obtained at ~80 ns following 532 nm excitation of TiO_2−Ru_a^{II}−Ru_b^{II}−OH_2^{2+} (a, black) and TiO_2−Ru_a^{II}−Ru_b^{III}−OH_2^{3+} (b, green) in PC with 0.2 M $LiClO_4$ and 2% water at 22 ± 2 °C. Surface coverage (Γ) was 6×10^{-8} mol cm^{-2}, 22 ± 2 °C. Insert: Plot of transient absorbance-time trace monitored at 520 nm.

dominant −(BL)Ru_b^{II} light absorber is followed by injection, TiO_2−Ru_a^{II}($BL^{-\bullet}$)Ru_b^{III}−OH_2^{2+*} → $TiO_2(e^-)$−Ru_a^{II}(BL)-Ru_b^{III}−OH_2^{3+}. The efficiency of injection (Φ_{inj}) following excitation at 532 nm was ~0.10 in PC/2%H_2O by using Ru-$(bpy)_3^{2+*}$ in poly(methyl methacrylate) (PMMA) as a chemical actinometer (Supporting Information).[14,15] On the basis of absorbance changes for $TiO_2(e^-)$ at 950 nm relative to [Ru-$(bpy)_2$(4,4′-$(PO_3H_2)_2$bpy]$^{2+}$ (**RuP**) bound to TiO_2, Φ_{inj} was estimated to be ~0.15 in PC/2%H_2O (Table 2).

As previously addressed, light absorbed by the complex at 532 nm is dominantly by the dπ(Ru_b^{II}) → π^*(BL) transition to give the lowest energy, bridge-based MLCT state, ^{3}[($BL^{-\bullet}$)-$Ru_b^{III}OH_2$]. The large spatial separation and weak electronic coupling between π^*($BL^{-\bullet}$) and the TiO_2 interface may significantly reduce the injection rate from this excited state. Results from previous studies have demonstrated ultrafast injection rates and high efficiencies from surface-bound MLCT excited states, whereas low injection rates and efficiencies were observed from remote states.[16−19]

An additional limitation may arise from unfavorable electron injection energetics. On the basis of $E_{1/2}$ = 0.82 V of the ($Ru_a^{II}Ru_b^{III}OH_2^{3+}$/$Ru_a^{II}Ru_b^{II}OH_2^{2+}$) couple and the emission energy for the ^{3}[dπ(Ru_b^{III}) -π^*($BL^{-\bullet}$)] excited state (850 nm), the reduction potential $E^{o'}$ for ($BL^{-\bullet}$)Ru_b^{III} is ~−0.64 V versus NHE. This value is close to the flat band potential for TiO_2 in PC (−0.6 V, Supporting Information, Figure S11). However, despite the 0.4 V positive shift of TiO_2 conduction band (E_{CB} ≈ −0.2 V) in 0.1 M $HClO_4$,[20,21] the injection efficiency increased by a factor of only ~2 with Φ_{inj} ≈ 20%, Figure 5.

Excitation at 532 nm also results in the surface-bound TiO_2−(4,4′-$(HOOC)_2$bpy$^{-\bullet}$)Ru_a^{III} MLCT state or states (eq 2b). This absorption feature accounts for a relatively small fraction of the light absorbed at 532 nm. Injection from related carboxylate−TiO_2-bound MLCT excited states is known to occur rapidly and with high efficiency.[18] However, once excited, injection from these surface-bound MLCT states is in competition with intramolecular energy transfer and rapid relaxation and decay by interconversion and decay from the lowest-lying bridge-based ($BL^{-\bullet}$)Ru_b^{III} MLCT state. In this context, the relatively high injection efficiency for **2P** (~0.4, Table 2) is notable, in demonstrating that can occur directly from a surface-bound

Table 2. Summary of Injection Yields and Lifetimes on TiO_2 Following 532 nm Laser Excitation

complex on TiO_2	electrolyte	Φ_{inj}[a]	$t_{1/2}$ (μs)
$Ru_a^{II}-Ru_b^{II}-OH_2^{2+}$	0.2 M $LiClO_4$ in PC, 2% H_2O	0.10 (0.15)	30
	0.1 M $HClO_4$	0.20 (0.17)	8.4
$Ru_a^{II}-Ru_b^{III}-OH_2^{3+}$	0.2 M $LiClO_4$ in PC, 2% H_2O	(0.17)	27
	0.1 M $HClO_4$	(0.2)	3.6
$Ru(bpy)_2(4,4'-(PO_3H_2)_2bpy)^{2+}$	0.1 M $HClO_4$	1.0	0.5
$Ru(Mebim_2py)(4,4'-(CH_2PO_3H_2)_2(bpy))(OH_2)^{2+}$	0.1 M $HClO_4$	0.45[b] (0.4)	0.6

[a] Injection efficiencies in parentheses determined by ΔA measurements for $TiO_2(e^-)$ at 950 nm at 22 ± 2 °C (Supporting Information). [b] Supporting Information (Figure S12).

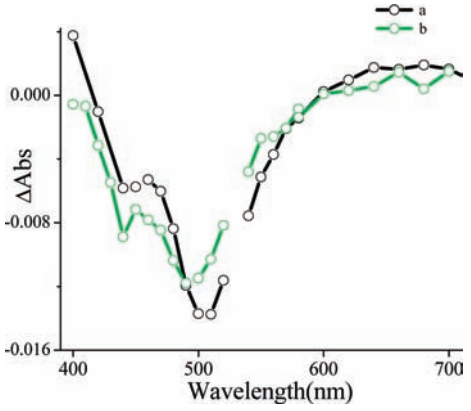

Figure 5. Transient absorption difference spectra obtained ~80 ns following 532 nm excitation of $TiO_2-Ru_a^{II}-Ru_b^{II}-OH_2^{2+}$(a, black) and $TiO_2-Ru_a^{II}-Ru_b^{III}-OH^{2+}$ (b, green) in 0.1 M $HClO_4$ at 22 ± 2 °C. Surface coverage (Γ) was 4.5×10^{-8} mol cm^{-2}.

MLCT state.

$$TiO_2 - Ru_a^{II}(BL)Ru_b^{II}OH_2^{2+} \xrightarrow{h\nu}$$
$$TiO_2 - Ru_a^{II}(BL^{-\cdot})Ru_b^{III}OH_2^{2+*} \xrightarrow{\text{injection}}$$
$$TiO_2(e^-) - Ru_a^{II}(BL)Ru_b^{III}OH_2^{3+} \quad (2a)$$

$$TiO_2 - OOC(bpy)Ru_a^{II}(BL)Ru_b^{II}OH_2^{2+} \xrightarrow{h\nu}$$
$$TiO_2 - OOC(bpy^{-\cdot})Ru_a^{III*}(BL)Ru_b^{II}OH_2^{2+} \xrightarrow{\text{injection}}$$
$$TiO_2(e^-) - Ru_a^{III}(BL)Ru_b^{II}OH_2^{2+} \xrightarrow[\text{rapid}]{\text{electron transfer}}$$
$$TiO_2(e^-) - Ru_a^{II}(BL)Ru_b^{III}OH_2^{3+} \quad (2b)$$

Electron injection by $TiO_2-Ru_a^{II}-Ru_b^{III}-OH_2^{3+}$ following 532 nm excitation was also investigated. In these experiments, $TiO_2-Ru_a^{II}-Ru_b^{III}-OH_2^{3+}$ was generated on the surface by electrolysis at E_{app} = 1.1 V (vs NHE) in the presence of $Fe(bpy)_3^{2+}$ as an electron transfer mediator to overcome slow cross-surface electron transfer on the TiO_2 surface.[22] The maximum bleach in the transient spectrum shifted to ~490 nm in both PC and 0.1 M $HClO_4$ (curve b, Figures 4 and 5). By comparing with the spectral difference between *nano*ITO$-Ru_a^{II}-Ru_b^{IV}=O^{2+}$ and *nano*ITO$-Ru_a^{II}-Ru_b^{III}OH_2^{3+}$ in Figure 3, the transient difference spectrum as well as the slow multiexponential kinetics from 410 to 700 nm following laser excitation are consistent with rapid injection and intramolecular PCET to give $TiO_2(e^-)-Ru_a^{II}-Ru_b^{IV}=O^{2+}$ (eq 3).

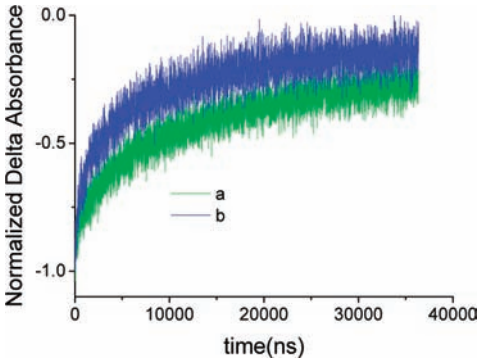

Figure 6. Normalized transient absorbance−time traces at 510 nm for back electron transfer of $TiO_2(e^-)-Ru_a^{II}-Ru_b^{III}-OH_2^{3+}$ (a, green) and at 490 nm for $TiO_2(e^-)-Ru_a^{II}-Ru_b^{IV}=O^{2+}$ (b, blue) following 532 nm excitation in 0.1 M $HClO_4$.

The mechanism for delivery of the oxidative equivalent to the external catalytic site may be different in this case. As shown in eq 3, in the oxidized assembly, $TiO_2-Ru_a^{II}-Ru_b^{III}OH_2^{3+}$, $Ru^{II}{}_a$ is the only intense light absorber. Light absorption is due to a combination of $d\pi(Ru_a^{II}) \rightarrow \pi^*(BL)$ and $d\pi(Ru_a^{II}) \rightarrow \pi^*(4,4'-(COOH)_2bpy)$ transitions. 532 nm excitation would lead to mostly bridging ligand based excited states, followed by intramolecular PCET to form $-Ru^{IV}{}_b=O^{2+}$ at the remote site.

Spectral differences between $TiO_2-Ru_a^{II}-Ru_b^{III}-OH_2^{3+}$ and $TiO_2-Ru_a^{II}-Ru_b^{IV}=O^{2+}$ are small, and TA measurements in the visible could be complicated by interferences from small amounts of $TiO_2-Ru_a^{II}-Ru_b^{II}-OH_2^{2+}$ or $TiO_2-Ru_a^{II}-Ru_b^{IV}=O^{2+}$. Consequently, electron injection efficiencies were determined by monitoring the appearance and decay of amplitude for the $TiO_2(e^-)$ absorbance in the near IR. On the basis of these measurements, values of 0.17 in PC/2% H_2O and 0.20 in 0.1 M $HClO_4$ were obtained.

$$TiO_2 - Ru_a^{II}(BL)Ru_b^{III}OH_2^{3+} \xrightarrow{h\nu}$$
$$TiO_2 - Ru_a^{III}(BL^{-\cdot})Ru_b^{III}OH_2^{3+} \xrightarrow{\text{injection}}$$
$$TiO_2(e^-) - Ru_a^{III}(BL)Ru_b^{III}OH_2^{3+} \xrightarrow[\text{rapid}]{\text{electron transfer}}$$
$$TiO_2(e^-) - Ru_a^{II}(BL)Ru_b^{IV}=O^{2+} + 2H^+ \quad (3)$$

The kinetics of back electron transfer for $TiO_2(e^-)-Ru_a^{II}-Ru_b^{III}-OH_2^{3+}$ and $TiO_2(e^-)-Ru_a^{II}-Ru_b^{IV}=O^{2+}$ following injection were also investigated. Absorbance−time traces in 0.1 M $HClO_4$ following 532 nm excitation are shown in Figure 6 with monitoring at 510 nm for $TiO_2(e^-)-Ru_a^{II}-Ru_b^{III}-OH_2^{3+}$ (eq 4) and at 490 nm for $TiO_2(e^-)-Ru_a^{II}-Ru_b^{IV}=O^{2+}$ (eq 5). The kinetics for both processes were multiexponential, as previously found for back electron transfer following injection by **RuP** on TiO_2.[15] Table 2 summarizes injection yields and times for 50% of the total absorbance change to occur ($t_{1/2}$) for back electron transfer to occur in $TiO_2(e^-)-Ru_a^{II}-Ru_b^{III}-OH_2^{3+}$

and $TiO_2(e^-)-Ru_a^{II}-Ru_b^{IV}=O^{2+}$. These data are compared with data for **RuP** and the aqua monomer **2P** on TiO_2 in Table 2.

The significantly decreased back electron transfer rates (as enhanced half times, $t_{1/2}$) to the remote $-Ru_b^{III}-OH_2^{2+}$ and $-Ru_b^{IV}=O^{2+}$ sites relative to the surface-bound monomers is a notable observation as the appearance of a decay component of $TiO_2(e^-)-Ru_a^{II}-Ru_b^{III}-OH_2^{3+}$ that last for up to ~0.1 s after excitation (Figure S13 of the Supporting Information). $t_{1/2}$ for back electron transfer in 1C occurred on a similar time scale despite the difference in driving force (~0.3 V), and are approximately an order of magnitude longer than that for surface-bound Ru(III) (**RuP** and **2P**, Table 2). An important factor may be the increased electron-tunneling distance[18,23−25] from $TiO_2(e^-)$ to the remote $-Ru_b^{III}-OH^{2+}$ or $-Ru_b^{IV}=O^{2+}$ site in the surface-bound assemblies. Additional factors may also play a role including relative driving forces, a possible kinetic role for PCET in back proton transfer, and differences in the number of injected electrons per TiO_2 particle.[15,26]

$$TiO_2(e^-) - Ru_a^{II} - Ru_b^{III} - OH_2^{3+} \rightarrow TiO_2 - Ru_a^{II} - Ru_b^{II} - OH_2^{2+} \quad (4)$$

$$TiO_2(e^-) - Ru_a^{II} - Ru_b^{IV}=O^{2+} + 2H^+ \rightarrow TiO_2 - Ru_a^{II} - Ru_b^{III} - OH_2^{3+} \quad (5)$$

Our results are important in demonstrating sequential build up of oxidative equivalents at a remote, known water oxidation catalyst site in a molecular assembly on TiO_2. On the basis of these studies, the "rules" that govern excitation, electron injection, and back electron transfer in chromophore−catalyst assemblies are emerging. We are currently exploring related molecular assemblies in photoelectrochemical applications.

■ ASSOCIATED CONTENT

Supporting Information. Synthesis, experimental section, and supplementary results. This material is available free of charge via the Internet at http://pubs.acs.org.

■ AUTHOR INFORMATION

Corresponding Author
*E-mail: tjmeyer@unc.edu.

■ ACKNOWLEDGMENT

This work was funded by the UNC Energy Frontier Research Center (EFRC) "Solar Fuels and Next Generation Photovoltaics", an EFRC funded by the U.S. Department of Energy, Office of Science, Office of Basic Energy Sciences under award DE-SC0001011, supporting M.K.B., J.J.C., and K.H. We acknowledge funding by the Army Research Office through grant W911NF-09-1-0426 for partial support for work by W.S. and C.G. on compound synthesis, separation, and characterization. Partial funding for W.S. and C.G. for work on interfacial photophysics dynamics and spectroelectrochemistry, by the CCHF, an EFRC funded by the U.S. Department of Energy, Office of Science, Office of Basic Energy Sciences, under award number DE-SC0001298 at the University of Virginia, is gratefully acknowledged. We acknowledge support for the purchase of instrumentation from UNC EFRC (Solar Fuels and Next Generation Photovoltaics, an Energy Frontier Research Center funded by the U.S. Department of Energy, Office of Science, Office of Basic Energy Sciences under award number DE-SC0001011) and UNC SERC ("Solar Energy Research Center Instrumentation Facility" funded by the U.S. Department of Energy − Office of Energy Efficiency & Renewable Energy under award number DE-EE0003188)

■ REFERENCES

(1) Alstrum-Acevedo, J. H.; Brennaman, M. K.; Meyer, T. J. Chemical Approaches to Artificial Photosynthesis. 2. *Inorg. Chem.* **2005**, *44*, 6802.

(2) Bard, A. J.; Fox, M. A. Artificial Photosynthesis: Solar Splitting of Water to Hydrogen and Oxygen. *Acc. Chem. Res.* **1995**, *28*, 141.

(3) Concepcion, J. J.; Jurss, J. W.; Brennaman, M. K.; Hoertz, P. G.; Patrocinio, A. O. v. T.; Murakami Iha, N. Y.; Templeton, J. L.; Meyer, T. J. Making Oxygen with Ruthenium Complexes. *Acc. Chem. Res.* **2009**, *42*, 1954.

(4) Gratzel, M. Photoelectrochemical Cells. *Nature* **2001**, *414*, 338.

(5) Meyer, T. J.; Huynh, M. H. V. The Remarkable Reactivity of High Oxidation State Ruthenium and Osmium Polypyridyl Complexes. *Inorg. Chem.* **2003**, *42*, 8140.

(6) Karlsson, S.; Boixel, J.; Pellegrin, Y.; Blart, E.; Becker, H.-C.; Odobel, F.; Hammarström, L. Accumulative Charge Separation Inspired by Photosynthesis. *J. Am. Chem. Soc.* **2010**, *132*, 17977.

(7) Concepcion, J. J.; Tsai, M.-K.; Muckerman, J. T.; Meyer, T. J. Mechanism of Water Oxidation by Single-Site Ruthenium Complex Catalysts. *J. Am. Chem. Soc.* **2010**, *132*, 1545.

(8) Concepcion, J. J.; Jurss, J. W.; Templeton, J. L.; Meyer, T. J. One Site is Enough. Catalytic Water Oxidation by $[Ru(tpy)(bpm)(OH_2)]^{2+}$ and $[Ru(tpy)(bpz)(OH_2)]^{2+}$. *J. Am. Chem. Soc.* **2008**, *130*, 16462.

(9) Chen, Z.; Concepcion, J. J.; Jurss, J. W.; Meyer, T. J. Single-Site, Catalytic Water Oxidation on Oxide Surfaces. *J. Am. Chem. Soc.* **2009**, *131*, 15580.

(10) Chen, Z.; Concepcion, J. J.; Luo, H.; Hull, J. F.; Paul, A.; Meyer, T. J. Nonaqueous Catalytic Water Oxidation. *J. Am. Chem. Soc.* **2010**, *132*, 17670.

(11) Hoertz, P. G.; Chen, Z.; Kent, C. A.; Meyer, T. J. Application of High Surface Area Tin-Doped Indium Oxide Nanoparticle Films as Transparent Conducting Electrodes. *Inorg. Chem.* **2010**, *49*, 8179.

(12) Chen, Z.; Concepcion, J. J.; Hull, J. F.; Hoertz, P. G.; Meyer, T. J. Catalytic Water Oxidation on Derivatized nanoITO. *Dalton Trans.* **2010**, *39*, 6950.

(13) Anderson, A. Y.; Barnes, P. R. F.; Durrant, J. R.; O'Regan, B. C. Simultaneous Transient Absorption and Transient Electrical Measurements on Operating Dye-Sensitized Solar Cells: Elucidating the Intermediates in Iodide Oxidation. *J. Phys. Chem. C* **2010**, *114*, 1953.

(14) Bergeron, B. V.; Kelly, C. A.; Meyer, G. J. Thin Film Actinometers for Transient Absorption Spectroscopy: Applications to Dye-Sensitized Solar Cells. *Langmuir* **2003**, *19*, 8389.

(15) Brennaman, M. K.; Patrocinio, A. O. T.; Song, W.; Jurss, J. W.; Concepcion, J. J.; Hoertz, P. G.; Traub, M. C.; Murakami Iha, N. Y.; Meyer, T. J. Interfacial Electron Transfer Dynamics Following Laser Flash Photolysis of $[Ru(bpy)_2((4,4'\text{-}PO_3H_2)_2bpy]^{2+}$ in TiO_2 Nanoparticle Films in Aqueous Environments. *ChemSusChem* **2011**, *4*, 216.

(16) Xu, Y.; Eilers, G.; Borgström, M.; Pan, J.; Abrahamsson, M.; Magnuson, A.; Lomoth, R.; Bergquist, J.; Polívka, T.; Sun, L.; Sundström, V.; et al. Synthesis and Characterization of Dinuclear Ruthenium Complexes Covalently Linked to RuII Tris-bipyridine: An Approach to Mimics of the Donor Side of Photosystem II. *Chem.—Eur. J.* **2005**, *11*, 7305.

(17) Wolpher, H.; Sinha, S.; Pan, J.; Johansson, A.; Lundqvist, M. J.; Persson, P.; Lomoth, R.; Bergquist, J.; Sun, L.; Sundström, V.; et al. Synthesis and Electron Transfer Studies of Ruthenium−Terpyridine-Based Dyads Attached to Nanostructured TiO_2. *Inorg. Chem.* **2007**, *46*, 638.

(18) Bonhôte, P.; Moser, J.-E.; Humphry-Baker, R.; Vlachopoulos, N.; Zakeeruddin, S. M.; Walder, L.; Grätzel, M. Long-Lived Photoinduced Charge Separation and Redox-Type Photochromism on Mesoporous Oxide Films Sensitized by Molecular Dyads. *J. Am. Chem. Soc.* **1999**, *121*, 1324.

(19) Gholamkhass, B.; Koike, K.; Negishi, N.; Hori, H.; Sano, T.; Takeuchi, K. Adjacent- versus Remote-Site Electron Injection in TiO_2 Surfaces Modified with Binuclear Ruthenium Complexes. *Inorg. Chem.* **2003**, *42*, 2919.

(20) Hagfeldt, A.; Grätzel, M. Light-Induced Redox Reactions in Nanocrystalline Systems. *Chem. Rev.* **1995**, *95*, 49.

(21) Astuti, Y.; Palomares, E.; Haque, S. A.; Durrant, J. R. Triplet State Photosensitization of Nanocrystalline Metal Oxide Electrodes by Zinc-Substituted Cytochrome *c*: Application to Hydrogen Evolution. *J. Am. Chem. Soc.* **2005**, *127*, 15120.

(22) Trammell, S. A.; Meyer, T. J. Diffusional Mediation of Surface Electron Transfer on TiO_2. *J. Phys. Chem. B* **1998**, *103*, 104.

(23) Argazzi, R.; Bignozzi, C. A.; Heimer, T. A.; Castellano, F. N.; Meyer, G. J. Long-Lived Photoinduced Charge Separation across Nanocrystalline TiO_2 Interfaces. *J. Am. Chem. Soc.* **1995**, *117*, 11815.

(24) Haque, S. A.; Handa, S.; Peter, K.; Palomares, E.; Thelakkat, M.; Durrant, J. R. Supermolecular Control of Charge Transfer in Dye-Sensitized Nanocrystalline TiO_2 Films: Towards a Quantitative Structure−Function Relationship. *Angew. Chem., Int. Ed.* **2005**, *44*, 5740.

(25) Hirata, N.; Lagref, J.-J.; Palomares, E. J.; Durrant, J. R.; Nazeeruddin, M. K.; Gratzel, M.; Di Censo, D. Supramolecular Control of Charge-Transfer Dynamics on Dye-Sensitized Nanocrystalline TiO_2 Films. *Chem.—Eur. J.* **2004**, *10*, 595.

(26) Haque, S. A.; Tachibana, Y.; Willis, R. L.; Moser, J. E.; Gratzel, M.; Klug, D. R.; Durrant, J. R. Parameters Influencing Charge Recombination Kinetics in Dye-Sensitized Nanocrystalline Titanium Dioxide Films. *J. Phys. Chem. B* **1999**, *104*, 538.

THE JOURNAL OF PHYSICAL CHEMISTRY Letters

LETTER

pubs.acs.org/JPCL

Competing Pathways in the *photo*-Proton-Coupled Electron Transfer Reduction of *fac*-[Re(bpy)(CO)$_3$(4,4′-bpy)]$^{+*}$ by Hydroquinone

David J. Stewart, M. Kyle Brennaman, Stephanie E. Bettis, Li Wang, Robert A. Binstead, John M. Papanikolas, and Thomas J. Meyer*

Department of Chemistry, University of North Carolina at Chapel Hill, Chapel Hill, North Carolina 27599, United States

Supporting Information

ABSTRACT: The emitting metal-to-ligand charge transfer (MLCT) excited state of *fac*-[Re^{I}(bpy)(CO)$_3$(4,4′-bpy)]$^{+}$ (**1**) (bpy is 2,2′-bipyridine, 4,4′-bpy is 4,4′-bipyridine), [Re^{II}(bpy$^{-\bullet}$)(CO)$_3$(4,4′-bpy)]$^{+*}$, is reductively quenched by 1,4-hydroquinone (H_2Q) in CH_3CN at 23 ± 2 °C by competing pathways to give a common electron−proton-transfer intermediate. In one pathway, electron transfer (ET) quenching occurs to give Re^{I}(bpy$^{-\bullet}$)(CO)$_3$(4,4′-bpy)]^{0} with k = (1.8 ± 0.2) × 10^9 M^{-1} s^{-1}, followed by proton transfer from H_2Q to give [Re^{I}(bpy)(CO)$_3$(4,4′-bpyH$^{\bullet}$)]$^{+}$. Protonation triggers intramolecular bpy$^{\bullet-}$ → 4,4′-bpyH^{+} electron transfer. In the second pathway, preassociation occurs between the ground state and H_2Q at high concentrations. Subsequent Re → bpy MLCT excitation of the adduct is followed by electron−proton transfer from H_2Q in concert with intramolecular bpy$^{\bullet-}$ → 4,4′-bpyH^{+} electron transfer to give [Re^{I}(bpy)(CO)$_3$(4,4′-bpyH$^{\bullet}$)]$^{+}$ with k = (1.0 ± 0.4) × 10^9 s^{-1} in 3:1 CH_3CN/H_2O.

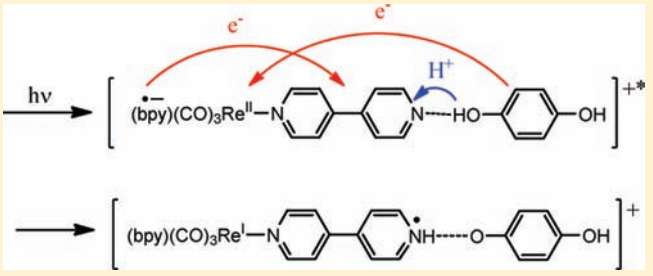

SECTION: Kinetics, Spectroscopy

Understanding proton-coupled electron transfer (PCET) and concerted electron−proton transfer (EPT) and their roles in chemistry and biology continues to evolve.[1−4] PCET is key in energy half reactions such as water oxidation, $2H_2O \rightarrow O_2 + 4H^+ + 4e^-$, and CO_2 reduction, $CO_2 + 8e^- + 8H^+ \rightarrow CH_4 + 2H_2O$. Concerted transfer of electrons and protons in EPT is important in avoiding high-energy protonated intermediates.[5−7] An example occurs in oxidation of tyrosine (TyrOH) by Os(bpy)$_3^{3+}$, Os(bpy)$_3^{3+}$ + TyrOH → Os(bpy)$_3^{2+}$ + TyrOH$^{+\bullet}$. Electron transfer is disfavored by 0.66 eV, whereas multiple site-EPT, with electron transfer to Os(bpy)$_3^{3+}$ and proton transfer to HPO_4^{2-} added as a base, eq 1, is favored by 0.06 eV.[8]

$$Os(bpy)_3^{3+} + TyrOH + HPO_4^{2-} \rightarrow Os(bpy)_3^{2+} + TyrO^{\bullet} + H_2PO_4^{-} \quad (1)$$

There is evidence that molecular excited states can also participate in EPT, a notable example in biology being green fluorescent protein (GFP).[9,10] The appearance of EPT in excited-state reactions has been examined to a limited extent,[5,11−13] but the phenomenon, and its implications for excited-state reactivity and energy conversion, remain to be documented comprehensively. It is of interest for possible application in the photoproduction of energetic intermediates capable of undergoing reactions more complex than electron or energy transfer. The underlying reactivity could be of value in possible applications in energy conversion and artificial photosynthesis, for example.[4,5,7,11,14,15]

An example is reduction of the lowest, bpz-based metal-to-ligand charge transfer (MLCT) excited state of Ru(bpy)$_2$(bpz)$^{2+}$ (bpz is 2,2′-bipyrazine) by hydroquinone (H_2Q) to give the highly reduced transient PCET intermediate, Ru(bpy)$_2$(bpzH$^{\bullet}$)$^{2+}$ which is capable of undergoing net H-atom transfer, eq 2.[5]

$$Ru(bpy)_2(bpz)^{2+} + H_2Q \rightarrow Ru(bpy)_2(bpzH^{\bullet})^{2+} + HQ^{\bullet} \quad (2)$$

In an extension of the previous results, we report here hydroquinone reduction of the lowest MLCT excited state of *fac*-[Re(bpy)(CO)$_3$(4,4′-bpy)]$^{+}$. The results are significant in revealing competitive pathways for excited-state reduction to give the potential H-atom transfer intermediate *fac*-[Re(bpy)(CO)$_3$(4,4′-bpyH$^{\bullet}$)]$^{+}$. Evidence has been obtained for competitive quenching by electron transfer, followed by proton transfer (ET-PT) and by preassociation and concerted electron−proton transfer (EPT) in a *photo*EPT reaction. This is similar to previous work showing complex competition between static and dynamic pathways.[16−18]

Preparation and characterization of **1** as the PF_6^- salt are described in the Supporting Information (SI). Its absorption spectrum in CH_3CN (Figure S1 of the SI) includes intense, ligand-localized $\pi \rightarrow \pi^*$ bands in the UV and a broad shoulder at 330−430 nm from overlapping dπ(Re) → π^*(bpy),π^*(4,4′-bpy)

Received: June 3, 2011
Accepted: June 30, 2011
Published: June 30, 2011

MLCT absorptions. In deaerated CH_3CN, 360 nm excitation of **1** at room temperature results in $^3\{d\pi^5(Re)\pi^*(bpy)^1\}$ (**1***) → $^1\{d\pi^6(Re)\}$ MLCT emission at 570 nm (Figure S2 of the SI) with an excited-state lifetime of $\tau = 266 \pm 13$ ns determined by both transient absorption (Figure S3 of the SI) and emission measurements. In cyclic voltammograms in CH_3CN at 23 ± 2 °C versus $Fc^{+/0}$ (0.63 V vs NHE),[19] a quasireversible $Re^I \rightarrow Re^{II}$ wave appears at $E_{1/2} = 1.36$ V and reversible, reductions at $E_{1/2} = -1.56$ (bpy), −1.64 (4,4′-bpy) (structure shown in Figure 1), and −1.80 V ($Re^I \rightarrow Re^0$) (Figure S4 of the SI), consistent with previous results.[20−22]

Excited-state quenching of **1** in CH_3CN at 23 ± 2 °C occurs with added H_2Q, as shown by Stern−Volmer luminescence (Figures S2 and S5 of the SI) and lifetime (Figure S6 of the SI) measurements with experimental details in the Supporting Information. In Figures S5 and S6 of the SI are shown plots of I_0/I versus $[H_2Q]$ and τ_0/τ versus $[H_2Q]$, respectively, with I_0 and τ_0 the emission intensity and lifetime without quencher and I and τ the same quantities with quencher added (eqs 3 and 4). From the slopes of these plots and the excited-state lifetime, $k_q = (1.8 \pm 0.2) \times 10^9\ M^{-1}\ s^{-1}$. Excited-state quenching experiments were also conducted in 1:1 v/v mixtures of CH_3CN-H_2O and CH_3CN-D_2O with 0.1 M added KPF_6. In these media, $k_q(H_2O) = (3.04 \pm 0.09) \times 10^9\ M^{-1}\ s^{-1}$ and $k_q(D_2O) = (2.8 \pm 0.1) \times 10^9\ M^{-1}\ s^{-1}$ giving a kinetic isotope effect (KIE) for quenching of $k(H_2O)/k(D_2O) = 1.1$ (Figure S7 of the SI).

$$\tau_0/\tau = 1 + \tau_0 k_q[H_2Q] \quad (3)$$

$$I_0/I = 1 + \tau_0 k_q[H_2Q] \quad (4)$$

The excited-state absorption spectrum of **1*** in CH_3CN at 23 ± 2 °C, obtained 10 ns following laser flash excitation at 355 nm, includes maxima at 370, 420, and 460 nm (Figure S3 of the SI), as expected for the MLCT excited-state $[Re^{II}(bpy^{-\bullet})(CO)_3(4,4'bpy)]^{+*}$.[23] In transient spectra with addition of H_2Q, new absorption features appear at $\lambda_{max} = 400$, 420 (shoulder), and 490 nm at the expense of the excited-state absorption features (Figure 2). An additional feature grows at 590 nm because of a following reaction, as discussed below. As shown by the absorbance−time trace in Figure S8 of the SI, obtained at 375 nm, excited-state quenching is first-order in $[H_2Q]$. From the slope of the plot of k_{obsd} versus $[H_2Q]$ (Figure S9 of the SI), $k_{obsd} = k_q = (1.80 \pm 0.07) \times 10^9\ M^{-1}\ s^{-1}$, consistent with the emission result.

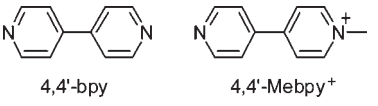

Figure 1. Structures of 4,4′-bpy and 4,4′-$Mebpy^+$.

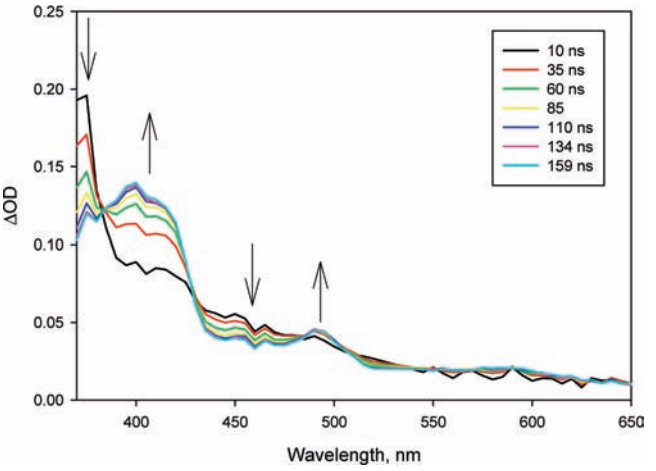

Figure 2. Time-dependent transient absorption difference spectrum of **1** in CH_3CN. [**1**] = 0.1 mM, [TBAH] = 0.1 M, $[H_2Q]$ = 0.01 M, λ_{ex} = 355 nm, 23 ± 2 °C.

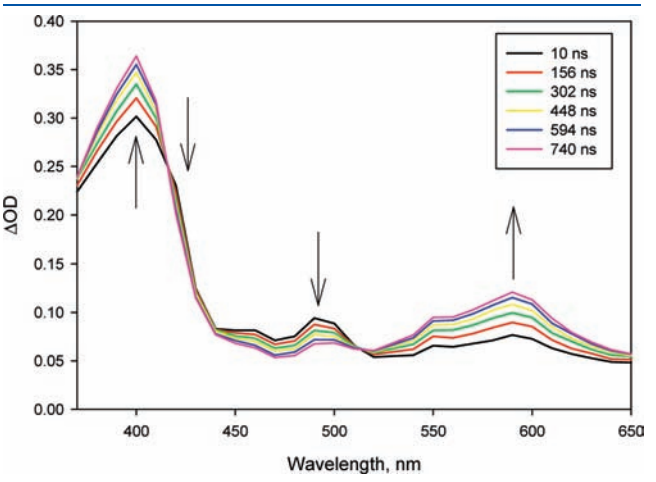

Figure 3. TA difference spectra for **1** in CH_3CN. [**1**] = 0.1 mM, [TBAH] = 0.1 M, $[H_2Q]$ = 0.5 M, λ_{ex} = 355 nm, 23 ± 2 °C.

Scheme 1. Mechanism for Photochemical Reduction of *fac*-$[Re^I(bpy)(CO)_3(4,4'\text{-bpy})]^+$ by H_2Q

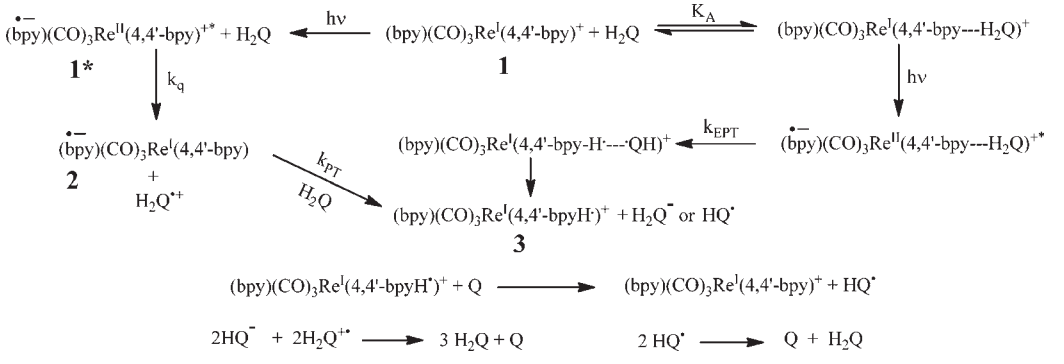

dx.doi.org/10.1021/jz2007512 |J. Phys. Chem. Lett. 2011, 2, 1844–1848

Scheme 2. Mechanism of Proton Transfer from H_2Q to $[Re^{I}(bpy^{-\bullet})(CO)_3(4,4'\text{-bpy})]^0$

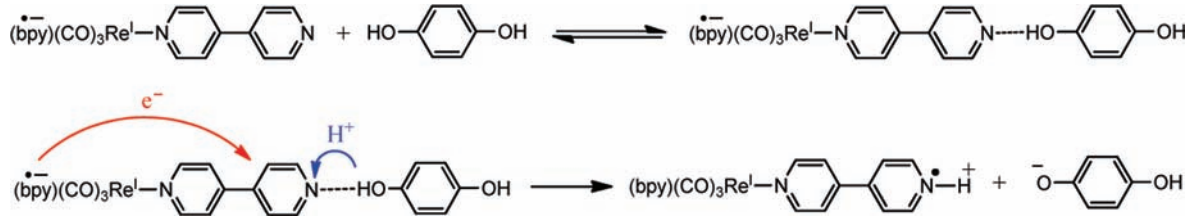

The spectral changes observed with added hydroquinone are consistent with reductive electron transfer quenching to give $[Re^{I}(bpy^{-\bullet})(CO)_3(4,4'\text{-bpy})]^0$, **2**, as shown in eq 5 and Scheme 1. In the difference spectrum, the absorption features at 400, 420, and 490 nm can be assigned to the hydroquinone radical-cation, $H_2Q^{\bullet+}$(400 and 420 nm)[24] and the reduced complex, respectively. Electron transfer quenching is consistent with the relatively small $k(H_2O)/k(D_2O)$ KIE of 1.1 for k_q in 1:1 CH_3CN/H_2O.

$$[Re^{II}(bpy^{-\bullet})(CO)_3(4,4'\text{-bpy})]^{+}* + H_2Q \rightarrow$$
$$[Re^{I}(bpy^{-\bullet})(CO)_3(4,4'\text{-bpy})]^{0} + H_2Q^{+\bullet} \quad (5)$$

Once formed, **2** undergoes a further reaction with H_2Q. With $[H_2Q]$ > 0.1 M, the rate of electron transfer quenching is sufficiently rapid that **2** is the first observable intermediate 10 ns after the laser pulse (Figure 3). Under these conditions, initial maxima are observed at 400, 490, and 590 nm with a shoulder at 420 nm. Over the first few hundred nanoseconds, the 400 and 590 nm maxima increase, and 420 and 490 nm maxima decrease with isosbestic points at 415 and 515 nm. These observations are consistent with appearance of an additional intermediate, **3**. Absorbance−time measurements at 490 (**2**) and 590 nm (**3**) (Figure S10 of the SI) show that the rate of appearance of **3** is first-order in $[H_2Q]$ with $k_{obsd} = (2.5 \pm 0.2) \times 10^6\ M^{-1}\ s^{-1}$ in CH_3CN. On the basis of rate measurements in 1:1 (v/v) CH_3CN-H_2O, $k_{obsd} = 1.6 \times 10^7\ M^{-1}s^{-1}$, and in 1:1 (v/v) CH_3CN-D_2O, $k_{obsd} = (9.2 \pm 0.2) \times 10^6\ M^{-1}\ s^{-1}$. This reaction occurs with $k(H_2O)/k(D_2O) = 1.7$ (Figure S13 of the SI).

For **3**, the absorption features at 590 and 400 nm are analogous to absorptions at λ_{max} = 610 and 370 nm for singly reduced $[Re^{I}(bpy)(CO)_3(4,4'\text{-Mebpy}^{\bullet})]$[25] (4,4′-Mebpy is *N*-methyl-4,4′-bipyridinium cation) in 1,2-dichloroethane. For singly reduced $[Re^{I}(dmb)(CO)_3(4,4'\text{-Mebpy}^{\bullet})]$[26] (dmb is 4,4′-dimethyl-2,2′-bipyridine) in CH_2Cl_2, λ_{max} = 630 and 380 nm. The 400 nm absorption includes significant contributions from $H_2Q^{\bullet+}$[24] and $HQ^{\bullet}$,[5,27] the latter of which is formed by a following reaction, as discussed below. These comparisons and first-order kinetics in H_2Q are consistent with Scheme 2 and proton transfer from H_2Q to $[Re^{I}(bpy^{-\bullet})(CO)_3(4,4'\text{-bpy})]^0$ to give **3** as $[Re^{I}(bpy)(CO)_3(4,4'bpyH^{\bullet})]^+$.

The net effect of proton transfer in Scheme 2 is a notable example of an intramolecular, concerted EPT or *photo*EPT reaction.[28] In this reaction, proton transfer to the remote 4,4′-bpy N-atom in $[Re^{I}(bpy^{-\bullet})(CO)_3(4,4'\text{-bpy})]^0$ triggers intramolecular electron transfer from π^*(bpy) to π^*(4,4′-bpy). In the EPT process, electron transfer occurs from π^*(bpy) to π^*(4,4-bpyH$^+$). This proton-induced process is analogous to MLCT → MLCT′ excited-state interconversion following $Re^{I} \rightarrow$ bpy excitation of $[Re^{I}(bpy)(CO)_3(4,4'\text{-Mebpy})]^{2+}$, eq 6, for which

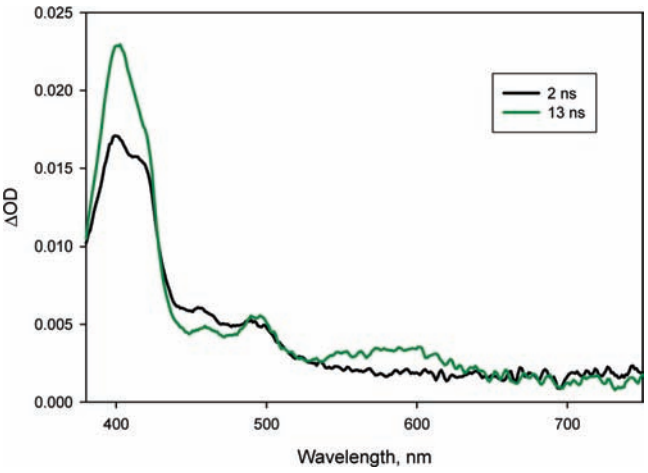

Figure 4. TA difference spectra for **1** in CH_3CN. [**1**] = 0.1 mM, [TBAH] = 0.1 M, $[H_2Q]$ = 0.5 M, λ_{ex} = 355 nm, 23 ± 2 °C.

$\Delta G \approx -0.49$ eV.[25] For the reaction in Scheme 2, protonation stabilizes the higher energy $[Re^{I}(bpy)(CO)_3(4,4'\text{-bpy}^{-\bullet})]^0$ state and provides the driving force for intramolecular EPT.

$$[Re^{I}(bpy)(CO)_3(4,4'\text{-Mebpy})]^{2+} \xrightarrow{h\nu}$$
$$[Re^{II}(bpy^{-\bullet})(CO)_3(4,4'\text{-Mebpy})]^{2+*} \rightarrow$$
$$[Re^{II}(bpy)(CO)_3(4,4'\text{-Mebpy}^{-\bullet})]^{2+*} \quad (6)$$

At H_2Q concentrations near saturation (~1.0 M), UV−visible spectral changes suggest that initial preassociation between **1** and H_2Q occurs (Figure S12 of the SI), but it is difficult to estimate the association constant by spectral measurements. Transient absorption measurements under these conditions, with monitoring on the 0.5 ns time scale by using the pump−probe technique described in SI, revealed a second mechanism for excited-state quenching. Transient absorption difference spectra obtained at 2 and 13 ns after laser flash excitation at 355 nm are shown in Figure 4. In the 2 ns spectrum with 0.5 M added H_2Q, absorption features for both **2** (400 and 490 nm) and the residual excited state **1*** (460 nm) are observed. As shown in the 13 ns spectrum, subsequent disappearance of the excited state occurs in concert with continued growth of **2** as *photo*EPT occurs.

Notable in the 13 ns spectrum is the appearance of the absorptions characteristic of **3** at 400 and 590 nm. As shown by the absorbance−time traces in 3:1 CH_3CN/X_2O with monitoring at 590 nm (Figure S13 of the SI), this feature grows with $k_{obsd,H_2O} = (1.0 \pm 0.4) \times 10^9\ s^{-1}$ and $k_{obsd,D_2O} = (6.9 \pm 0.3) \times 10^8\ s^{-1}$ with a KIE of 1.43 ± 0.06. In a second, much slower stage, continued growth of **3** occurs but only on the longer time

dx.doi.org/10.1021/jz2007512 |*J. Phys. Chem. Lett.* 2011, 2, 1844–1848

Scheme 3. *photo*EPT Following MLCT Excitation of the Pre-Associated Complex between 1 and H_2Q

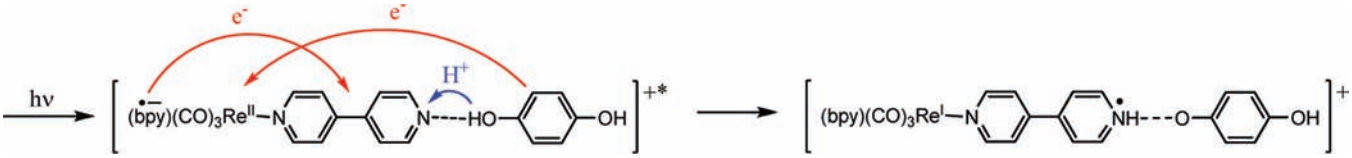

Scheme 4. Sequential EPT Pathway in the Pre-Associated Complex between 1 and H_2Q

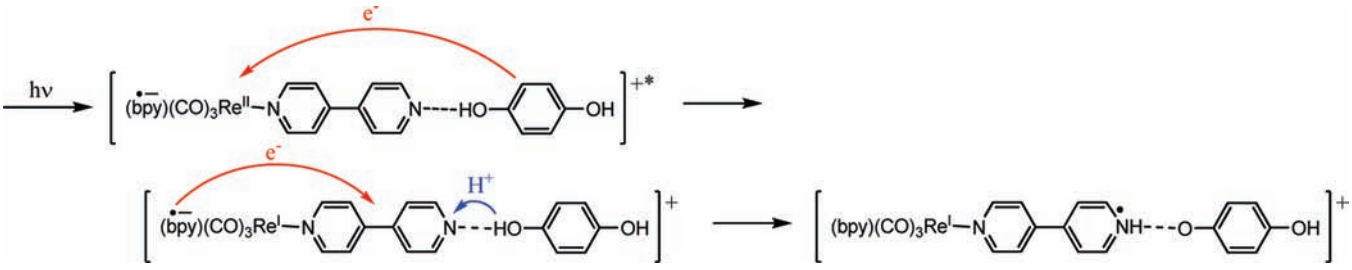

scale for diffusional interconversion of **2** to **3** by proton transfer from H_2Q (Figure 3 and Scheme 2). *Photo*EPT is incomplete under these conditions because of partial adduct formation.

As shown in Schemes 1 and 3, the observations on the 0.5 ns time scale are consistent with a second mechanism for reductive quenching. In this mechanism, preassociation between H_2Q and the ground-state complex occurs, presumably in a preformed hydrogen-bonded adduct. In the net sense, Re → bpy MLCT excitation of the adduct leads to a proton transfer in concert with a double electron transfer. One electron is transferred in concert with proton transfer from H_2Q to $[Re^{II}(bpy^{\bullet-})(CO)_3(4,4'\text{-bpy})]^{+*}$ and the second from $bpy^{\bullet-}$ → 4,4′-bpy. Given the relatively small KIE of 1.4, the *photo*EPT mechanism may be sequential with initial electron transfer, followed by EPT without formation of a discrete H_2Q^+ (Scheme 4). In any case, the change between diffusional and preassociated mechanisms is notable and points to a structural importance for preassociation and prior H-bond formation.

It was not possible to investigate the back reaction between $[Re^{I}(bpy)(CO)_3(4,4'\text{-bpyH}^{\bullet})]^{+}$ and $HQ^{\bullet}$ because of trace amounts of 1,4-benzoquinone (Q) in the H_2Q sample. Oxidation of **3** by added 1,4-benzoquinone (Q) was also observed by transient absorption measurements in the presence of an added pseudo-first-order excess of Q over the concentration range 0.25−4.0 mM in CH_3CN with 0.25 M added H_2Q at 23 ± 2 °C. Reaction between **3** and Q (eq 7) produces the original ground-state complex, λ_{max} = 320 and 350(sh) nm, and $HQ^{\bullet}$, λ_{max} = 400 nm in CH_3CN and 410 nm in 1:1 H_2O/CH_3CN (Figure S14 of the SI), consistent with previous results.[5,27] The kinetics of back electron transfer following 355 nm excitation with absorption monitoring at 590 nm (λ_{max} for **3**) were first order in [Q]. From a plot of k_{obsd} versus [Q] (Figure S15 of the SI), $k_{EPT} = 8.0 \times 10^9$ M^{-1} s^{-1} in CH_3CN and 6.0×10^9 M^{-1} s^{-1} in 1:1 CH_3CN/H_2O. This can be compared with $k_{EPT} = 8.5 \times 10^8$ M^{-1} s^{-1} for oxidation of $Ru(bpy)_2(bpzH^{\bullet})^{2+}$ by Q under the same conditions.[5] On the basis of rate comparisons between 1:1 CH_3CN/H_2O and 1:1 CH_3CN/D_2O (Figure S16 of the SI), KIE = 1.3 for back EPT in eq 7. In the final step of the overall mechanism (Scheme 1), on much longer time scales, $HQ^{\bullet}$ undergoes disproportionation to H_2Q and Q with

$$[Re^{I}(bpy)(CO)_3(4,4\text{-bpy-H}]^{+} + Q \rightleftharpoons [Re^{I}(bpy)(CO)_3(4,4\text{-bpy-H}\cdots Q]^{+} \xrightarrow{k_{EPT}} [Re^{I}(bpy)(CO)_3(4,4\text{-bpy}]^{+} + HQ^{\bullet} \quad (7)$$

$k = 6.1 \times 10^5$ (CH_3CN) and 2.0×10^5 M^{-1} s^{-1} (1:1 H_2O/CH_3CN) (Figure S17 of the SI) consistent with previous observations on $HQ^{\bullet}$ disproportionation under comparable conditions.[5]

The results obtained here are summarized in Scheme 1. They are significant in extending the known reactivity of molecular excited states toward *photo*EPT, in this case revealing subtle but essential factors in this reactivity including the importance of H-bond preassociation prior to the redox step. This is an essential feature in EPT and in proton transfer. It arises because of the short-range nature of proton transfer due to the greatly decreased radial extensions of protonic wave functions compared with electronic wave functions.[29] The intricate series of intramolecular events triggered by proton addition to **2** in Scheme 2 and electron−proton addition to **3** in Scheme 3 are also notable. They reveal a rich and variegated *photo*EPT reactivity of MLCT excited states.

■ ASSOCIATED CONTENT

Supporting Information. Experimental details and characterization of **1**. Additional UV−vis, emission, TA, and kinetic studies. This material is available free of charge via the Internet at http://pubs.acs.org.

■ AUTHOR INFORMATION

Corresponding Author
*E-mail: tjmeyer@unc.edu.

■ ACKNOWLEDGMENT

This work has been supported by the National Science Foundation under grant CHE-0957215 (supporting D.J.S.)

and by the UNC EFRC: Solar Fuels and Next Generation Photovoltaics, an Energy Frontier Research Center funded by the U.S. Department of Energy, Office of Science, Office of Basic Energy Sciences under award number DE-SC0001011 (supporting M.K.B, S.E.B., L.W., and R.A.B). We acknowledge support for the purchase of instrumentation from the UNC EFRC under U.S. DOE award number DE-SC0001011, as listed above, and UNC SERC ("Solar Energy Research Center Instrumentation Facility" funded by the US Department of Energy − Office of Energy Efficiency & Renewable Energy under award number DE-EE0003188).

REFERENCES

(1) Huynh, M. H. V.; Meyer, T. J. Proton-Coupled Electron Transfer. *Chem. Rev.* **2007**, *107*, 5004–5064.

(2) Mayer, J. M. Proton-Coupled Electron Transfer: A Reaction Chemist's View. *Annu. Rev. Phys. Chem.* **2004**, *55*, 363–390.

(3) Reece, S. Y.; Hodgkiss, J. M.; Stubbe, J.; Nocera, D. G. Proton-Coupled Electron Transfer: The Mechanistic Underpinning for Radical Transport and Catalysis in Biology. *Philos. Trans. R. Soc., B* **2006**, *361*, 1351–1364.

(4) Hammes-Schiffer, S. Theory of Proton-Coupled Electron Transfer in Energy Conversion Processes. *Acc. Chem. Res.* **2009**, *42*, 1881–1889.

(5) Concepcion, J. J.; Brennaman, M. K.; Deyton, J. R.; Lebedeva, N. V.; Forbes, M. D. E.; Papanikolas, J. M.; Meyer, T. J. Excited-State Quenching by Proton-Coupled Electron Transfer. *J. Am. Chem. Soc.* **2007**, *129*, 6968–6969.

(6) Gagliardi, C. J.; Jurss, J. W.; Thorp, H. H.; Meyer, T. J. Surface Activation of Electrocatalysis at Oxide Electrodes. Concerted Electron-Proton Transfer. *Inorg. Chem.* **2011**, *50*, 2076–2078.

(7) Costentin, C.; Robert, M.; Saveant, J. M. Concerted Proton-Electron Transfers: Electrochemical and Related Approaches. *Acc. Chem. Res.* **2010**, *43*, 1019–1029.

(8) Fecenko, C. J.; Thorp, H. H.; Meyer, T. J. The Role of Free Energy Change in Coupled Electron-Proton Transfer. *J. Am. Chem. Soc.* **2007**, *129*, 15098–15099.

(9) Leiderman, P.; Genosar, L.; Huppert, D.; Shu, X.; Remington, S. J.; Solntsev, K. M.; Tolbert, L. M. Ultrafast Excited-State Dynamics in the Green Fluorescent Protein Variant S65t/H148d. 3. Short- and Long-Time Dynamics of the Excited-State Proton Transfer. *Biochemistry* **2007**, *46*, 12026–12036.

(10) Shi, X.; Abbyad, P.; Shu, X.; Kallio, K.; Kanchanawong, P.; Childs, W.; Remington, S. J.; Boxer, S. G. Ultrafast Excited-State Dynamics in the Green Fluorescent Protein Variant S65t/H148d. 2. Unusual Photophysical Properties. *Biochemistry* **2007**, *46*, 12014–12025.

(11) Gagliardi, C. J.; Westlake, B. C.; Kent, C. A.; Paul, J. J.; Papanikolas, J. M.; Meyer, T. J. Integrating Proton-Coupled Electron-Transfer (Pcet) and Excited States. *Coord. Chem. Rev.* **2010**, *254*, 2459–2471.

(12) Hazra, A.; Soudackov, A. V.; Hammes-Schiffer, S. Isotope Effects on the Nonequilibrium Dynamics of Ultrafast Photoinduced Proton-Coupled Electron Transfer Reactions in Solution. *J. Phys. Chem. Lett.* **2011**, *2*, 36–40.

(13) Swarnalatha, K.; Rajkumar, E.; Rajagopal, S.; Ramaraj, R.; Banu, I. S.; Ramamurthy, P. Proton-Coupled Electron-Transfer Reaction of Phenols with Excited State Ruthenium(II) - Polypyridyl Complexes. *J. Phys. Org. Chem.* **2011**, *24*, 14–21.

(14) Alstrum-Acevedo, J. H.; Brennaman, M. K.; Meyer, T. J. Chemical Approaches to Artificial Photosynthesis. 2. *Inorg. Chem.* **2005**, *44*, 6802–6827.

(15) Meyer, T. J.; Huynh, M. H. V.; Thorp, H. H. The Possible Role of Proton-Coupled Electron Transfer (Pcet) in Water Oxidation by Photosystem II. *Angew. Chem., Int. Ed.* **2007**, *46*, 5284–5304.

(16) Balzani, V.; Moggi, L.; Manfrin, M. F.; Bolletta, F. Quenching and Sensitization Processes of Coordination-Compounds. *Coord. Chem. Rev.* **1975**, *15*, 321–433.

(17) Rybak, W.; Haim, A.; Netzel, T. L.; Sutin, N. Optically Induced Electron-Transfer within Ion-Pairs - the $Os(5\text{-Cl-Phen})_3^{2+}$—$Fe(Cn)_6^{4-}$ System. *J. Phys. Chem.* **1981**, *85*, 2856–2860.

(18) Frank, R.; Rau, H. Static and Dynamic Quenching of the Emission of Excited Ruthenium(II) Tris(Bipyridyl) Cation by Nickel(II) Tetracyanodithiolene Anion. *J. Phys. Chem.* **1983**, *87*, 5181–5184.

(19) Pavlishchuk, V. V.; Addison, A. W. Conversion Constants for Redox Potentials Measured Versus Different Reference Electrodes in Acetonitrile Solutions at 25 °C. *Inorg. Chim. Acta* **2000**, *298*, 97–102.

(20) Velayudham, M.; Rajkumar, M.; Rajagopal, S.; Ramamurthy, P. Synthesis, Characterization, Electrochemical and Photophysical Properties of Bimetallic Complexes of Rhenium(I) and Osmium(Ii). *Polyhedron* **2008**, *27*, 3417–3424.

(21) Lin, R. G.; Fu, Y. G.; Brock, C. P.; Guarr, T. F. Structural, Spectroscopic, and Electrochemical Investigation of Luminescent Bimetallic Complexes of Rhenium(I). *Inorg. Chem.* **1992**, *31*, 4346–4353.

(22) Stor, G. J.; Hartl, F.; Vanoutersterp, J. W. M.; Stufkens, D. J. Spectroelectrochemical (Ir, Uv/Vis) Determination of the Reduction Pathways for a Series of $[Re(Co)_3(\alpha\text{-Diimine})L']^{0/+}$ (L′ = Halide, Otf^-, Thf, Mecn, N-Prcn, Pph_3, $P(Ome)_3$) Complexes. *Organometallics* **1995**, *14*, 1115–1131.

(23) Rossenaar, B. D.; Stufkens, D. J.; Vlcek, A. Halide-Dependent Change of the Lowest-Excited-State Character from Mlct to Xlct for the Complexes $Re(X)(Co)_3(\alpha\text{-Diimine})$ (X = Cl, Br, I; α-Diimine = Bpy, Ipr-Pyca, Ipr-Dab) Studied by Resonance Raman, Time-Resolved Absorption, and Emission Spectroscopy. *Inorg. Chem.* **1996**, *35*, 2902–2909.

(24) Yamada, H.; Kimura, K. Dimer Phenomena of Cation Radicals of *para*-Dialkoxybenzenes in Concentrated Sulfuric Acid. *J. Chem. Phys.* **1969**, *51*, 5733–&.

(25) Chen, P. Y.; Danielson, E.; Meyer, T. J. Role of Free-Energy Change on Medium Effects in Intramolecular Electron-Transfer. *J. Phys. Chem.* **1988**, *92*, 3708–3711.

(26) Liard, D. J.; Kleverlaan, C. J.; Vlcek, A. Solvent-Dependent Dynamics of the $Mq^{\bullet} \rightarrow Re^{II}$ Excited-State Electron Transfer in $[Re(Mq^+)(Co)_3(Dmb)]^{2+}$. *Inorg. Chem.* **2003**, *42*, 7995–8002.

(27) Rao, P. S.; Hayon, E. Ionization-Constants and Spectral Characteristics of Some Semiquinone Radicals in Aqueous-Solution. *J. Phys. Chem.* **1973**, *77*, 2274–2276.

(28) Westlake, B. C.; Brennaman, M. K.; Concepcion, J. J.; Paul, J. J.; Bettis, S. E.; Hampton, S. D.; Miller, S. A.; Lebedeva, N. V.; Forbes, M. D. E.; Moran, A. M.; Meyer, T. J.; Papanikolas, J. M. Concerted Electron-Proton Transfer in the Optical Excitation of Hydrogen-Bonded Dyes. *Proc. Natl. Acad. Sci.* **2011**, *108*, 8554–8558.

(29) Iordanova, N.; Hammes-Schiffer, S. Theoretical Investigation of Large Kinetic Isotope Effects for Proton-Coupled Electron Transfer in Ruthenium Polypyridyl Complexes. *J. Am. Chem. Soc.* **2002**, *124*, 4848–4856.